

Phase Contrast X-ray Imaging in the Lungs: A Technique to Study Dynamic Alveolar Function

Richard Carnibella

Department of Mechanical and Aerospace Engineering
Monash University



Monash University

Declaration for thesis based or partially based on conjointly published or unpublished work

General Declaration

In accordance with Monash University Doctorate Regulation 17.2 Doctor of Philosophy and Research Master's regulations the following declarations are made:

I hereby declare that this thesis contains no material which has been accepted for the award of any other degree or diploma at any university or equivalent institution and that, to the best of my knowledge and belief, this thesis contains no material previously published or written by another person, except where due reference is made in the text of the thesis.

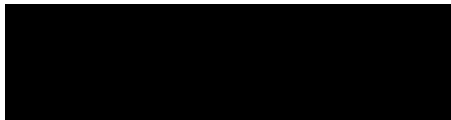
This thesis includes 4 original papers published in peer reviewed journals. The core theme of the thesis is the development of a novel X-ray technique for measuring the properties of granular and porous materials, with a focus on studying alveoli in the lungs as a specific application. The ideas, development and writing up of all the papers in the thesis were the principal responsibility of myself, the candidate, working within the Department of Mechanical and Aerospace Engineering under the supervision of Prof. Andreas Fouras, Dr Marcus Kitchen and Prof. Kerry Hourigan.

The inclusion of co-authors reflects the fact that the work came from active collaboration between researchers and acknowledges input into team-based research.

In the case of Chapters 2, 3, 4 and 5 my contribution to the work involved the following:

Thesis chapter	Publication title	Publication status*	Nature and extent of candidate's contribution
2	Determining particle size distributions from a single projection image	Published	Initiated the paper, conducted experiments, performed analysis and wrote manuscript (90%)
3	Decoding the structure of granular and porous materials from speckled phase contrast X-ray images	Published	Initiated the paper, conducted experiments, performed analysis and wrote manuscript (90%)
4	Single-exposure dual-energy-subtraction X-ray imaging using a synchrotron source	Published	Initiated the paper, conducted experiments, performed analysis and wrote manuscript (85%)
5	Single-shot X-ray measurement of alveolar size distributions	Published	Initiated the paper, conducted experiments, performed analysis and wrote manuscript (85%)

I have not renumbered sections of submitted or published papers in order to generate a consistent presentation within the thesis.

Signed: 

Date: 11/12/2016

Abstract

Despite the central role played by the alveoli in respiration, the tools currently available for assessing alveoli are very limited. Most functional lung imaging techniques lack the spatial resolution to measure function at the alveolar level. Those techniques capable of measuring alveolar function overcome this limitation by inferring function indirectly. Contrast in the lungs, spatial and temporal resolution, and reproducibility have all been significant impediments.

Processes that disrupt the normal function of the alveoli can have a serious impact on lung function and health. Emphysema, which is characterised by the destruction of alveoli, is the most common disease to directly affect the alveoli and is a leading cause of morbidity and mortality around the world. Patients who receive mechanical ventilation, particularly neonates, are also at risk of alveolar damage due to either alveolar collapse or overdistension.

Propagation-based phase contrast imaging exploits the properties of coherent X-ray radiation to produce remarkable contrast in images of the lungs. In projection, phase contrast X-ray images of the lungs exhibit a strongly speckled appearance. In this work it was shown that speckle produced by granular and porous materials like the lungs is dependent on the microstructure of the material. A technique was developed to decode the speckle images and in the case of the lungs, measure the distribution of alveolar diameters.

Initial work is based on modelling the lungs as a distribution of closely packed spherical particles. Two different techniques, for sparsely and close-packed particles, were developed for solving the inverse problem of determining the distribution of particles producing X-ray speckle. The method is based on using the spatial autocorrelation function as a speckle descriptor. Samples of glass microspheres were used to validate the accuracy of the technique.

The focus shifts to biological samples with the development of a dual energy synchrotron-based method for bone segmentation and suppression from chest X-rays. This precedes the application of speckle analysis in the lungs where the lung speckle is partially obscured by the ribcage.

Finally, the previously developed speckle analysis technique is employed to measure alveolar size in rabbit pup lungs. Initially in fixed, postmortem lungs where the results showed good agreement to high resolution CT. Then proceeding to dynamic, in vivo imaging of breathing lung, from which regional alveolar size and change in alveolar size were determined. As expected, these measurements were found to correlate closely with the respiratory phase. Towards validating in vivo accuracy, the measured distribution of alveoli was used to estimate the total number of alveoli as

well as alveolar recruitment, which were found in good agreement with published values.

Future work will focus on exploring applications in preclinical studies. Specific areas in which this technique may provide new insights include early disease diagnosis and monitoring of therapeutic efficacy in emphysema, and our understanding of the mechanisms of ventilator induced lung injury leading to the development of improved mechanical ventilation strategies.

Acknowledgements

I would like to begin by thanking all my supervisors, and especially Andreas and Marcus, for their support, guidance and time. Thanks to all the guys, past and present, who I've had the pleasure of working alongside in the LDI lab — it's been a lot of fun! Thank you to Stuart Hooper and the team at The Richie Centre for your support and assistance. And thank you to Kentaro Uesugi and all the beamline scientists at SPring-8 for your assistance and hospitality. My trips to the SPring-8 synchrotron in Japan were a real highlight of my time as a postgraduate student. Thanks to all the people I've met along the way, whose energy and enthusiasm have been an inspiration. And finally thanks to my family and friends, for your encouragement and support.

Publications

Constituent publications of this thesis

1. **Carnibella, R. P.**, Fouras, A., Kitchen, M. J., (2012a). “Single-exposure dual-energy-subtraction X-ray imaging using a synchrotron source”. In: *Journal of Synchrotron Radiation* 19, pp. 954–959.
2. **Carnibella, R. P.**, Kitchen, M. J., Fouras, A., (2012b). “Determining particle size distributions from a single projection image”. In: *Optics Express* 20.14, pp. 15962–15968.
3. **Carnibella, R. P.**, Kitchen, M. J., Fouras, A., (2013). “Decoding the structure of granular and porous materials from speckled phase contrast X-ray images”. In: *Optics Express* 21.16, pp. 19153–19162.
4. **Carnibella, R. P.**, Kitchen, M. J., Fouras, A., (2014). “Single-shot X-ray measurement of alveolar size distributions”. In: *Biomedical Applications in Molecular, Structural, and Functional Imaging*. SPIE Medical Imaging. SPIE.

Other published articles

5. Thurgood, J., Hooper, S., Siew, M., Wallace, M., Dubsky, S., Kitchen, M. J., Jamison, R. A., **Carnibella, R.**, Fouras, A., (2012). “Functional lung imaging during HFV in preterm rabbits”. In: *PLoS ONE* 7.10, e48122.
6. Donnelley, M., Morgan, K. S., Siu, K. K. W., Fouras, A., Farrow, N. R., **Carnibella, R. P.**, Parsons, D. W., (2014). “Tracking extended mucociliary transport activity of individual deposited particles: longitudinal synchrotron X-ray imaging in live mice”. In: *Journal of Synchrotron Radiation* 21.4, pp. 768–773.
7. Kitchen, M. J., Buckley, G. A., Leong, A. F. T., **Carnibella, R. P.**, Fouras, A., Wallace, M. J., Hooper, S. B., (2015). “X-ray specks: low dose *in vivo* imaging of lung structure and function”. In: *Physics in Medicine and Biology* 60.18, pp. 7259–7276.

Contents

- 1 Introduction 1**
 - 1.1 Granular and porous materials 1
 - 1.1.1 *The lungs and alveoli* 2
 - Alveolar mechanics 2
 - Alveolar pathology 4
 - 1.2 Assessing respiratory function 4
 - 1.3 Functional lung imaging 5
 - 1.3.1 *X-ray imaging* 5
 - Computed tomography 5
 - Four-dimensional computed tomography 5
 - Phase contrast X-ray imaging 6
 - 1.3.2 *Magnetic Resonance Imaging* 9
 - 1.3.3 *Nuclear medicine* 10
 - 2D scintigraphy 10
 - Single-photon emission computed tomography 11
 - Positron emission tomography 11
 - 1.3.4 *Electrical impedance tomography* 12
 - 1.4 Background and theory: X-ray imaging 12
 - 1.4.1 *X-ray image formation* 13
 - X-ray interaction with matter 13
 - Absorption contrast imaging 13
 - Phase contrast imaging 14
 - Propagation-based phase contrast imaging 15
 - 1.4.2 *X-ray speckle* 17
 - 1.5 Problem statement 19
- 2 Particle sizing I: Sparsely packed particles 21**
 - 2.1 Article - Determining particle size distributions from a single projection image 23
- 3 Particle sizing II: Closely packed particles 31**
 - 3.1 Article - Decoding the structure of granular and porous materials from speckled phase contrast X-ray images 32
 - 3.2 Additional particle sizing validation 43
- 4 Bone segmentation and suppression 47**

4.1	Article - Single-exposure dual-energy-subtraction X-ray imaging using a synchrotron source	49
5	Measuring alveolar dimensions	57
5.1	Computed tomography bone subtraction and reprojection	58
5.1.1	<i>Phase contrast enhanced computed tomography</i>	58
5.1.2	<i>Bone segmentation and reprojection</i>	58
5.2	Spatial frequency filtering	60
5.3	Comparison of autocorrelation functions using bone subtraction and frequency filtering	62
5.4	Concluding comments on bone suppression	63
5.5	Article - Single-shot X-ray measurement of alveolar size distributions	64
6	Measuring dynamic alveolar function	73
6.1	Introduction	73
6.1.1	<i>A Direct Autocorrelation-Based Measurement Technique</i>	73
6.2	Measuring the Dynamic Behaviour of Alveoli	76
6.3	Estimating the total number of alveoli	79
6.3.1	<i>Theory</i>	79
	Estimating the number of alveoli from the alveolar distribution	79
	Estimating the number of alveoli using the alveolar tidal volume	79
6.3.2	<i>Method</i>	80
6.3.3	<i>Results/Discussion</i>	81
6.4	Regional analysis	83
6.4.1	<i>Theory</i>	83
6.4.2	<i>Method</i>	83
6.4.3	<i>Results/Discussion</i>	84
7	Conclusions	87
7.1	X-ray speckle	87
7.2	Functional alveolar imaging	88
7.3	Bone suppression	88
7.4	Addendum	88
7.5	Future work	89
7.6	Summary	90
	References	91
A	Appendix	99

A.1 The lognormal distribution 99

B Appendix 101

B.1 Article - X-ray specks: low dose in vivo imaging of lung structure and function 101

1 Introduction

The relatively recent development of phase contrast X-ray imaging techniques has allowed the lungs to be imaged with an unprecedented level of contrast. In a single projection X-ray image of the chest, the appearance of the highly speckled lung tissue is striking (Figure 1.1 left). Based on the hypothesis that this seemingly random speckle pattern encodes information about the size and shape of the air sacs in the lungs, the work in this thesis concerns the development of methods for tackling the inverse problem of retrieving information from the speckle. Ultimately, this will provide researchers with new tools for measuring alveolar size and function (Figure 1.1 right).

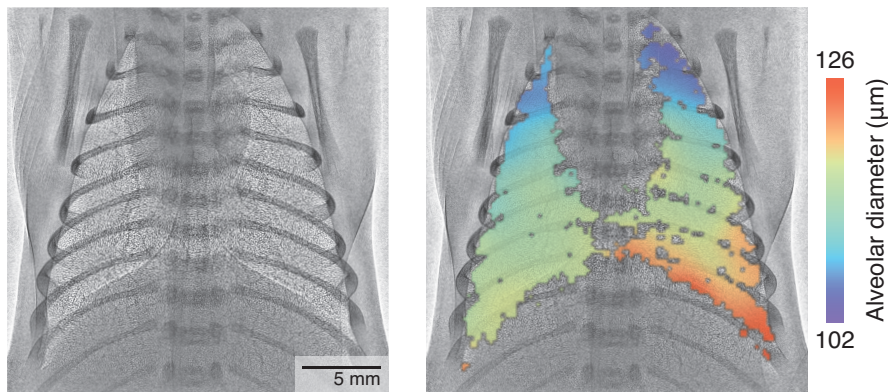


Figure 1.1: Left: Phase contrast X-ray of a rabbit pup showing the strongly speckled appearance of the lungs. Right: Overlay of measurements of regional alveolar diameter, obtained using the techniques developed in this thesis.

1.1 Granular and porous materials

Due to the presence of millions of air sacs (known as alveoli) the lungs can be considered as a type of porous material. Granular and porous materials are found all around us, both natural and man made. A granular material is typically defined as consisting of densely packed solid particles. Sand, powders and grains are examples. Jaeger et al. (1996) provide a more thorough coverage of this topic. In contrast, porous materials typically consist of a solid or liquid matrix containing empty voids. Concrete is an example of a man made porous material (Kumar and Bhattacharjee, 2003). Bone (Currey, 1988) and lung tissue (Lande and Mitzner, 2006) are examples of porous biological materials. The distinction between granular and porous materials isn't always clear. Soil, for example, is variously considered as both a granular and porous

material (Danielson and Sutherland, 1986). Colloids, substances consisting of microscopic particles suspended in a matrix, share many of the properties of granular and porous materials. The label: random heterogenous materials, is sometimes used to describe all these materials. Characteristically, they consist of multiple material phases in a random arrangement of grains or pores. The properties of these materials is usually intrinsically related to their structure, which is the motivation for studying the nature of these systems in detail. A comprehensive treatment of this topic can be found in the textbook by Torquato (2005).

The particular focus of this thesis is the porous nature and associated properties of the lungs, but the theory and techniques developed should be applicable across a range of so-called random heterogenous materials.

1.1.1 The lungs and alveoli

The mammalian lungs consist of three major components: the large conducting airways (in decreasing order of calibre these are the trachea, bronchi and bronchioles), the respiratory airways (respiratory bronchioles, alveolar ducts and alveoli), and an extensive network of blood vessels and capillaries. The process of respiration: the exchange of oxygen and carbon dioxide between inspired air and the bloodstream, takes place across the walls of the respiratory airways. Collectively the respiratory airways are also referred to as the lung parenchyma. It's estimated that approximately 80-90% of the total lung volume is composed of the lung parenchyma (Parent, 2015). Alveoli make up by far the largest component of the parenchyma. Human lungs contain hundreds of millions of thin walled alveoli (Ochs et al., 2004), giving them a sponge like appearance (Figure 1.2 right). The alveoli, therefore, are considered to be the primary respiratory units of the lungs.

Alveolar mechanics

Despite significant research into understanding the dynamics of the alveoli during respiration, there has been much conjecture as to the relative contributions of alveolar expansion and alveolar recruitment/derecruitment (Carney et al., 1999, Hajari et al., 2012). Alveolar recruitment refers to the opening of collapsed alveoli and derecruitment to the opposite: the collapse of open alveoli. One invasive technique used to investigate this question involved surgically placing a confocal microscope at the lung surface so that a small region of peripheral alveoli could be imaged (Namati et al., 2008). Questions were subsequently posed as to whether the peripheral alveoli sampled were representative of alveoli throughout the lungs (Cereda et al., 2011) and whether the insertion of the instrument itself could effect the alveoli being measured (Mertens et al., 2009). Another study using hyperpolarised MRI (Cereda et al., 2011)

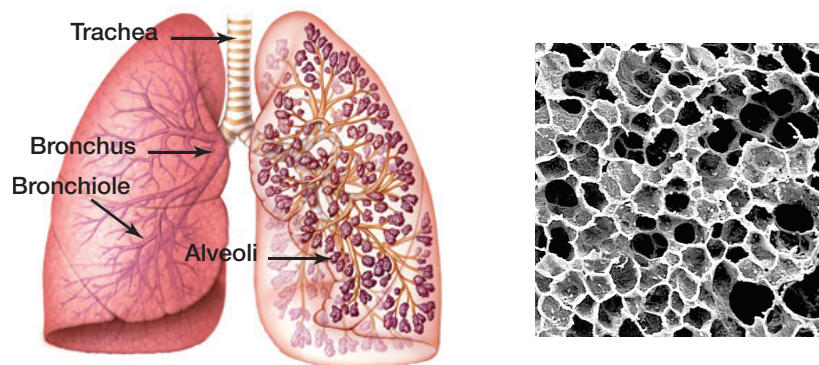


Figure 1.2: The conducting airways in the lung include the trachea, bronchi and bronchioles (left¹). However, most of the lung volume consists of millions of air sacs known as alveoli, seen here on electron microscopy (right²).

tackled the same problem but this technique also has multiple drawbacks, which will be covered in the discussion of functional MRI in section 1.3.2.

The use of mechanical ventilation is a potentially life saving intervention for a range of conditions. Just one example is in severely premature infants that require assisted ventilation to keep them alive, but at the same time are at risk of developing serious pulmonary complications such as bronchopulmonary dysplasia due to ventilator induced injury of their fragile, developing lungs (Jobe and Bancalari, 2001). Any means then of minimising lung damage produced by the administration of mechanical ventilation has the potential to improve outcomes in neonatal intensive care. The ability to monitor for over-distention or collapse of alveoli could form the basis of a method for optimising and tailoring individualised ventilation strategies.

In adult patients with acute respiratory distress syndrome (ARDS), a similar opportunity to improve the efficacy and minimise the harm caused by mechanical ventilation exists. ARDS is a condition that has a range of underlying causes, but is typically associated with sepsis and is characterised by widespread inflammation in the lungs. Currently, the mortality of this condition is high, ranging between about 10%–40% depending on severity, with the reasons for its poor response to mechanical ventilation and other therapies poorly understood (Crotti et al., 2001, Gattinoni et al., 2006, Rittayamai and Brochard, 2015).

¹[Untitled image of lung structure]. Retrieved September 3, 2015 from http://soft-matter.seas.harvard.edu/index.php/Pulmonary_Surfactant

²Lung SEM, Medium Mag [Online image]. Retrieved July 10, 2016 from <http://www1.udel.edu/biology/Wags/histopage/empage/er/er6.gif>

Alveolar pathology

Chronic obstructive pulmonary disease (COPD) is estimated to affect two million Australians and cost taxpayers \$8.8 billion dollars a year (McKenzie et al., 2010). Overwhelmingly, smoking is the most common cause of COPD. In developing countries air pollution is also a significant risk factor. A major component of COPD is emphysema, which is characterised by destruction of alveolar walls, minimising the surface area available for gas exchange. Additionally, the enlarged alveolar spaces result in increased lung compliance and work of breathing. The ability to screen for early disease could potentially improve outcomes for patients by motivating lifestyle changes or allowing the instigation of early therapies (Soriano et al., 2009).

1.2 Assessing respiratory function

Many technologies and techniques are currently available for studying the lungs and lung function. The first distinction that can be made is between those that measure structure and those that measure function. The term, functional testing or imaging, is used in the sense that these investigations can be used to qualify or quantify specific functional characteristics of the lungs. Measurements of volumes, flow rates, pressures and gas concentrations are all examples of functional measurements. If they are to be physiologically relevant, functional measurements need to be performed on living subjects.

The next distinction is between global and regional measurements. Pulmonary function tests are a group of investigations, of which spirometry is the most common, that measure a range of global parameters, typically at the mouth, as the patient performs a series of respiratory manoeuvres. Testing of regional function on the other hand is effectively synonymous with functional imaging; the various imaging modalities allowing non-invasive access to the lungs. These investigations typically produce measurements in the form of images, allowing measurements to be related to the underlying and surrounding anatomy. Much effort has been devoted to comparing global and regional techniques, in terms of their sensitivity as measures of damage or disease (Fan et al., 2001), and in trying to identify the unique applications for regional information.

The lungs are a dynamic organ and a healthy human takes around twelve breaths a minute. Smaller animals that may be used in preclinical studies can breathe significantly faster. This poses both an opportunity and a challenge for imaging techniques. The opportunity is to be able to derive functional measurements from the dynamic processes that are occurring over the respiratory cycle. The challenge is being able to image with sufficient temporal resolution to capture this information.

1.3 Functional lung imaging

1.3.1 X-ray imaging

Computed tomography

Computed tomography (CT) is a versatile tool commonly used in clinical practice for assessing lung pathology. In simple terms, the process involves taking X-rays images from multiple angles around a subject, which by means of computational inversion can be used to reconstruct a three-dimensional representation of the subject. Clinical scanners usually consist of a single X-ray source-detector pair, mounted within a gantry, that rotates around the subject. The time taken to acquire a complete scan therefore depends on the number of rows on the detector and the source-detector rotation speed. Current third generation scanners are capable of scanning a 16 cm tall region at around 3-4 frames per second with sufficient resolution to differentiate structures down to about half a millimetre in size (The ImPACT Group, 2009). Despite continuing advances in CT technology, today's scanners neither have enough detector rows nor are fast enough to image the entire breathing lung without significant motion artifact. Furthermore, their spatial resolution is insufficient for discriminating individual alveoli and, technical limitations aside, obtaining this level of resolution would necessarily come at the expense of increased radiation dose.

One method of overcoming the limited temporal resolution of CT scanners in the lungs is to acquire a pair of scans at end-expiration and end-inspiration, with the patient holding their breath for the duration of each scan. Following regional registration, the change in the volume of air within the lungs (a non-physiological tidal volume) can be estimated by the change in tissue CT number (Simon, 2000).

Another method is contrast enhanced tomography using a gas that is more radio-opaque than air, typically non-radioactive Xenon. Wash-in and wash-out studies (Chon et al., 2005) are performed by acquiring multiple scans after the gas is first administered until it reaches equilibrium, and then while the subject is returned to breathing regular air and the gas is washed out. In this respect it is similar to some of the nuclear medicine tests covered in section 1.3.3. The change in intensity or intensity gradient over the series of scans can be used to estimate regional ventilation. There are, however, drawbacks associated with the use of Xenon: the gas is expensive and requires additional hardware. It is also a strong anaesthetic.

Four-dimensional computed tomography

The logical extension of breath hold techniques, four-dimensional computed tomography (4D CT) is performed on patients who are allowed to breathe normally through-

out the duration of the scan. The acquisition of CT projections can either be gated to the respiratory cycle during acquisition or binned post acquisition (Pan et al., 2004). The result is a sequence of reconstructions (typically 2-20) corresponding to a series of time points during the respiratory cycle. Using a similar methodology to Simon (2000), Guerrero et al. (2006) used intensity-based analysis to measure regional ventilation.

Castillo et al. (2010) proposed an alternative approach to analysing 4D CT data using a deformable image registration technique to measure lung tissue motion. In another study, Reinhardt et al. (2008) compared measurements using a combined Xenon-enhanced and registration-based approach and found good agreement between the two. A different approach to measuring tissue motion, known as computed tomography particle image velocimetry (CT PIV) used a cross-correlation-based image analysis technique similar to that used in PIV (Dubsky et al., 2011).

The biggest drawback associated with all the 4D CT techniques is the radiation dose required. Even though the methods highlighted in this section don't require the resolution and associated dose necessary to discriminate structure at the level of the alveoli, the dose is that of multiple CT scans: effectively one at each time point. The gating or binning process also has a level of inherent inaccuracy and some degree of motion artifact, typically blurring, will be present.

A major advance upon CT PIV, which takes advantage of phase contrast in the lungs, four-dimensional X-ray velocimetry (4D XV; Figure 1.3) allows measurement of tissue motion and regional ventilation from significantly fewer projection angles, and therefore with less radiation dose than conventional 4D CT (Dubsky et al., 2012). This is achieved by directly reconstructing the motion field rather than using conventional CT reconstruction techniques.

As a point of clarification, although the references for both CT PIV and 4D XV are to synchrotron-based work (i.e. phase contrast imaging) they have been included in this section, rather than the next that covers phase contrast imaging techniques, because phase contrast is not an absolute requirement.

Phase contrast X-ray imaging

Conventional X-ray imaging suffers from poor tissue contrast in the lungs. The thin walled alveoli that make up much of the lung volume are weakly absorbing and produce little contrast in absorption-based X-ray imaging. Improving the contrast-to-noise ratio and increasing spatial resolution both come at the expense of requiring higher doses of radiation. The dose already associated with 4D protocols has been a significant barrier to their more widespread adoption in clinical practice. The risk of cancer from diagnostic X-ray techniques is real. Berrington de González et al. (2009) estimated that 1.5% to 2% of cancers in the US could be attributable to CT scans

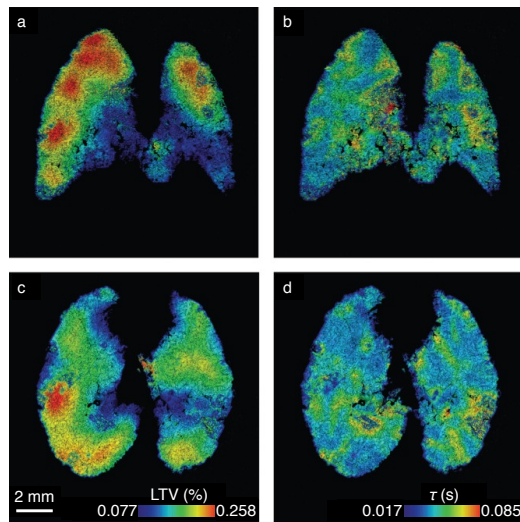


Figure 1.3: Tidal volume (left) and expiratory time constant (right) in a rabbit pup lung, obtained by 4D X-ray velocimetry. In coronal (a, b) and axial views (c, d). (Reproduced from Dubsy et al., 2012.)

alone.

A recent advance in X-ray imaging has been the development of phase contrast imaging techniques that exploit the wave nature of X-rays to produce additional contrast (described in detail in section 1.4.1). To date, propagation-based phase contrast imaging has proven to be the most practical of these techniques for medical imaging. In particular, it has proven to be a powerful technique for lung imaging (Kitchen et al., 2004). While alveoli are weakly absorbing, the abundant air-tissue interfaces found in the lungs are strong generators of phase modulation, resulting in up to an order of magnitude higher tissue contrast within the lungs (Kitchen et al., 2005), without the use of any contrast agents (Figure 1.4). Additionally, because the contrast produced by phase does not contribute to the absorbed radiation dose, there is also potential to minimise the dose. Kitchen et al. (2008) exploited phase contrast to dynamically measure regional volume during initial aeration of newborn rabbit pup lungs. The requirement of a coherent X-ray source dictated that the pioneering work on this technique was conducted on synchrotron X-ray beamlines but much progress has been made towards translating the technology to lab-based and clinical X-ray sources.

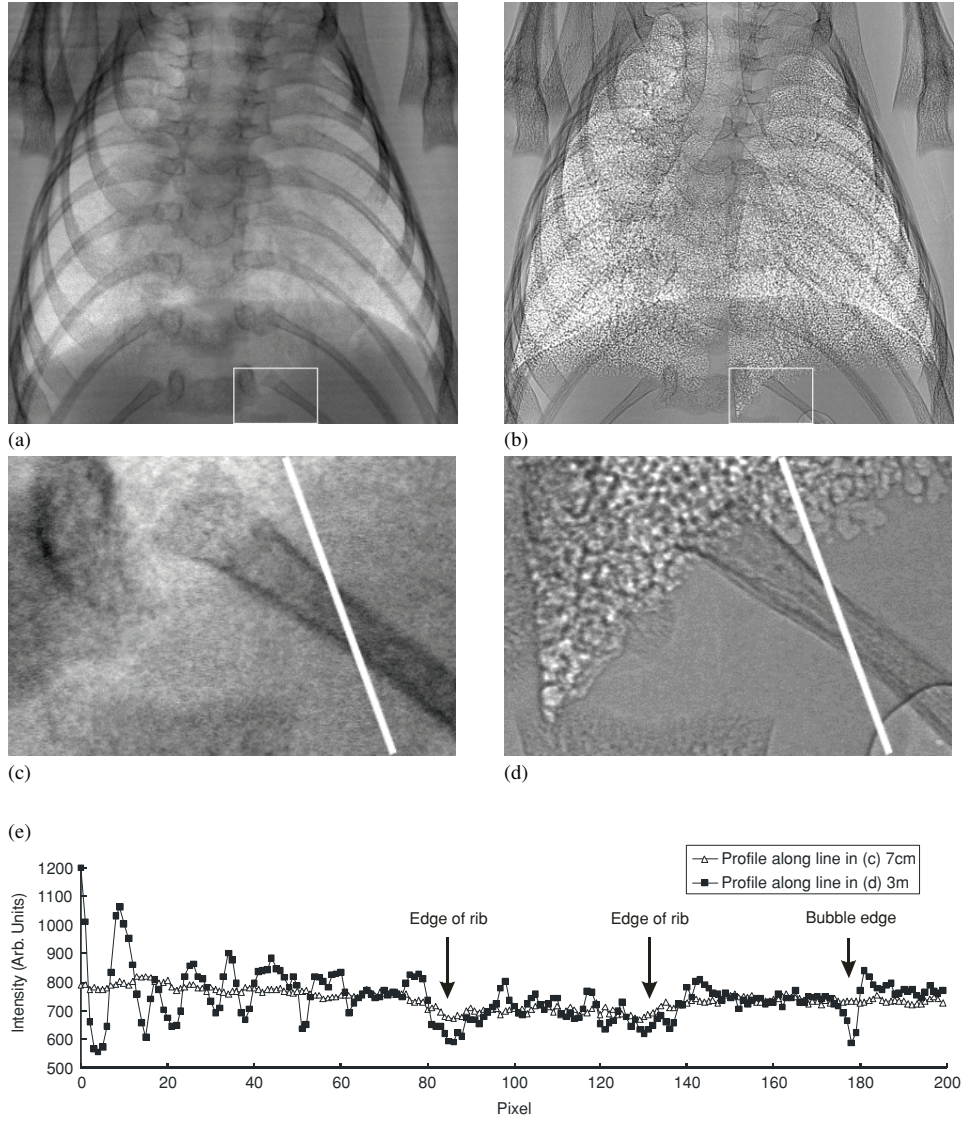


Figure 1.4: Absorption-based contrast (a,c) alongside propagation-based phase contrast (b,d) in a rabbit pup lung. The increased contrast in the lung tissue is evident on the radiographs and the line profiles in (e). (Reproduced from Lewis et al., 2005.)

Schleede et al. (2012) and Meinel et al. (2014) used a lab-based ‘compact light source’ with a grating-based technique to study emphysema in a mouse model. Dark field image contrast obtained using this technique is a result of the scattering power of the sample, which in turn is related to the alveolar size. They were able to show that emphysematous changes could be detected with greater sensitivity than conventional X-ray. However, the ability to quantitatively measure physiological parameters such as alveolar size has yet to be demonstrated. Grating-based techniques can also be technically challenging, and inefficient in respect to radiation dose because the gratings partially block the X-ray beam.

As a relatively new imaging modality, phase contrast X-ray imaging has many applications that have yet to be discovered. In this thesis it is the phase contrast produced by the alveoli that is exploited to make direct measurements of alveolar structure and function.

1.3.2 Magnetic Resonance Imaging

Alongside X-ray imaging, magnetic resonance imaging (MRI) is one of the mainstay modalities in clinical imaging. The working principle of MRI is the measurement of the electromagnetic field of charged nuclei in the body via radiofrequency signals that can be elicited by a combination of an applied magnetic field and radiofrequency stimulation. Typically it is the state of hydrogen atoms in the body, a major component of most tissues, that is measured. MRI imaging of the lungs has proven challenging due to both the low tissue density and the abundance of oxygen, which produces poor contrast and causes magnetic field inhomogeneities, respectively (Mills et al., 2003).

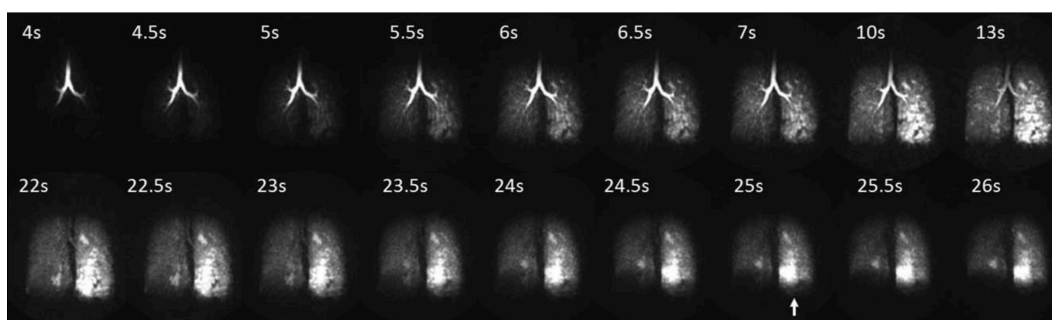


Figure 1.5: Single breath hyperpolarised ^3He MRI showing gas trapping occurring in an asthmatic patient’s left lower lobe. (Reproduced from Fain et al., 2010.)

However, the advent of contrast-based MRI techniques have been able to largely overcome these difficulties (Ebert et al., 1996). The use of hyperpolarised helium, ^3He , as a contrast agent has received the most attention (Fain et al., 2010; Figure 1.5).

In its most basic application, a single inhalation plus breath-hold scan can be used to identify regional filling defects (Samee et al., 2003). The development of fast MRI acquisition techniques have allowed dynamic measurement during wash-in and wash-out phases (Holmes et al., 2008, Wild et al., 2003), as well as over the respiratory cycle (Viallon et al., 2000, Salerno et al., 2001). Diffusion-weighted imaging measures the diffusivity of ^3He , producing maps of what is known as the apparent diffusion coefficient (ADC). Since diffusion is dependent on airway calibre, the ADC can be interpreted as an indirect measure of airway size. In the presence of disease, such as emphysema, increased heterogeneity has been observed (Salerno et al., 2002, Woods et al., 2006). Combining ADC measurements with a model of alveolar structure, Yablonskiy et al. (2002) were able to quantitatively estimate alveolar dimensions.

Despite offering much promise, hyperpolarised MRI techniques have significant drawbacks that have limited their more widespread use. Firstly, the production of hyperpolarised gas is both complicated and expensive. Compounding this, it has a limited shelf life of around 24 hours, necessitating that it either be produced on-site or express transported from a centralised production facility. The degree of hyperpolarisation of the gas is affected by the RF pulses used in MRI, and the fact that it rapidly diffuses in oxygen limits the range of imaging protocols that can be applied. As a result of all these factors, diffusion weighted imaging is plagued by both a lack of quantitative output and poor repeatability, frustrating attempts at longitudinal studies and comparative analyses across subjects and imaging sites (Gierada et al., 2009).

1.3.3 Nuclear medicine

Nuclear medicine refers to a group of imaging techniques based on imaging the radiation emitted by radioactive isotopes that have been administered to a patient. In the context of lung imaging, these isotopes are administered in the form of inhaled gases or aerosols. A common limitation of all of these methods is both poor temporal (approximately 30 s per projection) and spatial resolution (128×128 pixel coverage of the lungs). The total investigation time, from administration of isotopes to completion of imaging, can be hours.

2D scintigraphy

This technique, which has been around for over 40 years, typically uses krypton ($^{81\text{m}}\text{Kr}$) gas or aerosolised technetium ($^{99\text{m}}\text{Tc}$) as a radioisotope. These substances emit gamma radiation, which is detected by a specialised gamma camera. Images are captured during the wash-in, equilibrium and wash-out phases and can be used to identify localised changes in airflow. In addition to measuring airflow, injected

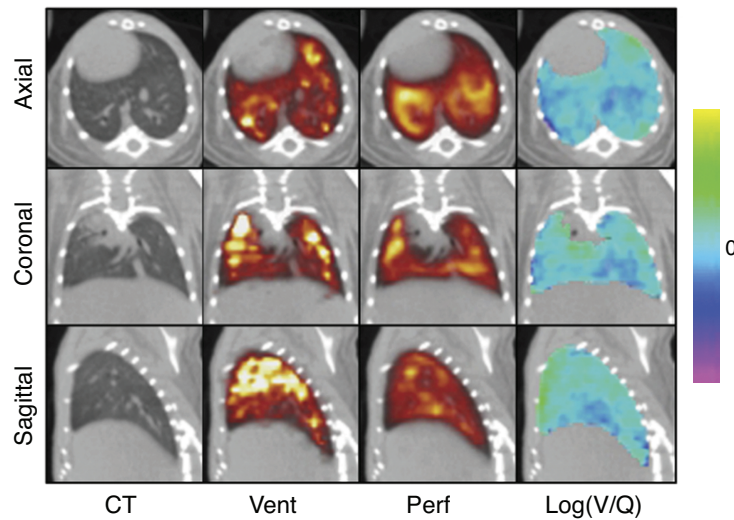


Figure 1.6: SPECT/CT slices of a mouse lung. Ventilation and perfusion heatmaps are coloured on an increasing scale from red to white. The color bar relates to the $\log(V/Q)$ heatmaps. (Reproduced from Jobse et al., 2012.)

radioisotopes can also be used to measure perfusion.¹ The most common clinical application has been the combined ventilation/perfusion scan used to assist in the diagnosis of pulmonary embolism. A ventilation/perfusion mismatch may be apparent in the event of an embolism.

Single-photon emission computed tomography

Single-photon emission computed tomography (SPECT) is essentially the 3D volumetric equivalent of 2D scintigraphy (Bajc et al., 2010). Increasingly commonly it is being performed together with X-ray CT to allow mapping SPECT derived functional measurements of the underlying anatomy (Jobse et al., 2012; Figure 1.6). SPECT is one of the functional techniques that has shown promise as a tool for the early detection of COPD (Norberg et al., 2014).

Positron emission tomography

Positron emission tomography (PET) is a related but slightly different technique based on the emission of positrons by a radioactive substance that then proceed to produce gamma radiation when they interact with adjacent electrons. It also differs from SPECT in that the contrast agent is given intravenously, with the nitrogen-based radiotracer diffusing from the pulmonary capillaries into the alveoli (Harris

¹Perfusion refers to the delivery of blood to biological tissues.

and Schuster, 2007). To date it hasn't received as much attention as SPECT as a technique for studying lung function.

1.3.4 Electrical impedance tomography

Different tissue types in the body have different electrical conductivities and permittivities depending on their free ion concentrations. Electrical impedance tomography (EIT) exploits these variations by sampling impedance across pairs of electrodes placed around the body and reconstructing the internal electrical properties (Cheney et al., 1999; Figure 1.7). It is ideally suited to lung imaging because lung tissue has significantly lower conductivity than other tissue types, resulting in strong image contrast (Victorino et al., 2004). This technique can be quite useful for monitoring the gross anatomy of the breathing lung in real-time. However, its broader utility is limited since imaging is restricted to a single slice and even within that slice spatial resolution is low.

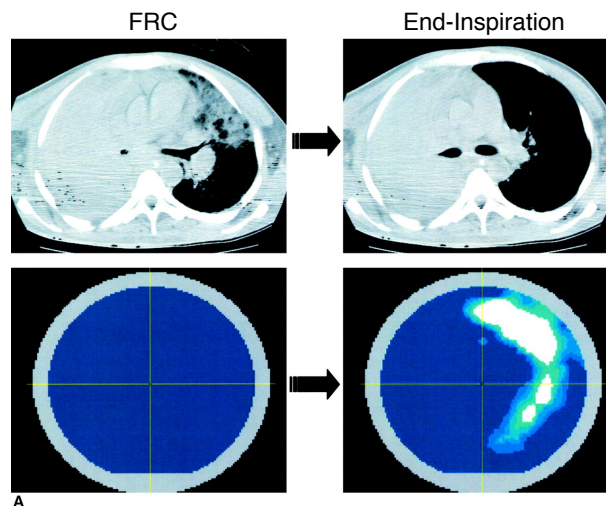


Figure 1.7: EIT (lower frames) and CT (upper frames) images from a patient at the start (left) and end (right) of an inflation manoeuvre. The EIT images show the relative change in impedance. Air is dark on CT and an increase in air is bright on EIT. No air is seen inflating the right lung — the airway has been completely obstructed by a mass. (Reproduced from Victorino et al., 2004.)

1.4 Background and theory: X-ray imaging

Having completed a survey of the different modalities and techniques for performing functional lung imaging, it is apparent that there is limited capability to study the

mechanics of the alveoli in vivo. This thesis describes the development of a new technique for measuring alveolar function, based on the analysis of X-ray lung speckle produced by phase contrast imaging.

But before proceeding, some background on X-ray theory is necessary. This section will cover both some of the fundamental theory concerned with describing the behaviour of X-ray radiation as well as important developments and the state of the art in phase contrast imaging and X-ray speckle. It provides a more thorough background to the work undertaken than could be covered in the papers that constitute the majority of this thesis.

1.4.1 X-ray image formation

X-ray interaction with matter

Absorption contrast imaging

The mechanisms describing the interaction of X-rays with matter that are relevant at the X-ray energies used in radiography are photoelectric absorption and Compton scattering. In biological tissues, below about 25 keV photoelectric absorption is the dominant interaction, with Compton scattering becoming more significant at higher energies. When X-rays are transmitted through matter, their energy is attenuated as a result of the aforementioned interactions.

In conventional X-ray imaging (sometimes referred to as absorption contrast imaging) it is the the process of X-ray attenuation that produces what we recognise as an X-ray image or radiograph. That is, the difference in X-ray attenuation between different materials or a given material of varying thickness results in a difference in intensity (i.e. contrast) at the X-ray detector. The attenuation of X-ray radiation as it passes through a medium is described by the Beer-Lambert law:

$$I(t) = I_0 e^{-\left(\frac{\mu}{\rho}\right)\rho t} \quad (1.1)$$

where $I(t)$ is the X-ray intensity leaving the medium, I_0 is the incident X-ray intensity, $\frac{\mu}{\rho}$ is the medium's mass attenuation coefficient, μ is the linear attenuation coefficient, ρ is density and t is thickness.

The total linear attenuation coefficient is the sum of the linear attenuation coefficients due to each of the different interaction mechanisms:

$$\mu = \mu_{photo} + \mu_{comp} + \mu_{other}$$

where μ_{photo} is the photoelectric absorption coefficient, μ_{comp} is the Compton scattering coefficient and μ_{other} accounts for other less significant interactions.

Mass attenuation coefficients for elements and a range of materials have been calculated using theory and experimental data and are available online from NIST (Berger et al., 2012).

Phase contrast imaging

The two main advantages of imaging with a synchrotron light source are the high brilliance (intensity) and high coherence (both temporal and spatial). Temporal coherence refers to the degree of correlation of a wavefield between two points along the direction of propagation and is an indication of the monochromaticity of a source. Spatial coherence refers to the degree of correlation of a wavefield between two points perpendicular to the direction of propagation and is a measure of the uniformity of the wave front. Diffraction and interference produced by coherent radiation is the basis of phase contrast X-ray imaging.

As an electromagnetic wave, X-rays carry information in the form of both intensity and phase. X-ray detectors are instruments that measure intensity. Retrieving information about phase isn't as straightforward. Typically approaches to measuring the phase of electromagnetic radiation involve some means of converting phase information to intensity.

X-ray interferometry uses silicon crystals to separate and then recombine X-ray beams with one of the separated beams having been directed through the sample. Phase modulation produced within the sample can be visualised when the beams are recombined as interference patterns.

Analyser-based approaches (Chapman et al., 1997) also use a silicon (analyser) crystal to separate the different phase components in the X-ray beam after it has passed through the sample.

Propagation-based phase contrast imaging (PBI), which has already been covered in some detail, encodes phase information in the interference produced when the X-rays that have passed through the sample are allowed to propagate a sufficient distance before reaching the detector (Snigirev et al., 1995 Wilkins et al., 1996).

Grating-based X-ray imaging (Pfeiffer et al., 2007) uses phase gratings, rather than a crystal, to generate interference patterns either before or after the incident beam has been perturbed by the sample.

In this work PBI is used exclusively. For medical imaging, particularly dynamic imaging, this technique has a number of advantages. In terms of efficiency, it makes use of all the intensity available unlike all other techniques which either partially block or selectively filter the beam. Efficiency is especially important for performing high speed imaging of dynamic biological systems. Crystal and grating-based techniques also require that their optical elements are highly stable, which can pose a challenge. PBI on the other hand is straightforward to implement and requires no

specialist apparatus besides a coherent X-ray source.

In the next section a theoretical overview of PBI is provided, specifically outlining the method of modelling PBI that is integral to the technique developed in this thesis.

Propagation-based phase contrast imaging

Wave theory gives us the framework for describing both the intensity and phase of X-ray radiation. A coherent, parallel, X-ray beam produced at a synchrotron can be regarded as a plane electromagnetic wave, with both wave amplitude and phase accounted for by the complex function:

$$U = A_0 e^{i\varphi}$$

where A_0 is the peak wave amplitude and φ is the phase shift of the wave.

Now in addition to X-ray attenuation we incorporate the phase shift that occurs as the wavefield passes through a sample (Figure 1.8) by use of a projected thickness approximation (Pogany et al., 1997). Essentially, the approximation neglects diffraction within the sample, which is valid when the sample thickness is small compared to the propagation distance, z_p . The phase shift within the sample is a function of the complex index of refraction:

$$n = 1 - \delta + i\beta$$

where the refractive index decrement

$$\delta = \frac{r_e \lambda}{k} \sum_i n_i (f_1)_i$$

and r_e is the classical electron radius, λ is the wavelength, the wavenumber $k = \frac{2\pi}{\lambda}$, n_i is the concentration of atom i per unit volume and f_1 is the real part of the forward atomic scattering factor. β is directly related to the linear attenuation coefficient:

$$\mu = 2k\beta$$

For a single material we can calculate the phase shift from the refractive index decrement:

$$\varphi = -k\delta t$$

Factoring in both the attenuation and the phase shift that occurs as the wavefield passes through the sample, the wavefield exiting the sample as a function of its projected thickness can be expressed as:

$$U_{exit}(x, y) = A_0 e^{-ik\delta T(x,y)}$$

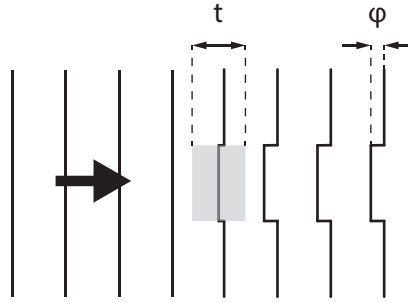


Figure 1.8: As X-rays pass through an object of thickness t , the phase of the wavefront that leaves the object lags the original wavefront by φ .

where $T(x, y)$ is the projected thickness of the sample. Multiple materials can be modelled by treating each separately. For practical purposes, it is often convenient to treat air as a vacuum.

Phase contrast in PBI is produced by allowing the wavefield to continue propagating beyond the sample. The interference that is produced is captured at the detector plane. A convenient means of calculating the propagated wavefield is by use of the angular spectrum method (Nieto-Vesperinas, 2006). Using this method, the complex wavefield is deconstructed into a collection of plane waves travelling in different directions (hence the term angular spectrum). The angular spectrum representation of the wavefield is obtained by simply taking its Fourier transform. In the angular frequency domain, the wavefield is easily propagated a distance z_p (Figure 1.9) by multiplying by the propagation term:

$$e^{iz_p \sqrt{k^2 - k_x^2 - k_y^2}}$$

where k_x and k_y are the coordinate axes in the angular frequency domain.

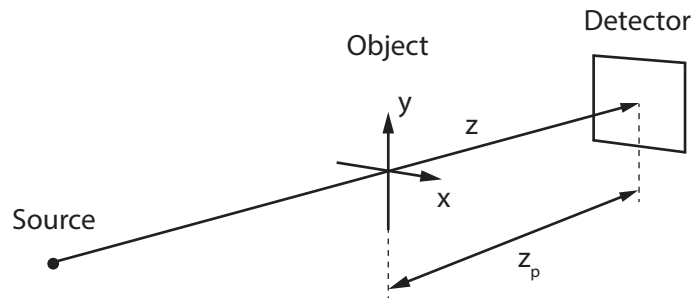


Figure 1.9: Configuration of source, object and detector for propagation-based phase contrast imaging

Combining all the components that have been described so far, the propagated

wavefield at the detector plane can be expressed as

$$U_{det}(x, y, z = z_p) = \mathcal{F}^{-1} \left\{ \mathcal{F} \left\{ A_0 e^{-ik\delta T(x,y)} \right\} e^{iz\sqrt{k^2 - k_x^2 - k_y^2}} \right\}$$

where \mathcal{F} and \mathcal{F}^{-1} are Fourier and inverse Fourier transforms, respectively.

Finally, since intensity is proportional to the squared magnitude of the wavefunction we square both sides and replace A_0 with the attenuated X-ray intensity according to equation 1.1. The result is the following expression for the intensity observed at the detector, which allows us to simulate the generation of X-ray images of a sample with known internal geometry and material properties:

$$I_{det}(x, y, z = z_p) = I_0 e^{-\mu T(x,y)} \left| \mathcal{F}^{-1} \left\{ \mathcal{F} \left\{ e^{-ik\delta T(x,y)} \right\} e^{iz\sqrt{k^2 - k_x^2 - k_y^2}} \right\} \right|^2$$

1.4.2 X-ray speckle

Finally, we return to the problem posed at the beginning of this chapter. That is, the interpretation of the speckled pattern apparent in the propagation-based phase contrast projection images of lungs and other granular and porous materials.

In optics theory speckle has a specific definition. When the wavefronts of coherent radiation interfere with each other as a result of a random scattering process, the wavefront produced is the result of the addition of the amplitude and phase of each of the individual scattered waves. If the wave amplitude and phase are treated as vectors, the process can be visualised by adding the vectors graphically, producing a plot that resembles a random walk. When the phase of the resultant wavefront is uniformly distributed within the interval $(-\pi, \pi)$, the speckle is considered fully developed. Speckle that doesn't satisfy this requirement, either due to partial coherence or limited scattering, is referred to as being partially developed (Goodman, 2006).

Lung speckle in PBI is partially developed speckle. Kitchen et al.(2004) modelled lung alveoli as spheres, producing phase maps in which vortices can be seen as the phase wraps the $(-\pi, \pi)$ interval. In these same simulations we also see structure in the phase map; in other words the phase is not uniformly distributed.

In the case of fully developed speckle, in most circumstances, the speckle size is independent of the size of the scatterers (Goodman, 2006). However, a near-field regime has been described (Giglio et al., 2000) in which the size of the speckle and the scatterers is correlated. This type of speckle has been referred to as 'near-field speckle'. It is worth noting that the definition of this near-field differs from the more widely used optics definition.² The theory holds for a scattering volume that produces

²Classically the near field is defined by the Fraunhofer distance such that $z < \frac{2d^2}{\lambda}$ where z is the distance from the scatterer, d is the diameter of the scatter and λ is the wavelength of the radiation. The condition for near-field speckle differs in that $z_{nfs} < \frac{dD}{\lambda}$ where D is the diameter of the beam of

a delta-correlated field (i.e. fully developed speckle), which requires that the length-scale of the scatters is not much greater than the wavelength of the radiation; that is they are effectively point scatters. This implies a far more restrictive regime than the requirement of the near-field speckle distance alone suggests.

Ferri et al. (2004) developed a technique they called heterodyne near-field scattering to essentially perform SAXS style analysis of particle systems such as colloids using both visible and X-ray radiation (Cerbino et al., 2008).

While Cerbino et al. (2008) were able to extend the definition of the near-field speckle to X-ray scattering, it was no longer independent of propagation distance and required the use of a correction factor, which was, coincidentally, the phase contrast transfer function (Pogany et al., 1997). Given that the length-scale of the alveoli is much greater than the X-ray wavelength, the framework provided by phase contrast theory is arguably both more appropriate and more useful for describing the nature of this speckle. The fact that the scatterer and speckle size are correlated can intuitively be explained by considering the narrow range of scattering angles (Kitchen et al., 2004). In this case, the resultant image produced by PBI will still strongly resemble the image of the superpositioned scatters rather than the uniformly random field of fully developed speckle.

In chapter 2 a more rigorous theoretical proof of the speckle pattern being the result of the superposition of the constituent scatterers or particles, in the context of phase contrast X-ray imaging, is given. This concept is fundamental to all the work that follows in this thesis because it forms the basis for being able to retrieve information about the morphology of the particles in such a system from their speckle image.

1.5 Problem statement

Many different processes in the lungs, both physiological and pathological, involve its smallest functional units — the alveoli. Yet the ability to directly study the behaviour of the alveoli *in vivo* is lacking.

Dynamic imaging can be a powerful tool for studying function and an array of dynamic techniques have been developed to assess lung function. These techniques make use of a range of approaches from imaging the flow or diffusion of gas in the lungs to measuring the motion of the lung tissue. However, of all the methods covered in this chapter only hyperpolarised MRI is capable of making measurements of alveolar function and its limitations are significant.

The development of phase contrast X-ray imaging allows us to visualise the fine structure of the lungs for the first time without an impractically high radiation dose. Phase contrast computed tomography can produce remarkably high resolution images of the alveoli but lacks for both spatial and temporal resolution *in vivo*.

The interpretation or decoding of two-dimensional phase contrast images of lung speckle presents an opportunity to observe the dynamic behaviour of the alveoli in the breathing lung in real-time. The development of such a technique is the primary focus of the work in this thesis.

Secondary objectives are to further develop our understanding of the origins and behaviour of speckle in the lungs (and other granular and porous materials) and to develop the necessary infrastructure, in terms of image analysis techniques and hardware, to facilitate the segmentation and analysis of the lung fields in two-dimensional projection images.

This thesis consists of five chapters, four of which are based on peer reviewed papers. In chapter 2 we begin by exploring the nature of X-ray speckle produced by sparsely packed granular and porous materials. The feasibility of extracting particle properties will be demonstrated while highlighting the effect of packing fraction and porosity. This groundwork is extended in chapter 3 to densely packed particle systems. A custom solver is developed to tackle the inverse problem of decoding the speckle and the accuracy of the technique is demonstrated on samples of glass microspheres. Chapter 4 outlines the development of a dual energy X-ray imaging system for material separation. The system can be used to achieve bone suppression in chest X-ray images allowing clear access to the lungs fields for the purpose of applying speckle analysis techniques. In chapter 5 we look at an alternative means of analysing lung speckle without the need for bone suppression. Images of inflation fixed lungs are analysed and the results presented. In the final chapter the technique is extended to dynamic *in vivo* lung imaging with a demonstration of the capability to perform regional analysis of alveolar dynamics in a breathing lung.

2 Particle sizing I: Sparsely packed particles

The arrangement and packing of grains or pores in a constrained system presents a complex mathematical problem. Key variables include the shape of the grains or pores, the diversity of shapes and sizes, and the way in which they have been arranged. As outlined in the previous chapter, the primary application of this work is in studying the porous structure of the lungs. However, the theory and methodology described in this thesis are also applicable across a range of other materials.

Packing in granular and porous materials can be classified as either regular or irregular. Regular packing usually implies that particles are of uniform shape and size; for example cubic and hexagonal arrangements of equal size spheres. More commonly in nature, granular and porous materials have an irregularly packed structure. The description, random packing, is often used synonymously with irregular packing because irregular packing can be achieved by randomly placing or pouring particles. Similarly, the formation of the lungs, and specifically the alveoli, is a process strongly influenced by randomness.

Packing fraction describes the volume of particles as a fraction of the total volume of the system and is equivalent to the porosity of a porous material. Random close-packing describes a maximally packed state that for monodisperse spheres has a packing fraction of 63.4 percent (Song et al., 2008). Polydisperse spheres and non-spherical particles can achieve even higher packing fractions. Throughout this work the terms packing fraction and porosity are used interchangeably. The terms close and dense packing are also used interchangeably to refer to a near maximal packing state. The term sparse packing is used to refer to packing fractions less than around 50 percent.

Phase contrast X-ray imaging allows us to visualise the superpositioned projections of the millions of alveoli found in the lungs. It was hypothesised that this information can be decoded to tell us about the size and shape of the alveoli. This is an inverse problem. The first step towards obtaining a solution to an inverse problem is to solve the forward problem. In this case the forward problem amounts to describing the image a particular arrangement of packed particles is expected to produce. The Percus Yevick approximation (Percus and Yevick, 1958) can be used to describe the three dimensional correlation between randomly packed spheres for packing fractions less than about 40 percent. However, an analytical or numerical means for describing more densely packed random systems of particles could have not been described in the literature.

In optics, diffraction theory tells us that, besides a scaling factor, the diffraction pattern produced by multiple randomly located apertures is the same as that produced

by a single aperture (Lipson et al., 2010). It was hypothesised that the same theory could similarly be applied to the pattern formed by superposing the projected image of randomly packed particles in Fourier space. This would allow the forward problem to be treated as a linear system: as the weighted sum of the contribution of different particles. It would also make the inverse problem a relatively simple linear problem. The catch, as it turns out, lies in the required randomness of the particles. As the packing fraction or porosity of the particles increases, so too the degree of randomness decreases. This is because in a system of non-penetrating particles, the position of particles is restricted to space unoccupied by other particles; whereas to be truly random, a particle must be allowed to reside anywhere. This problem can also be identified and explained by examining the spatial autocorrelation function of such a system. As the packing fraction increases, periodic oscillations begin to develop in the autocorrelation function, highlighting that the positions of the particles are correlated. This implies that particles are more or less likely to be found at certain distances from their neighbours.

Unfortunately, or perhaps fortunately given their important role, alveoli in humans, and more generally in mammalian lungs, are densely packed. The respiratory portion of the lungs (the parenchyma: respiratory bronchioles to alveoli), which accounts for over 90 percent of the lung volume (Weibel, 1963; Ochs et al., 2004), has an estimated alveolar fraction or porosity of around 65 percent (Ochs et al., 2004).

However, it was found that at packing fractions of less than ten per cent, one can effectively assume that randomness dominates and a linear system model is valid. The relative simplicity of this approach prompted further investigation, specifically as a means of validating the hypothesis that the information contained within X-ray speckle produced by a granular or porous material could be decoded. If this could be demonstrated in a sparsely packed system, it would lay the groundwork for the development of the tools required to tackle the more difficult problem of decoding the structure of a close-packed systems, such as the lungs. Additionally, there may be applications for such a technique in other areas where relatively sparsely packed systems of particles are to be found.

2.1 Article - Determining particle size distributions from a single projection image

The following paper was published in 2012 in *Optics Express*. This work was co-authored by M.J. Kitchen and A. Fouras. The paper is reproduced in this thesis directly from the published version.

Monash University

Declaration for Thesis Section 2.1

Declaration by candidate

In the case of Section 2.1, the nature and extent of my contribution to the work was the following:

Nature of contribution	Extent of contribution (%)
Initiated the paper, conducted experiments, performed analysis and wrote manuscript.	90

The following co-authors contributed to the work. If co-authors are students at Monash University, the extent of their contribution in percentage terms must be stated:

Name	Nature of contribution	Extent of contribution (%) for student co-authors only
M. J. Kitchen	Performed experiments, supported analysis and revised manuscript.	NA
A. Fouras	Performed experiments, supported analysis and revised manuscript.	NA

The undersigned hereby certify that the above declaration correctly reflects the nature and extent of the candidate's and co-authors' contributions to this work*.

Candidate's Signature  Date 11/12/2016

Main Supervisor's Signature  Date 11/12/2016

*Note: Where the responsible author is not the candidate's main supervisor, the main supervisor should consult with the responsible author to agree on the respective contributions of the authors.

Determining particle size distributions from a single projection image

R. P. Carnibella,^{1,2,*} M. J. Kitchen,³ and A. Fouras^{1,2}

¹Department of Mechanical and Aerospace Engineering, Monash University, Melbourne 3800, Australia

²Division of Biological Engineering, Monash University, Melbourne 3800, Australia

³School of Physics, Monash University, Melbourne 3800, Australia
richard.carnibella@monash.edu

Abstract: Imaging techniques employed to measure the structure of granular, particulate and porous materials are limited by scale, temporal resolution and, for biological samples, radiation exposure. This paper describes a technique for determining the distribution of particle sizes in opaque samples, for particle volume fractions less than ten percent, using a single projection radiograph. The method is based on the derived property of the additivity of the particles' spatial autocorrelation function in projection images. Simulations and experiments demonstrate the ability to use this property to determine the distribution of particle sizes in a material.

©2012 Optical Society of America

OCIS codes: (100.2960) Image analysis; (110.7440) X-ray imaging; (050.5080) Phase shift; (350.4990) Particles.

References and links

1. M. E. Davis, "Ordered porous materials for emerging applications," *Nature* **417**(6891), 813–821 (2002).
2. H. A. Makse, S. Havlin, P. R. King, and H. E. Stanley, "Spontaneous stratification in granular mixtures," *Nature* **386**(6623), 379–382 (1997).
3. C. N. Davies, *Aerosol Science*, First ed. (Academic Press, 1966).
4. R. A. Dobbins, L. Crocco, and I. Glassmans, "Measurement of Mean Particle Sizes of Sprays from Diffractively Scattered Light," *AIAA J.* **1**(8), 1882–1886 (1963).
5. B. P. Flannery, H. W. Deckman, W. G. Roberge, and K. L. D'Amico, "Three-Dimensional X-ray Microtomography," *Science* **237**(4821), 1439–1444 (1987).
6. T. Narayanan, O. Diat, and P. Bösecke, "SAXS and USAXS on the high brilliance beamline at the ESRF," *Nucl. Instrum. Meth. A* **467–468**, 1005–1009 (2001).
7. L. Rigon, H.-J. Besch, F. Arfelli, R.-H. Menk, G. Heitner, and H. Plothow-Besch, "A new DEI algorithm capable of investigating sub-pixel structures," *J. Phys. D Appl. Phys.* **36**(10A), A107–A112 (2003).
8. H. Suhonen, M. Fernández, A. Bravin, J. Keyriläinen, and P. Suortti, "Refraction and scattering of X-rays in analyzer-based imaging," *J. Synchrotron Radiat.* **14**(6), 512–521 (2007).
9. R. Cerbino, L. Peverini, M. A. C. Potenza, A. Robert, P. Bosecke, and M. Giglio, "X-ray-scattering information obtained from near-field speckle," *Nat. Phys.* **4**(3), 238–243 (2008).
10. A. Snigirev, I. Snigireva, V. Kohn, S. Kuznetsov, and I. Schelokov, "On the possibilities of x-ray phase contrast microimaging by coherent high-energy synchrotron radiation," *Rev. Sci. Instrum.* **66**(12), 5486–5492 (1995).
11. S. W. Wilkins, T. E. Gureyev, D. Gao, A. Pogany, and A. W. Stevenson, "Phase-contrast imaging using polychromatic hard X-rays," *Nature* **384**(6607), 335–338 (1996).
12. M. J. Kitchen, D. Paganin, R. A. Lewis, N. Yagi, K. Uesugi, and S. T. Mudie, "On the origin of speckle in x-ray phase contrast images of lung tissue," *Phys. Med. Biol.* **49**(18), 4335–4348 (2004).
13. M. D. Alaimo, D. Magatti, F. Ferri, and M. A. C. Potenza, "Heterodyne speckle velocimetry," *Appl. Phys. Lett.* **88**(19), 191101 (2006).
14. A. Fouras, J. Dusing, R. Lewis, and K. Hourigan, "Three-dimensional synchrotron x-ray particle image velocimetry," *J. Appl. Phys.* **102**(6), 064916 (2007).
15. A. Fouras, D. Lo Jacono, C. V. Nguyen, and K. Hourigan, "Volumetric correlation PIV: a new technique for 3D velocity vector field measurement," *Exp. Fluids* **47**(4-5), 569–577 (2009).
16. S. Dubsy, R. A. Jamison, S. C. Irvine, K. K. W. Siu, K. Hourigan, and A. Fouras, "Computed tomographic x-ray velocimetry," *Appl. Phys. Lett.* **96**(2), 023702 (2010).
17. C. V. Nguyen, J. Carberry, and A. Fouras, "Volumetric-correlation PIV to measure particle concentration and velocity of microflows," *Exp. Fluids* (in press).
18. D. Paganin, S. C. Mayo, T. E. Gureyev, P. R. Miller, and S. W. Wilkins, "Simultaneous phase and amplitude extraction from a single defocused image of a homogeneous object," *J. Microsc.* **206**(1), 33–40 (2002).

#164928 - \$15.00 USD Received 19 Mar 2012; revised 25 May 2012; accepted 28 May 2012; published 28 Jun 2012
(C) 2012 OSA

2 July 2012 / Vol. 20, No. 14 / OPTICS EXPRESS 15962

19. A. Lipson, S. G. Lipson, and H. Lipson, *Optical Physics*, 4th ed. (Cambridge University Press, 2010).
20. M. Nieto-Vesperinas, *Scattering And Diffraction in Physical Optics*, 2nd ed. (World Scientific Pub Co Inc, 2006).
21. A. Pogany, D. Gao, and S. W. Wilkins, "Contrast and resolution in imaging with a microfocus x-ray source," *Rev. Sci. Instrum.* **68**(7), 2774–2782 (1997).
22. E. L. Crow and K. Shimizu, *Lognormal Distributions: Theory and Applications* (M. Dekker, 1988).
23. S. Goto, K. Takeshita, Y. Suzuki, H. Ohashi, Y. Asano, H. Kimura, T. Matsushita, N. Yagi, M. Isshiki, H. Yamazaki, Y. Yoneda, K. Umetani, and T. Ishikawa, "Construction and commissioning of a 215-m-long beamline at SPring-8," *Nucl. Instrum. Meth. A* **467–468**, 682–685 (2001).
24. C. Kittel, *Introduction to Solid State Physics*, 8th ed. (Wiley, 2005).

1. Introduction

Granular, particulate and porous materials and systems are of interest across a spread of disciplines including material, chemical, geological and biological science and engineering. Many existing and new porous materials have special properties that are a consequence of their unique structure [1]. To geologists, the behavior of many natural systems, such as those comprised of sand, soil and snow, can be understood by studying the behavior of granular media [2]. As such, simple methods to characterize these materials and systems are in demand.

Characterization techniques based on optical scattering [3,4] are well established but are limited to non-opaque samples. X-ray computed tomography (CT) and microtomography [5] are capable of imaging the structure of opaque samples, but suffer comparatively poor temporal resolution; furthermore, ionizing radiation dose can be problematic for biological samples. Diffraction based X-ray techniques [6–9] have to date been limited to studying particulates no larger than a few micrometres or have only been qualitative in nature.

In this paper we show that for low volume fraction suspensions of particles, the spatial autocorrelation function (SAF) of a projection image of the particles is additive, and use this property to determine the distribution of particle sizes from a single image.

2. Theory

Many systems of interest consist of spheroidal particles dispersed in a pseudo-random arrangement within some medium. Planar X-ray imaging of such a system can produce a discernible speckle pattern. However, when the difference in attenuation between the particles and medium is small, the speckle contrast is poor. Propagation-based phase contrast X-ray imaging (PCXI) [10,11], using a partially coherent source, can produce significantly higher speckle contrast [9,12]. A typical speckle pattern can be seen in Fig. 1.

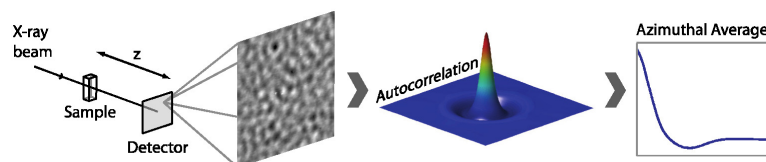


Fig. 1. Schematic of propagation-based phase contrast X-ray imaging setup and image processing steps. The sample and detector are in-line and z is the propagation distance for phase contrast imaging. A region of a typical X-ray image has been magnified to highlight the speckled appearance produced by particles. A spatial autocorrelation is performed; which is azimuthally averaged to produce the final one-dimensional autocorrelation function.

To obtain useful information from these speckled images, a statistical measure such as the SAF can be used. In the context of heterodyne imaging of particles, Alaimo *et al.* derive the property of linearity: that the autocorrelation function is a weighted sum of contributions from all the particles, which they use to recover the velocity distribution from a seeded flow [13]. For a side scattering (non-heterodyne) particle image velocimetry configuration, Fouras *et al.*

proposed that the total cross-correlation function is equal to the sum of the cross-correlation functions at each depth, and used this notion to perform three-dimensional velocity measurements from two-dimensional images [14–16]. Nguyen *et al.* extended this concept and used the SAF to infer particle concentration as a function of depth [17]. In what follows, the linearity property of the SAF: that the SAF of a projection image is equal to the sum of the SAF of each particle, will be justified in the context of X-ray imaging, with or without phase contrast, and be used to determine the distribution of particle sizes.

For a sample comprised of randomly oriented particles or pores, the fluctuations in X-ray absorption across the image are generally small. So long as the net attenuation itself is not too large we can approximate the exponential decay in X-ray intensity to first order terms:

$$I(x, y) = \frac{I'(x, y)}{I^m(x, y)} \approx 1 - \mu T(x, y), \quad (1)$$

where $I'(x, y)$ is the measured intensity, $I^m(x, y)$ is the incident intensity, μ is the material linear attenuation coefficient assuming a single homogenous material and $T(x, y)$ is the projected thickness of the particles / pores.

In phase contrast X-ray imaging, intensity is again well approximated as a linear function of particle thickness for sufficiently short propagation distances (refer to the treatment of the transport of intensity equation by Paganin *et al.* [18]). This approximation is particularly accurate when high spatial frequencies are attenuated, which can be a result of the limited spatial coherence of the beam, the point spread function of the detection system and/or image post processing.

In both cases, because the change in intensity can be treated as a linear function of the projected thickness, the intensity function for a distribution of particle sizes, in which the position of each particle is given by a randomly positioned delta function, can be expressed as a sum of convolutions:

$$I^m(x, y) = \sum_{r=R_{\min}}^{R_{\max}} \left\{ \sum_{n=1}^{N_r} [\delta(x-x_n)\delta(y-y_n)] * I^m_r(x, y) \right\}, \quad (2)$$

where I^m denotes that the image mean has been subtracted. Here we assume spherical particles of radius r , but note that the theory is valid for particles of any shape if their orientation are either identical or completely random (see [19]). We define the minimum and maximum radii as R_{\min} and R_{\max} , respectively. Here N_r is the number of particles of a particular radius.

The power spectrum of this image is given by:

$$\text{PSD}\{I^m(x, y)\} = \left| \sum_{r=R_{\min}}^{R_{\max}} \left\{ \sum_{n=1}^{N_r} \mathcal{F}\{\delta(x-x_n)\delta(y-y_n)\} \cdot \mathcal{F}\{I^m_r(x, y)\} \right\} \right|^2 \quad (3)$$

where \mathcal{F} denotes a Fourier transform. By application of the Wiener–Khinchin theorem, the autocorrelation function can be expressed as:

$$\text{SAF}\{I^m(x, y)\} = \mathcal{F}^{-1} \left\{ \left[\sum_{r=R_{\min}}^{R_{\max}} \left[\sum_{n=1}^{N_r} \mathcal{F}\{\delta(x-x_n)\delta(y-y_n)\} \cdot \mathcal{F}\{I^m_r(x, y)\} \right] \right]^2 \right\}. \quad (4)$$

Theoretically, the positions of particles in a suspension of non-penetrating particles cannot be truly random. However, for low volume fractions of particles, the positions of particles are only weakly correlated and the autocorrelation function can be approximated by the sum of the autocorrelation function of each particle:

$$\text{SAF}\{I^m(x, y)\} = \sum_{r=R_{\min}}^{R_{\max}} \mathcal{F}^{-1} \left\{ \sum_{n=1}^{N_r} |\mathcal{F}\{\delta(x-x_n)\delta(y-y_n)\}|^2 \cdot |\mathcal{F}\{I_r^m(x, y)\}|^2 \right\}. \quad (5)$$

Since the expected power spectrum of N_r randomly positioned delta functions can be shown to be N_r , if the mean intensity is removed [19]:

$$\text{SAF}\{I^m(x, y)\} = \sum_{r=R_{\min}}^{R_{\max}} N_r \text{SAF}\{I_r^m(x, y)\}. \quad (6)$$

For a distribution of particle sizes, if the SAF of all potential particle sizes is known, Eq. (6) is a linear inverse problem and the distribution, N_r , can be determined numerically.

3. Simulations

Computer simulations were undertaken to validate this theory and to demonstrate the ability to perform particle sizing. Synthetic samples were generated consisting of non-penetrating spherical glass particles randomly suspended in rectangular volumes (10 mm thick) with a total volume fraction of 2%. The position of each particle was generated randomly: a position was accepted if the particle to be inserted did not collide with any particles already in the volume. If a collision did occur, a new position was generated until an unoccupied location was found. At a volume fraction of 2%, the number of collisions is small, implying that the particles' positions are only weakly correlated.

PCXI was simulated by reducing the volume to a projected thickness, calculating the transmitted wave function and propagating using the angular spectrum method [20]. The imaging source was a coherent monochromatic beam at 33 keV and the propagation distance between the sample and detector, z , was 50 cm (Fig. 1). The glass particles had a refractive index decrement, $\text{Re}(1-n)$, of 4.863×10^{-7} and an absorption coefficient of 127.36 m^{-1} [12]. The propagated intensity function was filtered with a Gaussian kernel to simulate the point spread function of the detector and binned to achieve an effective pixel size of $6 \mu\text{m}$. This low pass filtering also accounts for the limited spatial coherence of an actual synchrotron beam [21]. The image mean was subtracted before a two-dimensional spatial autocorrelation was performed. The SAF was averaged over multiple windows (128×128 pixels) and azimuthally averaged (Fig. 1).

For a simple mixture with an equal number of particles of two discrete diameters, the SAF should be an equally weighted sum of the SAFs of single spheres of each diameter, as is shown to be the case in Fig. 2.

To model a more realistic sample, a mixture was generated in which particle diameters were sampled from a log-normal distribution: a skewed distribution whose logarithm is normally distributed, which is commonly used for the characterization of particle sizes [22]. The mean and standard deviation of the diameter's logarithm were $\mu = 4.72$ and $\sigma = 0.231$, respectively. The SAF was averaged over 1000 windows and 50 calibration SAFs were generated covering the range of particle sizes in the sample, each generated from the image of a single sphere. Solving for the distribution of particle diameters, N_r in Eq. (6), is a linear inverse problem. A least squares solver with a non-negative constraint and a second order finite-difference regularizer to penalize non-smooth solutions was used. The calculated distribution of particle diameters is presented in Fig. 3. The solution is shifted slightly away from the skew, which is the result of smoothing applied by the regularization term and depends on the choice of the regularization parameter.

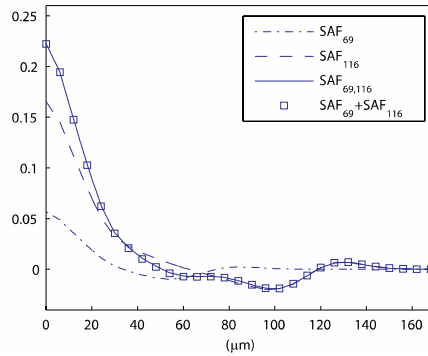


Fig. 2. The autocorrelation function produced by an equal mixture of two particle sizes is equal to the weighted sum of the autocorrelation functions of particles of each size. SAF_{69} and SAF_{116} are equally weighted autocorrelation functions of single particles with diameters of 69 μm and 116 μm respectively. $SAF_{69,116}$ is the autocorrelation of an equal mixture (by number) of particles. All SAFs in this figure were averaged over 256 windows.

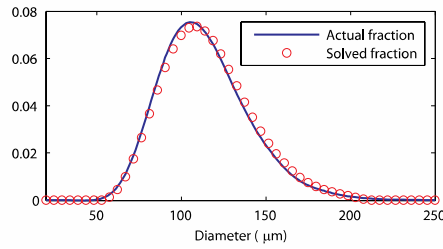


Fig. 3. Calculated distribution of particle diameters from simulated data. Each point represents the fraction of particles of that diameter.

4. Experimental results

A physical experiment, to further demonstrate the validity of the theory outlined here, was performed in experimental Hutch 3 of beamline 20B2 at the SPring-8 synchrotron in Japan [23]. The source-to-sample distance of ~ 210 m provided an incident wavefield of sufficient spatial coherence for propagation-based phase contrast imaging.

Because of the difficulty in obtaining particles for calibration purposes, a slightly different problem was tackled: to determine the ratio of mixtures of two particle sizes (where each nominal size is known to contain a distribution of diameters).

Nine mixtures of glass particles of two sizes (nominally 69 μm and 116 μm ; by Master sizer particle size analyzer log-normal distributions: $\mu = 4.26$, $\sigma = 0.227$ and $\mu = 4.72$, $\sigma = 0.231$) were prepared in cuvettes ($10 \times 10 \times 60$ mm³) by suspension in white petroleum jelly. The total volume fraction was again chosen to be 2%. Imaging was performed with a monochromatic beam at an energy of 33 keV, with a propagation distance of 50 cm between sample and detector. The detector's effective pixel size was 6 μm .

Based on Eq. (6), the SAF for these samples can be expressed in the form:

$$SAF\{i(x, y)\} = f SAF_{69} + (1 - f) SAF_{116} \quad (7)$$

where f is the volume fraction of the 69 μm particles and the calibration SAFs (SAF_{69} and SAF_{116}) are obtained from samples of unmixed particles. f can be determined by inversion of Eq. (7).

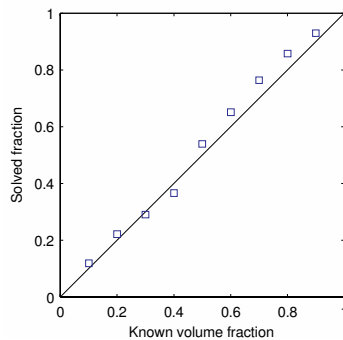


Fig. 4. Experimentally obtained volume fraction of one particle size from nine bimodal mixtures averaged over 460 windows. True solutions lie on the solid line.

The results for the fractions of each particle are presented in Fig. 4, and it can be seen that there is good agreement with the true values. Simulations of bimodal mixtures of particles with the same lognormal distributions used in the previous experiment were performed, and the results are presented in Fig. 5, which highlight the relationship between the error metric and the number of windows averaged over. The experimental error seen in Fig. 4 is more significant than that predicted by simulation. It is likely this discrepancy is largely due to inaccuracies in the preparation of the samples (e.g. uneven mixing).

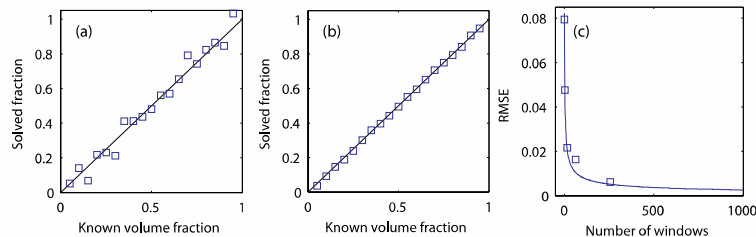


Fig. 5. Calculated volume fraction of one particle size in a mixture of two particles from simulated data; illustrating the reduction in error by averaging over 256 windows (b) versus 4 windows (a). Ideal solutions lie on the solid line. (c) Root mean square error as a function of the number of windows averaged over.

An apparent limitation evident in this experiment is the need for calibration samples. In principle it is possible to produce these samples, although a more practical approach would be to use simulated calibration samples in their place. However, the imaging system is complex and modeling it with the required accuracy is not trivial.

A theoretical limit on the maximum volume fraction for this method has already been touched on. Decreasing randomness at higher volume fractions corresponds to a breakdown of the assumption that the particles' positions are uncorrelated and the development of organization in their arrangement. This is analogous to the concept of the structure factor [24] in scattering techniques. Based on the SAF of synthetic samples, evidence of non-randomness

was observed for volume fractions greater than around 2-3%. However, in simulated experiments, comparable to those used to produce Fig. 5, increasing the volume fraction of particles only had a significant impact on the accuracy of solutions above 10%.

5. Conclusions

The methodologies discussed in this paper are expected to be useful for studying granular and particulate materials and systems with less radiation and higher temporal resolution than CT imaging, and at a scale beyond that where diffraction based X-ray scattering techniques have been demonstrated to be applicable.

Simulations suggest the upper limit of packing fractions for these methods is around 10%. As the packing fraction increases, the assumption of randomness of the position of the particles begins to break down as the sample starts developing a degree of organization. By using the extra information present in the SAF of such systems, it is conceivable that these methodologies could be extended to more densely packed systems.

Acknowledgments

The authors gratefully acknowledge support from Australian Research Council Grants (Grant Nos. DP110101941 and DP110101498). R.C. is a recipient of an Australian Postgraduate Award. We acknowledge useful discussions with D.M. Paganin in the preparation of this paper. We acknowledge travel funding provided by the International Synchrotron Access Program (ISAP) managed by the Australian Synchrotron.

3 Particle sizing II: Closely packed particles

In the previous chapter, a proof describing the formation of speckled projection images by volumes of grains or pores was presented. Additionally, it was shown that for a simple system of spherical particles not exceeding a packing fraction or porosity of around ten per cent, the distribution of the constituent particles could be found from the X-ray speckle image.

In this chapter we will consider random close-packing of systems of particles, like that produced by pouring microspheres into a container. Unlike the sparsely packed volumes considered in the previous chapter, this model is expected to be a closer approximation to alveolar packing. How accurately alveoli can be modelled by spheres is an open question. One way of considering the problem is that since the correlation function is produced by many alveoli, effectively what we're studying is the average shape of the alveoli. Assuming the orientation of the alveoli is isotropic, it's reasonable to expect the average alveoli will approximate a sphere. This model isn't perfect. In reality, the alveolar structure is closer to an irregular honeycomb in appearance than a cluster of spheres. Another concern is the impact of other structures, such as the airways, present in the lung but not in a volume of spheres. It is also necessary to contend with structures outside the lungs, such as bone and soft tissue. In chapter 4 specific techniques for performing bone segmentation and suppression are addressed. And in chapter 5 a method combining spatial frequency filtering and radial averaging of the autocorrelation functions is shown to minimise or eliminate contamination due to structures beyond the length scale of the alveoli.

Following the paper in section 3.1 describing a method for measuring the distribution of sizes of random close-packed volumes of particles, an additional validation study has also been included.

3.1 Article - Decoding the structure of granular and porous materials from speckled phase contrast X-ray images

The following paper was published in 2013 in *Optics Express*. This work was co-authored by M.J. Kitchen and A. Fouras. The paper is reproduced in this thesis directly from the published version.

Monash University

Declaration for Thesis Section 3.1

Declaration by candidate

In the case of Section 3.2, the nature and extent of my contribution to the work was the following:

Nature of contribution	Extent of contribution (%)
Initiated the paper, conducted experiments, performed analysis and wrote manuscript.	90

The following co-authors contributed to the work. If co-authors are students at Monash University, the extent of their contribution in percentage terms must be stated:

Name	Nature of contribution	Extent of contribution (%) for student co-authors only
M. J. Kitchen	Performed experiments, supported analysis and revised manuscript.	NA
A. Fouras	Performed experiments, supported analysis and revised manuscript.	NA

The undersigned hereby certify that the above declaration correctly reflects the nature and extent of the candidate's and co-authors' contributions to this work*.

Candidate's Signature		Date 11/12/2016
Main Supervisor's Signature		Date 11/12/2016

*Note: Where the responsible author is not the candidate's main supervisor, the main supervisor should consult with the responsible author to agree on the respective contributions of the authors.

Decoding the structure of granular and porous materials from speckled phase contrast X-ray images

R. P. Carnibella,^{1*} M. J. Kitchen,² and A. Fouras¹

¹Department of Mechanical Engineering, Monash University, Melbourne, 3800, Australia

²School of Physics, Monash University, Melbourne, 3800, Australia

*richard.carnibella@monash.edu

Abstract: Imaging techniques for studying the structure of opaque, granular and porous materials are limited by temporal resolution and radiation dose. We present a technique for characterising the structure of such materials by decoding three dimensional structural information from single, propagation based phase contrast X-ray images. We demonstrate the technique by measuring the distribution of diameters of glass microspheres in packed samples. We also present synthetic data, which shows that our inverse method is stable and that accuracy is improved by phase contrast X-ray imaging. Compared to computed tomography, our technique has superior temporal resolution and lower radiation dose.

©2013 Optical Society of America

OCIS codes: (100.2960) Image analysis; (110.7440) X-ray imaging; (120.5050) Phase measurement; (350.4990) Particles.

References and links

1. D. P. Schmidt and M. L. Corradini, "The internal flow of diesel fuel injector nozzles: A review," *Int. J. Engine Res.* **2**(1), 1–22 (2001).
2. F. J. Leij, T. A. Ghezzehei, and D. Or, "Modeling the dynamics of the soil pore-size distribution," *Soil Tillage Res.* **64**(1–2), 61–78 (2002).
3. D. E. Carney, C. E. Bredenberg, H. J. Schiller, A. L. Picone, U. G. McCann II, L. A. Gatto, G. Bailey, M. Fillinger, and G. F. Nieman, "The mechanism of lung volume change during mechanical ventilation," *Am. J. Resp. Crit. Care* **160**(5), 1697–1702 (1999).
4. A. J. Hajari, D. A. Yablonskiy, A. L. Sukstanskii, J. D. Quirk, M. S. Conradi, and J. C. Woods, "Morphometric changes in the human pulmonary acinus during inflation," *J. Appl. Physiol.* **112**(6), 937–943 (2012).
5. R. R. Mercer, M. L. Russell, and J. D. Crapo, "Alveolar septal structure in different species," *J. Appl. Physiol.* **77**(3), 1060–1066 (1994).
6. J. Knust, M. Ochs, H. J. G. Gundersen, and J. R. Nyengaard, "Stereological estimates of alveolar number and size and capillary length and surface area in mice lungs," *Anat. Rec. (Hoboken)* **292**(1), 113–122 (2009).
7. A. Fouras, B. J. Allison, M. J. Kitchen, S. Dubsky, J. Nguyen, K. Hourigan, K. K. W. Siu, R. A. Lewis, M. J. Wallace, and S. B. Hooper, "Altered lung motion is a sensitive indicator of regional lung disease," *Ann. Biomed. Eng.* **40**(5), 1160–1169 (2012).
8. C. N. Davies, *Aerosol Science* (Academic Press, 1966).
9. C. E. Mandt, Y. Kuga, L. Tsang, and A. Ishimaru, "Microwave propagation and scattering in a dense distribution of non-tenuous spheres: experiment and theory," *Waves Random Media* **2**(3), 225–234 (1992).
10. J. R. Fletcher, G. P. Swift, D. C. Dai, J. A. Levitt, and J. M. Chamberlain, "Propagation of terahertz radiation through random structures: An alternative theoretical approach and experimental validation," *J. Appl. Phys.* **101**(1), 013102 (2007).
11. C. M. Sayers and R. L. Smith, "The propagation of ultrasound in porous media," *Ultrasonics* **20**(5), 201–205 (1982).
12. The ImPACT Group, *Comparative Specifications: 128 to 320 Slice CT Scanner Technical Specifications* (Centre for Evidence-based Purchasing, 2009).
13. R. Mokso, P. Cloetens, E. Maire, W. Ludwig, and J.-Y. Buffière, "Nanoscale zoom tomography with hard x rays using Kirkpatrick-Baez optics," *Appl. Phys. Lett.* **90**(14), 144104 (2007).
14. M. Langer, A. Pacureanu, H. Suhonen, Q. Grimal, P. Cloetens, and F. Peyrin, "X-ray phase nanotomography resolves the 3D human bone ultrastructure," *PLoS ONE* **7**(8), e35691 (2012).

15. R. Mokso, F. Marone, D. Haberthür, J. C. Schittny, G. Mikuljan, A. Isenegger, and M. Stampanoni, "Following dynamic processes by X-ray tomographic microscopy with sub-second temporal resolution," in *AIP Conference Proceedings* (2011), Vol. 1365, pp. 38–41.
16. J. Moosmann, A. Ershov, V. Altapova, T. Baumbach, M. S. Prasad, C. LaBonne, X. Xiao, J. Kashef, and R. Hofmann, "X-ray phase-contrast in vivo microtomography probes new aspects of *Xenopus* gastrulation," *Nature* **497**(7449), 374–377 (2013).
17. S. Fain, M. L. Schiebler, D. G. McCormack, and G. Parraga, "Imaging of lung function using hyperpolarized helium-3 magnetic resonance imaging: Review of current and emerging translational methods and applications," *J. Magn. Reson. Imaging* **32**(6), 1398–1408 (2010).
18. O. Glatter and O. Kratky, *Small Angle X-ray Scattering* (Academic Press, 1982).
19. U. Bonse and M. Hart, "Small angle X-ray scattering by spherical particles of polystyrene and polyvinyltoluene," *Z. Phys.* **189**(2), 151–162 (1966).
20. R. Cerbino, L. Peverini, M. A. C. Potenza, A. Robert, P. Bosecke, and M. Giglio, "X-ray-scattering information obtained from near-field speckle," *Nat. Phys.* **4**(3), 238–243 (2008).
21. R. P. Carnibella, M. J. Kitchen, and A. Fouras, "Determining particle size distributions from a single projection image," *Opt. Express* **20**(14), 15962–15968 (2012).
22. J. H. Holland, *Adaptation in Natural and Artificial Systems: An Introductory Analysis with Applications to Biology, Control, and Artificial Intelligence* (MIT Press, 1992).
23. L. Randy, Haupt, *Practical Genetic Algorithms*, 2nd ed. (Wiley Interscience, 2004).
24. A. Snigirev, I. Snigireva, V. Kohn, S. Kuznetsov, and I. Schelokov, "On the possibilities of x-ray phase contrast microimaging by coherent high-energy synchrotron radiation," *Rev. Sci. Instrum.* **66**(12), 5486–5492 (1995).
25. S. W. Wilkins, T. E. Gureyev, D. Gao, A. Pogany, and A. W. Stevenson, "Phase-contrast imaging using polychromatic hard X-rays," *Nature* **384**(6607), 335–338 (1996).
26. M. J. Kitchen, D. Paganin, R. A. Lewis, N. Yagi, K. Uesugi, and S. T. Mudie, "On the origin of speckle in x-ray phase contrast images of lung tissue," *Phys. Med. Biol.* **49**(18), 4335–4348 (2004).
27. S. Torquato, T. M. Truskett, and P. G. Debenedetti, "Is random close packing of spheres well defined?" *Phys. Rev. Lett.* **84**(10), 2064–2067 (2000).
28. S. B. Yuste and A. Santos, "Radial distribution function for hard spheres," *Phys. Rev. A* **43**(10), 5418–5423 (1991).
29. C. James, Spall, "Stochastic optimization," in *Handbook of Computational Statistics: Concepts and Methods*, Wolfgang Härdle, James E. Gentle, and Yuichi Mori, eds. (Springer, 2004), pp. 169–197.
30. V. Alan, Oppenheim, *Discrete-time Signal Processing*, 2nd ed. (Prentice Hall, 1999).
31. A. W. Klein, R. F. Becker, and M. R. Bryson, "A method for estimating the distribution of alveolar sizes from histological lung sections," *Trans. Am. Microsc. Soc.* **91**(2), 195–208 (1972).
32. L. Knudsen, E. R. Weibel, H. J. G. Gundersen, F. V. Weinstein, and M. Ochs, "Assessment of air space size characteristics by intercept (chord) measurement: an accurate and efficient stereological approach," *J. Appl. Physiol.* **108**(2), 412–421 (2010).
33. C. Kloss, C. Goniva, A. Hager, S. Amberger, and S. Pirker, "Models, algorithms and validation for opensource DEM and CFD-DEM," *Prog. Comput. Fluid Dy.* **12**, 140–152 (2012).
34. A. Pogany, D. Gao, and S. W. Wilkins, "Contrast and resolution in imaging with a microfocus x-ray source," *Rev. Sci. Instrum.* **68**(7), 2774–2782 (1997).
35. M. Nieto-Vesperinas, *Scattering And Diffraction in Physical Optics*, 2nd ed. (World Scientific, 2006).
36. L. Eshelman and J. Schaffer, "Real-coded genetic algorithms and interval-schemata," in *Foundations of Genetic Algorithms*, D. Whitley, ed. (Morgan Kaufmann, 1993), pp. 187–202.
37. S. Goto, K. Takeshita, Y. Suzuki, H. Ohashi, Y. Asano, H. Kimura, T. Matsushita, N. Yagi, M. Isshiki, H. Yamazaki, Y. Yoneda, K. Umetani, and T. Ishikawa, "Construction and commissioning of a 215-m-long beamline at SPring-8," *Nucl. Instrum. Meth. A* **467–468**, 682–685 (2001).
38. M. J. Berger, J. H. Hubbell, S. M. Seltzer, J. Chang, J. S. Coursey, R. Sukumar, D. S. Zucker, and K. Olsen, "XCOM: Photon Cross Sections Database," <http://www.nist.gov/pml/data/xcom.index.cfm>.
39. M. J. Kitchen, R. A. Lewis, M. J. Morgan, M. J. Wallace, M. L. Siew, K. K. W. Siu, A. Habib, A. Fouras, N. Yagi, K. Uesugi, and S. B. Hooper, "Dynamic measures of regional lung air volume using phase contrast x-ray imaging," *Phys. Med. Biol.* **53**(21), 6065–6077 (2008).
40. R. A. Jamison, J. A. Armitage, J. Carberry, M. J. Kitchen, S. B. Hooper, and A. Fouras, "Functional imaging to understand biomechanics: a critical tool for the study of biology, pathology and the development of pharmacological solutions," *Curr. Pharm. Biotechnol.* **13**(11), 2128–2140 (2012).
41. J. Thurgood, S. Hooper, M. Siew, M. Wallace, S. Dubsy, M. Kitchen, R. A. Jamison, R. Carnibella, and A. Fouras, "Functional lung imaging during HFV in preterm rabbits," *PLoS ONE* **7**(10), e48122 (2012).

1. Introduction

The study of granular and porous materials is relevant across a range of disciplines including material science, mechanical and chemical engineering, geophysics and biology. The development of cavitation bubbles in diesel injectors [1], the change in soil pore size during

wetting and drying [2] and the mechanics of alveoli in the breathing lung [3] are examples of dynamic systems, which existing imaging techniques are not well suited to studying.

Expanding briefly on the example of the lung, despite much research, respiratory physiologists' understanding of alveolar mechanics during respiration remains incomplete. The degree to which alveolar expansion and recruitment each contribute to inflation continues to be a topic of debate [3,4]. Dynamic imaging of lung alveoli is a particularly difficult problem because of their small size compared to that of the entire lung and the velocity at which they move. A free breathing mouse, for example, has millions of alveoli, each of the order of 100 μm in diameter [5,6], packed inside a chest several centimetres wide, which respire 3-4 times a second. In addition to physiological studies, there is potential for disease detection applications using dynamic lung imaging techniques [7].

To non-destructively study the kinds of samples described, optical and other low energy imaging modalities, from visible light to terahertz frequencies [8–10], suffer from scattering and limited penetration depth. Ultrasound imaging has similar drawbacks [11].

X-ray computed tomography (CT) is a powerful and widely used technique for visualizing the three-dimensional structure of a sample. Despite not being inherently suited to studying dynamic systems because of the requirement for multiple projections at any time point, modern scanners are still capable of quite respectable temporal resolution. Third generation clinical CT scanners are capable of scanning at around 3-4 frames per second with sufficient spatial resolution to differentiate structures down to about half a millimetre in size [12]. However, this is still slower than many dynamic processes and the spatial resolution is too coarse for micro-imaging. Micro-tomography and even nano-tomography [13,14] are possible using an ultra-bright synchrotron source. A state of the art micro-tomography scanner, with an ultra-bright synchrotron radiation source, has been demonstrated capable of scanning an infant rat's chest in half a second [15]. Another interesting example is 4D tomography of *Xenopus* gastrulation [16]. However, these scanners are incapable of the frame rates required to dynamically image rapidly moving systems such as breathing lungs. In addition to temporal resolution, a significant problem with CT is the high radiation dose, which is particularly relevant for biological samples.

In lung imaging, hyperpolarized helium diffusion MRI has recently been used to try and measure alveolar dynamics [4]. There are a number of problems with this method, which include the difficulty and expense of obtaining hyperpolarized helium, the fact that diffusion is a relative measurement, and that airspace dimensions can only indirectly be obtained from these diffusion measurements [17].

At submicron scales, X-ray scattering techniques can be used to obtain structural information from single projection images [18–20]. Since scattering angles are inversely proportional to the size of the scattering particles, the problem of measuring increasingly smaller scattering angles limits the maximum feature size which can be studied.

For studying particles tens to hundreds of microns in size, Carnibella *et al.* [21] presented a method for determining basic morphological parameters of randomly packed particles at low packing fractions from a single projection X-ray image. This method was based on the encoding of three-dimensional structural information in speckled two-dimensional X-ray images of the samples. Specifically, this method exploited the linearity of the spatial autocorrelation function (SAF) of these images. For densely packed systems of particles, the positions of individual particles are more strongly correlated and the SAFs are no longer linear. Therefore, a non-linear inverse method is necessary to decode their structure. In this paper, we present a technique using a genetic algorithm [22,23] (GA) to recover morphological parameters of randomly packed particles, without restriction on the packing fraction.

We begin by describing the theoretical and technical background of the technique. We demonstrate, experimentally, its application in determining the distribution of diameters in a packed sample of glass microspheres. Finally, we use synthetic X-ray images of microspheres

to characterise the performance of our GA and the efficacy of propagation based phase contrast.

2. Description of technique

When a sample of randomly packed particles is imaged using absorption or phase contrast X-ray imaging [24,25] (PCXI), the resulting image has a speckled appearance [26]. Examples of these images can be found in Figs. 1 and 3. We make note that this speckle is not necessarily so called near field speckle [20] and that, in fact, it is also produced in absorption based imaging. Speckle contrast, however, is markedly improved in PCXI. Carnibella *et al.* [21] showed that at low packing fractions, the SAF of a projection image of a sample is equal to the sum of the SAF of the image of each particle in that sample. This implies that the speckled images contain information about the morphology of the particles, since the SAF of the image of a single particle is directly related to its morphology. In the same paper, it was also found that at higher packing fractions this behaviour began to break down, which corresponded with the development of oscillations in the previously single peaked SAFs. It was hypothesised that these oscillations were related to both the shape (form) and organisation (structure) of the particles and that it should be possible to recover details of these properties.

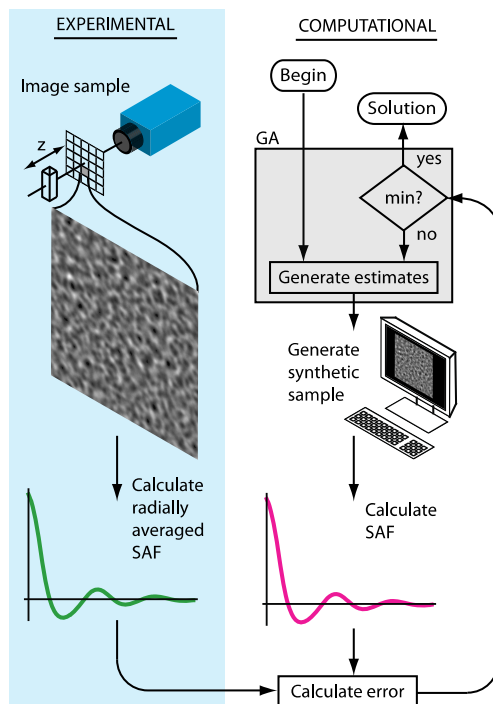


Fig. 1. An overview of the complete process of solving for particle statistics. On the left, a single phase contrast image of the sample is taken at a propagation distance, z , and its spatial autocorrelation function (SAF) calculated. On the right the genetic algorithm (GA) iterates over simulated particle SAFs to find the particle parameters that produce the closest match between the two SAFs.

Ideally, we seek an analytical expression for the SAF as a function of some parameters related to the morphology and/or structure of the particles. Then, an appropriate optimisation method could be applied to solve for these parameters. To our knowledge, no such analytical expression exists describing the distribution of particles in samples approaching random close packing [27]. We note that for lower packing densities (suspensions), the Percus-Yevick approximation can be used to obtain the radial distribution function analytically [28], and that this could potentially be used as the basis of an inverse method.

Our method is based on stochastic modelling of particle packing, combined with physical modelling of the imaging process, using an iterative approach to solve the forward imaging problem until simulated results match experimental data. The particles are selected randomly from a distribution described by some parameters, and a GA attempts to find the set of these parameters that produces the best match between simulated and experimental SAFs. A simple outline of this procedure can be found in Fig. 1. GAs are particularly suited to this task because they tend to locate global minima and are robust in the presence of variability related to the stochastic nature of the simulations [29].

The experimental SAF is easily obtained after imaging a sample. Propagation based phase contrast X-ray images can be obtained by imaging with a coherent X-ray source such as a synchrotron or micro-focus lab source. The images are pre-processed by applying flat and dark field corrections:

$$I = \frac{I_{\text{raw}} - I_{\text{dark}}}{I_{\text{flat}} - I_{\text{dark}}}. \quad (1)$$

The SAF is obtained by dividing the image into N smaller windows, averaging their normalised 2D SAFs, and radially averaging:

$$\text{SAF}_{2\text{D}}(j, k) = \sum_{x,y} I_{x,y} I_{x-j, y-k}, \quad (2)$$

$$\overline{\text{SAF}}_{2\text{D}}(j, k) = \frac{1}{N} \sum_{n=1}^N \frac{\text{SAF}_{2\text{D},n}(j, k)}{\text{SAF}_{2\text{D},n}(0, 0)}, \quad (3)$$

$$\text{SAF}(l) = \frac{1}{M} \sum_{m=1}^M \overline{\text{SAF}}_{2\text{D}} \Big|_{|l-0.5 \leq \sqrt{j^2+k^2} < l+0.5} (j, k), \quad (4)$$

where M is the number of pixels that have a centre within a circular band defined by the radii: $l-0.5$ and $l+0.5$. Ideally, the window size should be such that it can capture the full SAF. The point at which the SAF settles near zero depends on the size of the particles. We found choosing a window size that captures at least the first three peaks of the SAF to be sufficient. Windowing is necessary because a single autocorrelation is not a consistent estimator of the true SAF: that is, the variance of the autocorrelation function does not decay to zero as the window size is increased [30].

We now outline the process of obtaining a simulated SAF, produced by a given set of parameter estimates. In the context of a GA, a set of parameter estimates is referred to as a chromosome. The simulation process begins with a description of the distribution of particle diameters. We use a volume weighted, lognormal probability density function (PDF), which can be characterised by two parameters: its geometric mean (GM) and geometric standard deviation (GSD). Many collections of particles including alveoli are well approximated by a lognormal distribution [31,32], however, any other PDF could be similarly used. The pouring of particles is simulated using molecular dynamics software (LIGGGHTS [33]). We assume the particles are spherical and non-penetrating. The mean packing fraction achieved was 60.0 per cent.

Next, we simulate X-ray images of these particles. We consider the case of propagation based PCXI, the modality used in the experiments presented later. Following the method outlined by Kitchen *et al.* [26], the sample volume is first reduced to two dimensions by making a projection approximation [34]. Then, assuming a plane wave source, the exit wave field is calculated:

$$U_{\text{exit}} = e^{-\mu} e^{-ik\delta t}, \quad (5)$$

where μ is the linear attenuation coefficient, δ is the refractive index decrement and t is the projected thickness of the sample. This wave field is then propagated a distance, z , to the plane of the detector using the angular spectrum method [35]. The intensity function of this wave field is convolved with a Gaussian kernel, described by a single parameter: its standard deviation, σ_{blur} , which accounts for the combined effects of partial coherence, the point spread function of the detector and penumbral blurring:

$$I_{\text{sim}} = |U_{\text{propagated}}|^2 * N(0, \sigma_{\text{blur}}), \quad (6)$$

where $N(\mu, \sigma)$ is a normal distribution with mean, μ and standard deviation, σ . This last operation is simply the application of a Gaussian low pass spatial filter. The resulting image is binned to match the effective pixel size of the actual detector. The normalised two dimensional SAFs of smaller sample windows within the image are calculated. The SAF of multiple windows are averaged and that result radially averaged to produce the final simulated SAF.

The GA requires an initial randomly generated population of N_{pop} chromosomes. Each chromosome consists of the following parameters: the GM and the GSD of the distribution of particle diameters and the standard deviation of the Gaussian low pass filter kernel. Before running the algorithm it is necessary to set upper and lower limits for each parameter. Choosing limits which bracket smaller ranges will decrease convergence time. However, care must be taken to ensure that the range of each parameter encompasses the true, but unknown value. The cost of each chromosome is determined by calculating the sum of squared errors between the experimental SAF and a simulated SAF generated from each chromosome's parameters.

The $N_{\text{pop}}/2$ chromosomes with the highest costs are discarded. Pairs of chromosomes are randomly selected, from a rank weighted population [23], to be parents. Uniform crossover using the BLX-0.5 operator [36] is performed to produce two offspring from each pair of parents. At the end of this process the population size remains unchanged. Mutations, according to a Gaussian distribution (standard deviation, σ_{mutation}) are randomly applied to a fraction, f_{mutation} , of the parameters from any chromosomes other than that with the lowest cost (elitism):

$$x_{\text{mutated}}(x) = \min(\max(N(x, \sigma_{\text{mutation}}), x_{\text{lo}}), x_{\text{hi}}), \quad (7)$$

where x is the value of the parameter being mutated, N is a normal distribution and x_{lo} and x_{hi} are the lower and upper limits of that parameter.

This process is repeated until the cost function shows no signs of improvement, at which point we assume the algorithm has reached the vicinity of the global minimum. Mutations are then disabled and the algorithm is allowed to continue until all the parameters have converged. The specific stopping criteria used in the following sections are described in each section.

3. Application to experiments

To test our technique, we conducted experiments on beamline BL20B2 at the Spring-8 synchrotron, Japan [37]. A detuned Si(111) double crystal monochromator was used to

generate a monochromatic beam, with an energy of 34 keV to image solid glass microspheres. The sieved microspheres were nominally of 4 different ranges of diameters (63-75 μm , 75-90 μm , 90-106 μm , 106-125 μm). Plastic cuvettes ($10 \times 50 \times 10 \text{ mm}^3$) filled with these microspheres were placed at a propagation distance of 0.5 m from the detector. The detector was a Hamamatsu C4880-41S, with an effective pixel size of 5.9 μm . Exposure times were 2 seconds. The SAF was averaged over approximately 200 windows (96×96 pixels, $1132.8 \times 1132.8 \mu\text{m}^2$).

To simulate SAFs for the GA, the sample volume had the imaging area of a single experimental window and was 1 mm deep ($1132.8 \times 1132.8 \times 1000 \mu\text{m}^3$). Spheres were modelled as soda lime glass, which when imaged at 34 keV have a linear absorption coefficient of 198.0 m^{-1} and a refractive index decrement of 4.67×10^{-7} [38]. The SAF was averaged over 16 windows (chosen as an acceptable balance between accuracy and computational effort). Other relevant parameters were the same as for the experimental setup.

The GA was run with a population size of 12 and with the following limits on each parameter's range: 20 μm to 120 μm for the GM, 1.01 to 1.3 for the GSD and 6 μm to 30 μm for the standard deviation of the Gaussian kernel. These limits were chosen to encompass all reasonable solutions, given we had prior information on the microspheres' diameters. The mutation distribution, σ_{mutation} , was 0.2 of each parameter range and f_{mutation} was 0.2. The GA was deemed to have reached the global minimum when the mean slope of the cost function for the last 10 iterations was equal to or greater than zero. With mutations disabled, the algorithm was allowed to continue until the difference between parameters across the population was less than 1 per cent. At this point the chromosome with the lowest cost was chosen as the solution.

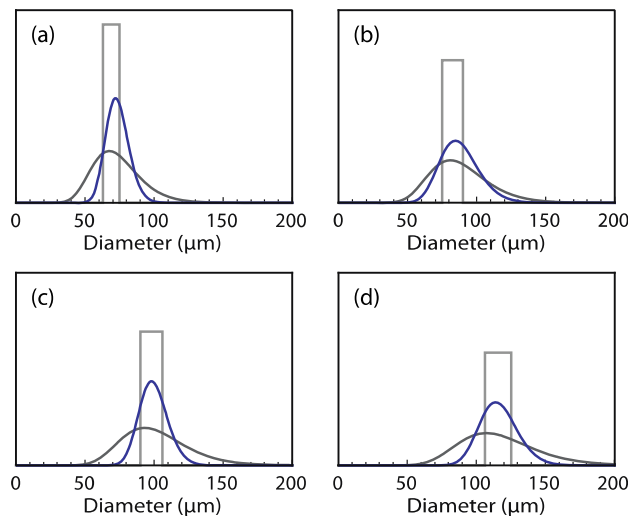


Fig. 2. The distributions of microsphere sizes obtained from experimental images. Nominal sieve sizes were (a) 63-75 μm , (b) 75-90 μm , (c) 90-106 μm and (d) 106-125 μm . These sizes are depicted by the light grey top hat functions. The darker grey curve is the distribution measured by a commercial particle sizer (Mastersizer 2000). The darkest/blue curve is the distribution measured by our method.

Table 1. Comparison of nominal microsphere sizes with geometric mean, geometric standard deviation and interquartile range (IQR) measured by a commercial particle size analyzer and phase contrast X-ray speckle analysis

Nominal Range (μm)	GM (μm)		GSD		IQR (μm)	
	Mastersizer	Speckle	Mastersizer	Speckle	Mastersizer	Speckle
63-75	71.4	73.0	1.27	1.12	60.9-83.8	67.7-78.8
75-90	85.8	86.8	1.27	1.17	72.9-101.0	77.9-96.7
90-106	98.6	99.2	1.27	1.11	84.0-115.7	92.5-106.3
106-116	113.4	115.3	1.27	1.13	96.4-133.4	106.5-124.9

Computational effort is almost solely attributable to the simulation of pouring spheres. Running on a single 3 GHz processor core, for the window size described, the pouring simulations took on average around 5 minutes. For a population size of 12, when averaging over 16 windows, this means 192 pouring simulations per iteration of the GA. Fortunately, since every simulation window is completely independent, if enough cores are available, an entire iteration could be completed in a few minutes. Typically, less than 40 iterations were required for the GA to converge.

Our results are displayed in Fig. 2 and quantified in Table 1. As can be seen, the mean microsphere diameters agree well with both the nominal particle sizes and those obtained by a commercial measurement system (Mastersizer 2000). Interestingly, the spread of diameters is less than that measured by the commercial system, and more closely agrees with the nominal sieve limits.

Two second exposure times were used to obtain a high signal to noise ratio for testing this technique on a strongly attenuating sample and does not represent the best temporal resolution of the technique. For example, at this beamline much shorter exposure times (tens of milliseconds) are possible within the lungs [7,39,40], with frame rates as high as three hundred frames per second even achievable [41]. In comparison to the technique presented here, a high resolution CT scan may require of the order of 1000 projections. Hence we could obtain the same morphological information at 1000 times the frame rate and with 1/1000 the radiation dose of CT.

4. Synthetic studies

To characterise the performance of our solver and study the efficacy of X-ray phase contrast for sizing particles, we applied the technique to measure the distribution of sphere diameters from synthetically generated X-ray images. The synthetic images were generated using the same method as previously described. The distribution of sphere diameters had a GM of 56.7 μm and a GSD of 1.14. These parameters are those of the largest sieved microspheres (106-125 μm), which we had previously measured (Fig. 2). The width of the Gaussian kernel was also obtained from the previous experiment, having imaged samples at a number of propagation distances. Photon and readout noise were added according to the camera's specifications and assuming photon counts similar to those recorded experimentally. The synthetic images were scaled to match the mean intensity and contrast of the 10 mm deep samples we measured experimentally (in our simulations other speckle characteristics were independent of sample depth). Synthetic images were generated at propagation distances between zero and three metres. Figure 3 shows that, to the eye, these synthetic speckle images closely match the corresponding experimental images. Synthetic experimental SAFs were produced by averaging 400 windows and radially averaging.

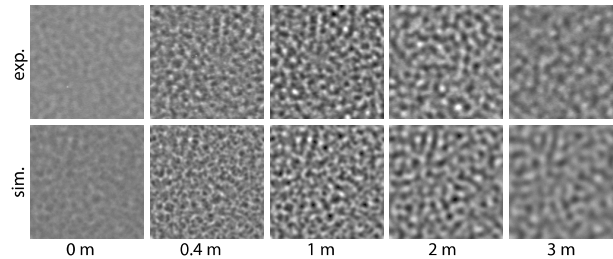


Fig. 3. The upper row is a series of experimental phase contrast X-ray images, of nominally 106-125 μm glass microspheres, recorded at propagation distances of 0.01 m, 0.4 m, 1 m, 2 m and 3 m. For comparison, the lower row shows simulated images at the same propagation distances. The latter is based on solutions for the distribution of sphere sizes in the experimental images. Each image is $1132.8 \times 1132.8 \mu\text{m}^2$.

The GA was run with the following limits on each parameter's range: 48 μm to 68 μm for the GM, 1.05 to 1.2 for the GSD and 6 μm to 35 μm for the standard deviation of the Gaussian kernel. To produce an estimate of uncertainty in the solution, upon convergence the algorithm was restarted (by keeping the best and randomly generating 11 new chromosomes) and run until the variables converged again. In this way the solver was allowed to converge a total of 10 times, which produced 10 solutions. In Figs. 4(a) and 4(b) the parameters belonging to each of these solutions is plotted.

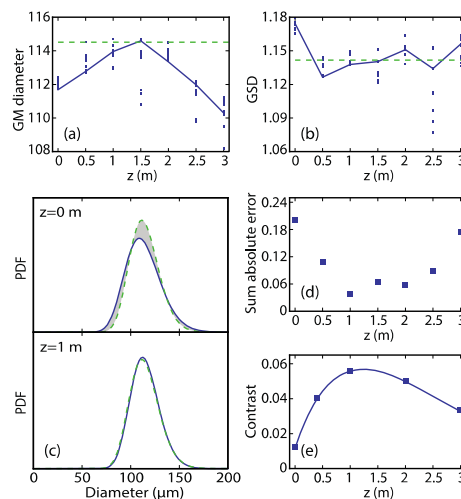


Fig. 4. (a) The geometric mean (GM) and (b) geometric standard deviation (GSD) of the distribution of microsphere diameters measured from synthetic phase contrast X-ray images at several propagation distances, z . In these two sub-figures, individual solutions are plotted as points, the parameters of the best solution are linked by a solid line, and the true solution is denoted by a horizontal dashed line. (c) The probability density functions (PDF) of microsphere diameters, measured at propagation distances of 0 m and 1 m. (d) The sum of absolute errors between the true and measured PDF at several propagation distances. The points at 0 m and 1 m correspond with the shaded area between the PDFs in (c). (e) Speckle contrast, measured as the standard deviation of image pixel intensities, as a function of propagation distance.

The spread of the GAs solutions (the points in 4(a) and (b)) at each propagation distance isn't obviously correlated with the propagation distance or image contrast (Fig. 4(e)). This is consistent with this variability being the result of the stochastic nature of the simulations. Therefore, we expect that this variance can be reduced by averaging the SAF over more windows, at the expense of increased computation time.

Overall, the best solutions are quite close to the true distributions of the microspheres' diameters. Comparing the extremes of these solutions (at $z = 0$ m and $z = 1$ m) in Fig. 4(c) highlights that even in the worst case ($z = 0$ m), the solution is still quite accurate: the GM and GSD are in error by 1.5% and 2.9%, respectively. In Fig. 4(d) it can be seen that accuracy is worst at very short propagation distances, where phase contrast is weak, and at the largest propagation distances, where the size of the Gaussian kernel is greatest (not shown). The inverse relationship between the solution error and the speckle contrast is illustrated by comparing Figs. 4(d) and 4(e). Since speckle contrast is proportional to the signal to noise ratio, this relationship is not surprising. We note that our experimental images were of static samples, with a high intensity synchrotron source and significant exposure times. We expect that the benefit afforded by phase contrast would be of greater significance when imaging conditions are less ideal.

We encountered an unexpected result in the behaviour of the Gaussian low pass filter kernel over the range of propagation distances. We found that this parameter increased almost linearly over the range of propagation distances, at a rate greater than expected by penumbral blurring for the known source size of $150\ \mu\text{m}$ (horizontal) by $10\ \mu\text{m}$ (vertical). As mentioned, this accounts for the decrease in contrast at the largest propagation distances. Our hypothesis is that this may be the result of scattering/refraction within the volume of the sample, which we assume is negligible when we make the projection approximation. Alternatively, or additionally, it may be the result of scattering by optical elements and/or air along the beam path which hasn't been accounted for in our model. These hypotheses warrant further investigation.

5. Conclusions

In this paper we have outlined a new technique for the quantification of useful parameters related to random granular and porous systems without restriction on the mode of packing. The basis of the technique lies in retrieving structural information encoded in speckled phase contrast X-ray images of such systems. The experimental and synthetic results presented demonstrate the accuracy and robustness of this technique and that propagation based phase contrast significantly improves the accuracy. We have also shown that there is a limit to the gains that can be obtained by increasing the propagation distance due to an increase in blurring. The advantages of our technique are high temporal resolution and low radiation dose, which suggest potential applications for imaging dynamic and biological systems. Specifically, we envisage the technique being applied to the measurement of dynamic lung morphology, for physiological studies or disease detection.

Acknowledgments

The authors gratefully acknowledge support from Australian Research Council Grants (Grant Nos. DP110101941 and DP110101498). R.C. is a recipient of an Australian Postgraduate Award. We acknowledge travel funding provided by the International Synchrotron Access Program (ISAP) managed by the Australian Synchrotron.

3.2 Additional particle sizing validation

At the time of submission of the preceding paper, the commercial particle sizer (Mastersizer 2000) had been deemed the gold standard measurement of the true distribution of particle sizes. While there is reasonable correspondence between X-ray speckle-based measurements and those made by the Mastersizer, and additionally between these and the nominal particle diameters, it was decided to investigate the discrepancies between each measurement technique further. The details of this investigation and its associated findings are presented here.

Microspheres from the same samples used in the paper were dusted onto an adhesive Kapton backing to produce a monolayer of particles. These monolayers were then imaged at high resolution on beamline 20XU at the SPring-8 synchrotron, Japan. Phase contrast enhanced imaging was performed with 1 m of propagation distance between the sample and detector, so that the spheres' edges were easily identifiable (Figure 3.1a). The true edge of the particle lies between the two strongest black and white phase contrast fringes. Images were taken with a PCO.edge scientific CMOS camera (sCMOS; 6.5 μm pixels) using a Hamamatsu beam monitor with a 10X objective lens installed. The resulting effective pixel size was measured as 0.56 μm . Enough images were taken to ensure sufficient sampling numbers (Table 3.1).

Table 3.1: Number of microspheres sampled for each nominal microsphere size.

Microsphere size (μm)	Number of spheres
63-75	694
75-90	715
90-106	275
106-125	543

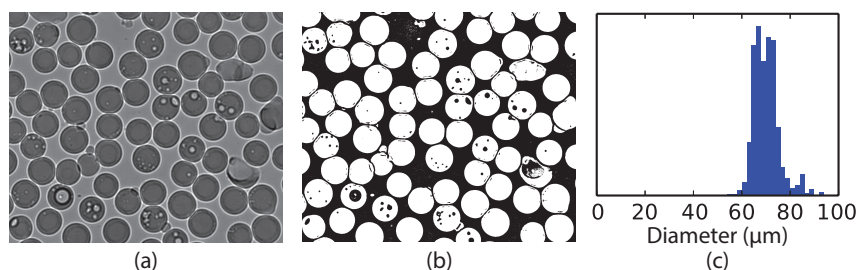


Figure 3.1: Flat and dark field corrected phase contrast images of microspheres (a) are first thresholded (b) before particle diameters are measured and binned to produce histograms (c) of the size distribution.

Each image was analysed using ImageJ image processing software. After flat and dark field correction, the image was thresholded (Figure 3.1b) and analysed using

the software's 'Analyze Particles' feature. Non-circular objects and objects deemed too small to be a microsphere were rejected. Again, the number of microspheres identified for each sample size can be found in Table 3.1. Finally histograms of the measured particle diameters were produced using 2 μm wide bins (Figure 3.1c). We will refer to this method from here on in as monolayer-based measurement.

In Figure 3.2 we compare these histograms with the nominal distributions and the distributions measured by the Mastersize and the X-ray speckle analysis method. To quantify these comparisons, the mean square error between the monolayer-based histograms (reference) and each of the other measurements for each nominal distribution was also calculated (Figure 3.3).

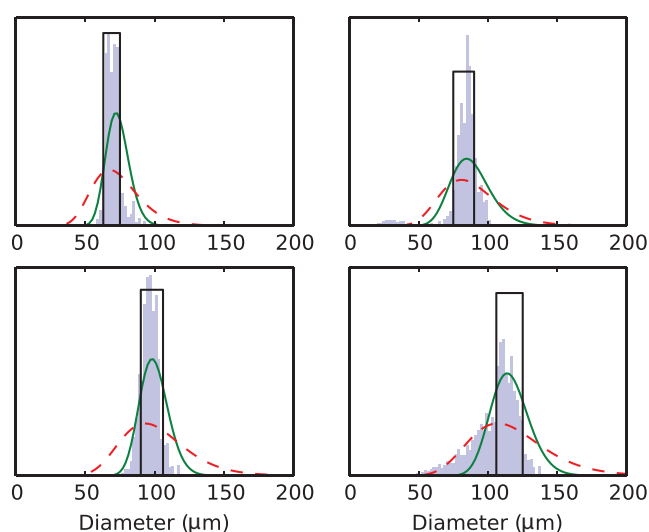


Figure 3.2: The nominal (black top-hat), Mastersizer (red dashed), X-ray speckle (green) and monolayer-based (blue-grey histogram) measured distributions (probability density functions) for each batch of microspheres. Working clockwise from top-left, nominal microsphere sizes in micrometres are 63-75 (69), 75-90 (83), 90-106 (98) and 106-125 (116). Values in brackets are the midpoint of each range.

If the monolayer-based measurements are accepted as new gold standard, these results indicate that the X-ray speckle-based technique has outperformed the commercial particle sizer in all cases, based on the mean square error. When the shape of the true distribution is closer to a uniform distribution than a lognormal distribution (the nominally 69 and 83 μm microspheres), the nominal distribution proves to be the best description of microsphere size. Potentially a less restrictive choice of distribution could improve the performance of the technique. Nevertheless, it has proven itself superior for more natural (Gaussian-like) distributions and in all cases has been shown to measure particle distributions with greater accuracy than the commercial particle sizer.

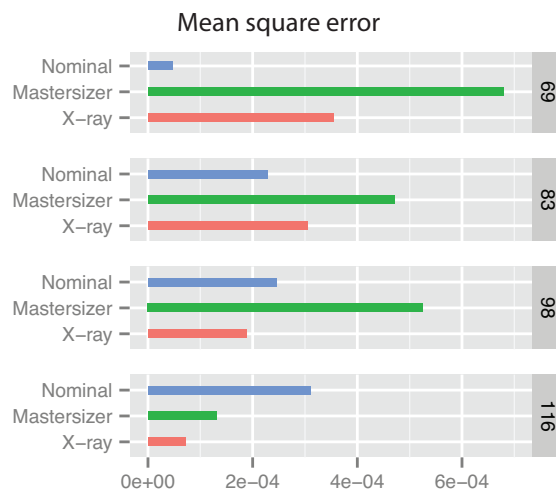


Figure 3.3: Quantitive comparison (mean square error) of distributions measured by various techniques relative to monolayer-based measurement.

4 Bone segmentation and suppression

There are two significant differences between a chest X-ray containing the lungs and an X-ray image of a volume of microspheres. The first, which was addressed in chapter 3, concerns the validity of the approximation of the lungs and specifically the alveoli as a volume of packed spheres. The second, which is the topic of this chapter, is that a chest X-ray also contains the shadows of other structures that are outside of the lungs. Some of these shadows are produced by soft tissues such as the heart, the muscles of the chest wall and the skin. These materials have similar X-ray properties to water (being largely composed of water themselves) and tend to produce large shadows with gentle gradients that can be effectively removed using a spatial frequency filter.

More problematic than the soft tissue shadows are those of the bones of the ribcage and spine. The significantly higher X-ray attenuation of bone, due to its high calcium content, results in bony structures featuring prominently on a chest X-ray and partially obscuring the view of the lung fields. The autocorrelation function of lung speckle is significantly distorted by contamination with signal from bone (Figure 4.1), which is a problem when we seek to use the autocorrelation function to measure alveolar size. To date there have been many approaches developed for the purpose of subtracting the shadows of bones from chest X-ray images. A selection of these are outlined in the published paper in section 4.1.

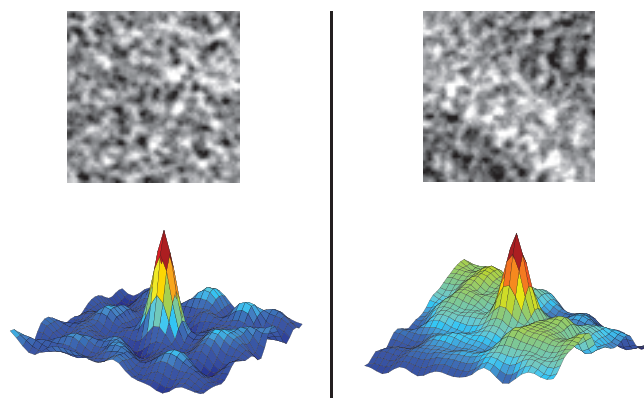


Figure 4.1: X-ray lung speckle and corresponding spatial autocorrelation function (left) beside another image of lung speckle showing the autocorrelation function affected by an overlying rib (right). In addition to producing a broad ridge in the autocorrelation function, the rib has resulted in widening of the autocorrelation peak.

A method developed specifically for the purpose of bone subtraction for dynamic imaging using a synchrotron X-ray source is presented in the following paper. The

basis of the technique, dual energy imaging, is an established method of performing material decomposition. Typically it is performed using an X-ray source capable of rapidly switching voltage. Since a synchrotron X-ray source's energy can't be rapidly switched in this fashion, to marry the benefits of synchrotron radiation and dual energy imaging, there is a need for a synchrotron-based methods of performing dual energy imaging.

The following method makes use of the usually unwanted higher harmonic energies, in addition to the fundamental energy produced by a crystal monochromator, to effectively create a dual energy source. A series of inline scintillating screens separated by a metal spectral filter are then used to simultaneously capture low and high energy images. A full description of the method and an example of material separation of bone and soft tissue can be found in the paper.

Using this technique it is possible to achieve bone free images of the lung fields with high temporal resolution. These images are suitable for analysis techniques such as dynamic volume measurement (Kitchen et al., 2008) and autocorrelation-based measurement of alveolar size, the focus of the final two chapters.

4.1 Article - Single-exposure dual-energy-subtraction X-ray imaging using a synchrotron source

The following paper was published in 2012 in *The Journal of Synchrotron Radiation*. This work was co-authored by A. Fouras and M.J. Kitchen. The paper is reproduced in this thesis directly from the published version.

Monash University

Declaration for Thesis Section 4.1

Declaration by candidate

In the case of Section 4.1, the nature and extent of my contribution to the work was the following:

Nature of contribution	Extent of contribution (%)
Initiated the paper, conducted experiments, performed analysis and wrote manuscript.	85

The following co-authors contributed to the work. If co-authors are students at Monash University, the extent of their contribution in percentage terms must be stated:

Name	Nature of contribution	Extent of contribution (%) for student co-authors only
A. Fouras	Performed experiments, supported analysis and revised manuscript.	NA
M. J. Kitchen	Performed experiments, supported analysis and revised manuscript.	NA

The undersigned hereby certify that the above declaration correctly reflects the nature and extent of the candidate's and co-authors' contributions to this work*.

Candidate's Signature  Date 11/12/2016

Main Supervisor's Signature  Date 11/12/2016

*Note: Where the responsible author is not the candidate's main supervisor, the main supervisor should consult with the responsible author to agree on the respective contributions of the authors.



Single-exposure dual-energy-subtraction X-ray imaging using a synchrotron source

R. P. Carnibella,^{a,b*} A. Fouras^{a,b} and M. J. Kitchen^c

^aDivision of Biological Engineering, Monash University, Wellington Road, Clayton, Victoria 3800, Australia, ^bDepartment of Mechanical and Aerospace Engineering, Monash University, Wellington Road, Clayton, Victoria 3800, Australia, and ^cSchool of Physics, Monash University, Wellington Road, Clayton, Victoria 3800, Australia. E-mail: richard.carnibella@monash.edu

Projection radiography of the chest has long been plagued by the presence of bony anatomy obscuring visibility of the lungs and heart. Dual-energy subtraction is a well known method for differentiating bone and soft tissue, but existing techniques are not ideally suited to dynamic imaging. Herein a new technique to address this problem is presented. The harmonic content of a monochromated X-ray beam is exploited, and two in-line detectors are used to perform single-exposure dual-energy imaging. Images of a phantom demonstrate the ability to both separate and quantitatively measure the thickness of constituent materials, whilst images of a mouse thorax demonstrate the ability to separate bone and soft tissue in a biological specimen. The technique is expected to improve the performance of dynamic lung imaging.

Keywords: dual-energy imaging; digital subtraction imaging; basis material decomposition; dynamic imaging; X-ray imaging.

1. Introduction

Two significant problems with projection X-ray imaging are the difficulty in differentiating superimposed structures and the related problem of quantitatively measuring the material properties of individual structures. Dual-energy X-ray imaging is one technique which can overcome these limitations. Consequently, some of the applications of dual-energy imaging include bone differentiation on chest X-rays for the purpose of improving tumour diagnosis (Fraser *et al.*, 1986; Kelcz *et al.*, 1994), the diagnosis of cerebral haemorrhage (Brockmann *et al.*, 2010), lung perfusion measurement (Thieme *et al.*, 2008), cardiac imaging (Schwarz *et al.*, 2008), the diagnosis of urinary calculi (Graser *et al.*, 2008) and gout (Choi *et al.*, 2009), and bone and fat density measurement (Sartoris & Resnick, 1989; Jensen *et al.*, 1995).

Growing interest in dynamic synchrotron X-ray imaging has created demand for new methods of performing dual-energy imaging, which can be used with a synchrotron source and which are suitable for dynamic imaging. In particular, there is need for a means of subtracting bone from dynamic lung images. The shadows produced by the ribcage and spine are a problem for regional lung volume measurement techniques (Kitchen *et al.*, 2008), which regard the chest as a two-component system consisting of air and soft tissue. Regional lung volume measurements, from dynamic image sequences recorded at synchrotrons, have enabled researchers to assess the efficacy of ventilation strategies employed to safely aerate the lungs of premature neonates born with poor lung function

(Hooper *et al.*, 2009). In other studies, researchers have quantified the mechanics of lung tissue associated with detecting early-stage pulmonary disease using synchrotron-based imaging techniques (Fouras *et al.*, 2012). In that work the visibility of the ribcage was artificially suppressed in order to isolate the motion of the lung tissue.

An alternative to dual-energy imaging for bone subtraction has been developed by Suzuki *et al.* (2006), using a massive training artificial neural network. That approach, however, can be impractical because of the number of training samples required. A recent study (Kitchen *et al.*, 2011) showed that dynamic lung image segmentation can be performed in the context of phase-contrast X-ray imaging, using a Laue analyser crystal, to reconstruct the complex refractive index of a two-material system. However, that technique is complicated by the ultra-small-angle scattering arising from the airways, which increases the complexity of the reconstruction procedure.

Digital dual-energy imaging was pioneered by Brody *et al.* (1981) and Lehmann *et al.* (1981) who outlined the theory of basis material decomposition and demonstrated bone and soft tissue subtraction on chest X-ray images. They used a rapidly switching polychromatic X-ray source to sequentially capture low- and high-energy images (dual exposures). In this set-up the delay between capturing the dual-energy images limits the rate at which dynamic imaging can be performed and means rapidly moving subjects are prone to motion artefacts. Xu *et al.* (2011) developed a dual-energy system using flat panel detectors with a 15 ms delay, which can acquire image pairs at

up to 15 frames a second. Another issue, pertaining to the use of a polychromatic source, is the non-linear relationship between the log intensity measurements and material thickness (Brody *et al.*, 1981). The problem is not intractable, but requires extensive calibration and is often handled qualitatively by adjusting a weighting factor until satisfactory material subtraction is achieved.

An alternative to dual-exposure approaches is to selectively capture X-rays of different energies from a single exposure to polychromatic radiation, rather than changing the source energy. Single-exposure dual-energy imaging systems (Speller *et al.*, 1983; Ishigaki *et al.*, 1986) have been developed, which consist of a piece of metal, acting as a high-pass X-ray filter, sandwiched between two imaging plates or film-screen cassettes. By simultaneously capturing low- and high-energy images, motion artefacts are eliminated. Such an analogue detection medium is not, however, suitable for dynamic imaging. Phillips are developing a dual-layer sandwich detector (Phillips, 2008), which will be able to simultaneously record dual-energy images, but to date the technology is not commercially available.

To perform dual-energy tomography with a synchrotron source, Torikoshi *et al.* (2001, 2003) designed a system using the harmonic energy content of a monochromated X-ray beam to provide dual energies and used a rotating filter to alternately image at each energy.

The method presented in this paper is an evolution of the early single-exposure systems, optimized to work with a synchrotron source and digital detectors. Like Torikoshi *et al.* (2001, 2003), a key feature of the technique is the use of the harmonic energy content of a monochromated X-ray beam, but here we simultaneously acquire images at both energies using two detectors. The harmonic beam allows better energy separation than polychromatic sources and also significantly simplifies the systems of equations that need to be solved. Consequently, more accurate results can be expected, with the method only requiring a relatively simple calibration procedure. The paper first outlines the system design and theory of material decomposition. We then present experimental results from a phantom to demonstrate the accuracy of the technique followed by images of a mouse thorax to demonstrate the ability to separate bone from the soft tissues.

2. Theory and method

2.1. X-ray harmonics for dual-energy imaging

Silicon crystals are commonly used to produce a monochromatic beam from a polychromatic X-ray source. In accordance with Bragg's law,

$$n\lambda = 2d \sin \theta, \quad (1)$$

where n is an integer, λ is the wavelength of the incident wave, d is the distance between scattering planes and θ is the angle between the incident wave and scattering planes, photon energy can be selected by adjusting the angle θ at which the X-ray beam strikes the crystal. Different orders n result in the

presence of harmonic frequencies in the reflected beam at the same angle. Usually these harmonics are unwanted and efforts are taken to suppress them. For example, with double-crystal monochromators the first crystal is commonly detuned.

The experiments undertaken here were performed in experimental hutch 3 of beamline 20B2 at the SPring-8 synchrotron in Japan (Goto *et al.*, 2001). A Si(111) double-crystal monochromator was used to produce a beam with a fundamental energy of 17 keV and a third harmonic of 51 keV [the second harmonic for the Si(111) reflection is forbidden]. Although higher-order harmonics (*e.g.* the fifth, seventh, *etc.*) exist, their contribution can be neglected because each harmonic becomes progressively weaker.

Ideally, a higher fundamental energy than 17 keV is desirable for imaging macroscopic objects. However, this energy was chosen because the Gd₂O₂S:Tb (P43) phosphors used in the detectors have a *K*-edge at 50.2 keV. By placing the third-harmonic energy just beyond this (51 keV), the efficiency of the phosphor is maximized.

2.2. Dual detectors

The imaging set-up used in these experiments is illustrated in Fig. 1. A key feature is that the two phosphor screens are positioned in-line with the beam. A mirror (1 mm-thick aluminium-coated soda lime glass) angled at 45°, also on the same axis, was used to transfer the image on the first screen to a digital camera. In addition to the mirror, between the two screens was a 3 mm-thick sheet of aluminium, which acts as a high-pass energy filter.

For the front detector a PCO 4000 CCD camera (14 bit, pixel size 9.0 μm × 9.0 μm, 4000 pixels × 2672 pixels) coupled to a Nikon 105 macro lens (1.8:1 demagnification for an effective pixel size of 16.2 μm) was used in combination with a custom-made phosphor screen. The screen consisted of a

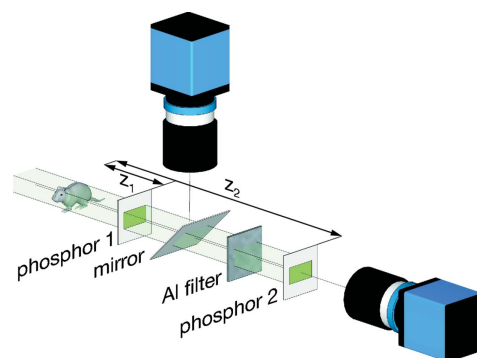


Figure 1 Single-exposure dual-energy imaging set-up using a synchrotron source. Initially the beam is dominated by the fundamental (low) energy component. An aluminium plate acts as a high-pass filter so that subsequently the harmonic (high) energy component dominates. Two phosphors and cameras simultaneously capture the low- and high-energy images. z_1 and z_2 , the distances between the sample and detectors, were 8 cm and 36 cm, respectively.

research papers

1 mm-thick quartz glass substrate, powder-coated with a 25 μm layer of P43 phosphor. For the rear detector a Hamamatsu C9300-124 CCD camera (12 bit, same Kodak CCD as the PCO 4000) with fibre-optic taper (1.8:1) was employed (Uesugi *et al.*, 2011). The fibre-optic coupling provided a high numerical aperture to increase the sensitivity for the lower-intensity second image. This configuration was used for all experiments presented in this paper.

To account for differences in alignment and magnification between detectors, a pair of images was taken of an object containing three small metallic fiducial markers. Image registration was performed using these images to produce an affine transform that could correct for discrepancies in translation, scale, rotation and shear between images recorded by the two detectors.

The rationale in choosing the materials and thicknesses of the first phosphor screen, mirror and aluminium filter was to find a balance between minimizing the contribution of the fundamental energy at the second detector while preserving the higher-energy harmonic component. The goal was that the first and second cameras in this set-up are essentially operating as low- and high-energy detectors, respectively. The actual proportion of each energy at each detector is taken into account in the decomposition process.

2.3. Material decomposition

The attenuation of X-rays by any material is an energy-dependent function of photoelectric absorption and X-ray scattering. By measuring the combined attenuation of two known materials, at two different energies, it is possible to solve for the thickness of each material (Lehmann *et al.*, 1981). The following explains how this was achieved for the imaging set-up described in the previous section.

The transmittance through each material in the path of the beam, as a function of energy, can be expressed using the Beer–Lambert attenuation law as

$$k(E) = I/I_0 = \exp[-\mu(E)t], \quad (2)$$

where I_0 and I are the intensity of the incident and transmitted beam, respectively, $\mu(E)$ is the material's linear attenuation coefficient at energy E , and t is its thickness.

The phosphor's (P43) output in the visible spectrum can be expressed as a function of its quantum efficiency (QE),

$$I(E) = S(E)[1 - k_{\text{P43}}(E)] \text{QE}_{\text{P43}}(E), \quad (3)$$

where $S(E)$ is the source strength.

The total transmittance measured by each detector is equivalent to the flat-field (direct beam) corrected image,

$$T_1 = \frac{k_{\text{sample}}(E_1)I_1(E_1) + k_{\text{sample}}(E_2)I_1(E_2)}{I_1(E_1) + I_1(E_2)} = \frac{\text{image}_1}{\text{image}_{1,\text{flat}}}, \quad (4)$$

$$T_2 = \frac{\prod^M [k_m(E_1)]k_{\text{sample}}(E_1)I_2(E_1) + \prod^M [k_m(E_2)]k_{\text{sample}}(E_2)I_2(E_2)}{\prod^M [k_m(E_1)]I_2(E_2) + \prod^M [k_m(E_2)]I_2(E_2)} = \frac{\text{image}_2}{\text{image}_{2,\text{flat}}}, \quad (5)$$

where, for the second detector, M is the number of other materials the beam passes through in addition to the sample (*i.e.* the first phosphor screen, the mirror and the aluminium filter). E_1 and E_2 are the energy of the fundamental and third harmonic, respectively.

Grouping constants, these expressions can be simplified to

$$T_1 = C_1 k_{\text{sample}}(E_1) + C_2 k_{\text{sample}}(E_2), \quad (6)$$

$$T_2 = C_3 k_{\text{sample}}(E_1) + C_4 k_{\text{sample}}(E_2), \quad (7)$$

for the first and second detectors, respectively.

The constants C_n are the fractions of the total measured transmittance attributable to each energy. If these constants are known, the sample's transmittance and then the thickness of each material can be found by solving the following simultaneous equations,

$$\begin{bmatrix} k_{\text{sample}}(E_1) \\ k_{\text{sample}}(E_2) \end{bmatrix} = \begin{bmatrix} C_1 & C_2 \\ C_3 & C_4 \end{bmatrix}^{-1} \begin{bmatrix} T_1 \\ T_2 \end{bmatrix}, \quad (8)$$

$$\begin{bmatrix} t_1 \\ t_2 \end{bmatrix} = \begin{bmatrix} \mu_1(E_1) & \mu_2(E_1) \\ \mu_1(E_2) & \mu_2(E_2) \end{bmatrix}^{-1} \begin{bmatrix} \ln^{-1}[k_{\text{sample}}(E_1)] \\ \ln^{-1}[k_{\text{sample}}(E_2)] \end{bmatrix}, \quad (9)$$

where $\mu_m(E)$ is the linear attenuation coefficient of sample material m at energy E , and t_m is its thickness. The linear attenuation coefficients used in this paper can be found in Table 1.

For decomposition of biological samples, the aim is to separate bone from soft tissue, where bone is relatively homogeneous in its composition but not its density, and soft tissue broadly includes skin, muscle, fat, internal organs, *etc.* The simplification of the body as a two-component system is valid because, in terms of attenuation, the difference between the two components can primarily be attributed to the calcium content of bone. This can be verified by observing that in the NIST database (NIST, 2011) the attenuation coefficients of various soft tissues (brain, breast, lung, muscle, ovary and testis) differ from that of water at 17 keV by at most 15% (breast). In comparison, the attenuation coefficient of bone is over 900% that of water.

2.4. Calibration

Calibration is necessary for two reasons. Firstly, because energy separation in this system is not perfect: the low-energy detector measures a small fraction of the high-energy component and *vice versa*. Secondly, calibration is a means of accounting for all the materials between the sample and second detector without specifically needing to know the attenuation coefficients of each.

Table 1
Linear attenuation coefficients (cm^{-1}) (NIST, 2011).

	17 keV	51 keV
Aluminium	14.88	0.9608
PMMA	0.9675	0.2446
Cortical bone (ICRU-44)	12.15	0.7863
Soft tissue (ICRU-44)	1.297	0.2370

The constants C_n can be determined by imaging at least two different calibration samples for which the sample's thickness and attenuation coefficients are known. For the following experiments the two calibration samples imaged were 1 mm and 2 mm sheets of aluminium. The total transmittance for each detector was calculated; for example, for the first calibration sample at the first detector,

$$T_{1,\text{calib1}} = \frac{I_{1,\text{calib1}} - I_{\text{dark}}}{I_{\text{flat}} - I_{\text{dark}}}. \quad (10)$$

The theoretical transmittance, $k_n(E)$, of calibration sample n was calculated using equation (1). Table 1 gives the attenuation coefficients for aluminium at both energies used in this paper. Finally, the following simultaneous equations can be solved to obtain the calibration constants,

$$\begin{bmatrix} C_1 \\ C_2 \end{bmatrix} = \begin{bmatrix} k_1(E_1) & k_1(E_2) \\ k_2(E_1) & k_2(E_2) \end{bmatrix}^{-1} \begin{bmatrix} T_{1,\text{calib1}} \\ T_{1,\text{calib2}} \end{bmatrix}, \quad (11)$$

$$\begin{bmatrix} C_3 \\ C_4 \end{bmatrix} = \begin{bmatrix} k_1(E_1) & k_1(E_2) \\ k_2(E_1) & k_2(E_2) \end{bmatrix}^{-1} \begin{bmatrix} T_{2,\text{calib1}} \\ T_{2,\text{calib2}} \end{bmatrix}. \quad (12)$$

3. Results and discussion

3.1. Phantom image decomposition

A simple phantom, modelling the superposition of soft tissue and bone, was constructed consisting of an aluminium step wedge, with 1.5 mm-thick steps, placed in front of a plastic (PMMA) rod with a diameter of 10 mm (Fig. 2a).

The images captured by each detector and the results of material decomposition are also presented in Fig. 2. The results show that the two materials have been clearly separated. Furthermore, for the most part, accurate quantitative values of the material thicknesses have been obtained. The largest discrepancy evident is in the thickness of the second (3 mm) aluminium step. The explanation for this discrepancy illustrates two important issues that arose over the course of conducting these experiments.

The first issue was the choice of energies. At 17 keV less than 2% of X-rays will be transmitted through a 3 mm-thick piece of aluminium. This results in the first detector, nominally the low-energy detector, being totally dominated by the high-energy component. Theoretically, this should not be an issue because both detectors are treated as dual-energy detectors according to the theory outlined in the previous section. However, when approaching the limit in which little of the low-energy beam is transmitted through the sample, the

equations become ill-conditioned and errors are magnified. A fundamental energy of around 25 keV would have been preferable, but this would place the third harmonic at 75 keV. At such a high energy the phosphor is much less sensitive and absorption contrast is diminished. A crystal monochromator capable of producing a second harmonic, which was not readily available for these experiments, could be expected to perform significantly better at energies of 25.5 and 51 keV.

The second issue was the shape and stability of the beam. The combination of the harmonic energy being physically narrower, in addition to having a narrower rocking curve than the fundamental energy, resulted in the system being sensitive to drift and intensity fluctuations of the harmonic component. When operating on images taken at different time points, e.g. flat-field images and calibration images, even a small shift of the harmonic can result in the introduction of significant errors. We estimate the error arising in the calculation of the transmittance at the second detector alone to be as much as 4% per pixel of vertical displacement of the harmonic. During

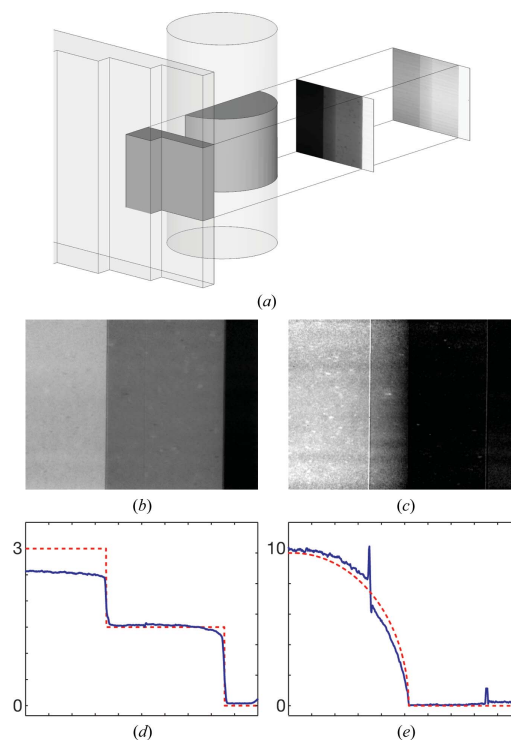


Figure 2
(a) Region of plastic rod and aluminium step wedge imaged using the dual-energy set-up. (b) Thickness of the aluminium wedge extracted by dual-energy decomposition. (c) Thickness of the plastic rod. The solid blue lines in (d) and (e) are the averaged cross-sectional thickness (mm) through each material; the dotted red lines are the actual thickness. The horizontal scale in subfigures (b)–(e) is consistent; ticks on the horizontal axes in (d) and (e) are spaced 1 mm apart.

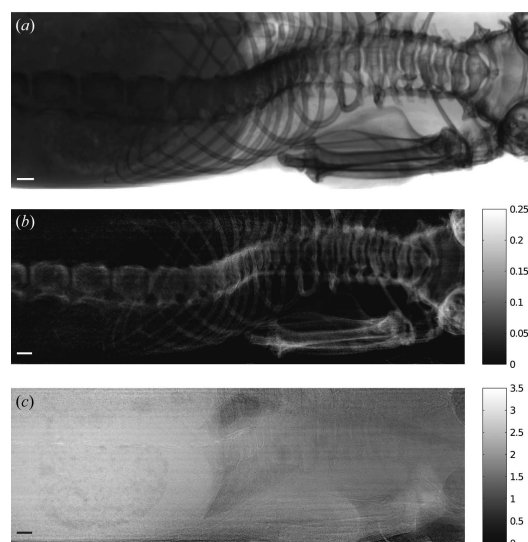


Figure 3
 (a) Plain X-ray image recorded by the first (low-energy) detector. (b) Bone image obtained by dual-energy subtraction. (c) Soft tissue image. In addition to separating these components the thickness (in cm) of each material is given. Bars in the lower left corner of each subfigure are 1 mm long.

the course of the experiments we estimate the rate of vertical harmonic drift at around $1.3 \text{ pixels min}^{-1}$. To compensate for the effects of this drift, the harmonic peaks were manually realigned before performing operations on images taken at different time points. The results in Figs. 2 and 3, in comparison with those obtained without this compensation (not shown), show a significant improvement in accuracy. Ideally, a more stable beam or more thorough beam tracking throughout the experiment could have further improved the quality of the results.

As a final observation, the image of the rod thickness (Fig. 2c) shows the presence of strong vertical lines corresponding to the edges of the aluminium step. These are the result of propagation-based phase contrast (Snigirev *et al.*, 1995; Wilkins *et al.*, 1996) produced by the edges of the step wedge. The decomposition algorithm outlined in this paper is based on a model of absorption contrast and therefore does not account for the effects of diffraction. The simplest measure to reduce phase contrast is to minimize the distance between the sample and detectors, since this phase contrast is propagation-based. It should also be pointed out that in biological samples such abrupt sharp edges are rare so that at short propagation distances phase contrast is much weaker.

3.2. Mouse thorax image decomposition

A small mouse was also imaged and a decomposition performed to separate bone from soft tissue. The results are presented in Fig. 3. Qualitatively, we see that the bones have

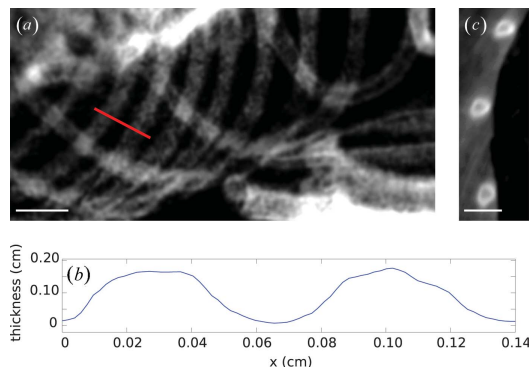


Figure 4
 (a) Bone image (projected thickness) of a section of a mouse ribcage. An averaged cross section through the two ribs cut by the diagonal red line can be seen in (b). (c) A CT cross section through some ribs from a similar mouse, highlighting their non-uniform bone density. Bars in the lower left corner of subfigures (a) and (c) are 1 mm long.

been clearly separated from the soft tissue. In Fig. 3(c) the shadow or impression of the bones that have been removed is visible upon close inspection. In some situations this is not desirable, for example with correlation-based lung motion tracking algorithms (Fouras *et al.*, 2011), in which case adding the equivalent bone thickness back to the soft tissue thickness will remove, or at least significantly reduce, these shadows.

Quantitative values for both the thickness of bone and soft tissue are in keeping with the external dimensions of the mouse. In Fig. 4(a), which is a magnified bone image of a section of the ribcage, a cross section through two ribs measures their thickness to be approximately half their width (Fig. 4b). A computed-tomography (CT) cross section through some mouse ribs is also presented (Fig. 4c), which highlights their non-uniform bone density. The discrepancy in thicknesses can be understood by considering that dual-energy decomposition is specifically measuring the thickness of cortical (compact) bone, and, because most bones are less dense in the centre (cancellous or spongy), this technique will tend to underestimate their anatomical thickness.

A final point is that these were static images of a deceased mouse. In theory the only limitation to the speed of dynamic imaging with this method is the intensity of the beam and sensitivity of the detectors, since low- and high-energy images are taken simultaneously. With a bright synchrotron source and high-sensitivity digital detectors, we anticipate that quantitative image reconstruction will be possible at video frame rates. This remains the work of future studies.

4. Conclusion

A single-exposure method for performing dual-energy-subtraction imaging with a synchrotron source has been presented. The accuracy of the technique for performing qualitative measurement of material thicknesses and the ability to separate bone and soft tissue in a small animal

specimen have been demonstrated. This method has applications for improving the performance of dynamic lung imaging techniques performed with synchrotron sources.

The authors gratefully acknowledge support from Australian Research Council (ARC) grants (Grant Nos. DP110101941 and DP110101498). RPC is a recipient of an Australian Postgraduate Award. MJK is an ARC Australian Research Fellow. We acknowledge useful discussions with R. A. Lewis in the preparation of this paper. We acknowledge travel funding provided by the International Synchrotron Access Program (ISAP) managed by the Australian Synchrotron.

References

- Brockmann, C., Scharf, J., Nölte, I. S., Seiz, M., Groden, C. & Brockmann, M. A. (2010). *Clin. Neuroradiol.* **20**, 231–235.
- Brody, W. R., Butt, G., Hall, A. & Macovski, A. (1981). *Med. Phys.* **8**, 353–357.
- Choi, H. K., Al-Arfaj, A. M., Eftekhari, A., Munk, P. L., Shojania, K., Reid, G. & Nicolaou, S. (2009). *Ann. Rheum. Dis.* **68**, 1609–1612.
- Fouras, A., Allison, B. J., Kitchen, M. J., Dubsky, S., Nguyen, J., Hourigan, K., Siu, K. K. W., Lewis, R. A., Wallace, M. J. & Hooper, S. B. (2012). *Ann. Biomed. Eng.* **40**, 1160–1169.
- Fraser, R. G., Hickey, N. M., Niklason, L. T., Sabbagh, E. A., Luna, R. F., Alexander, C. B., Robinson, C. A., Katzenstein, A. L. & Barnes, G. T. (1986). *Radiology*, **160**, 595–601.
- Goto, S., Takeshita, K., Suzuki, Y., Ohashi, H., Asano, Y., Kimura, H., Matsushita, T., Yagi, N., Isshiki, M., Yamazaki, H., Yoneda, Y., Umetani, K. & Ishikawa, T. (2001). *Nucl. Instrum. Methods Phys. Res. A*, **467–468**, 682–685.
- Graser, A., Johnson, T. R., Bader, M., Staehler, M., Haseke, N., Nikolaou, K., Reiser, M. F., Stief, C. G. & Becker, C. R. (2008). *Invest. Radiol.* **43**, 112–119.
- Hooper, S. B., Kitchen, M. J., Siew, M. L. L., Lewis, R. A., Fouras, A., te Pas, A. B., Siu, K. K. W., Yagi, N., Uesugi, K. & Wallace, M. J. (2009). *Clin. Exp. Pharmacol. Physiol.* **36**, 117–125.
- Ishigaki, T., Sakuma, S., Horikawa, Y., Ikeda, M. & Yamaguchi, H. (1986). *Radiology*, **161**, 271–273.
- Jensen, M. D., Kanaley, J. A., Reed, J. E. & Sheedy, P. F. (1995). *Am. J. Clin. Nutr.* **61**, 274–278.
- Kelcz, F., Zink, F. E., Peppler, W. W., Kruger, D. G., Ergun, D. L. & Mistretta, C. A. (1994). *Am. J. Roentgenol.* **162**, 271–278.
- Kitchen, M. J., Lewis, R. A., Morgan, M. J., Wallace, M. J., Siew, M. L. L., Siu, K. K. W., Habib, A., Fouras, A., Yagi, N., Uesugi, K. & Hooper, S. B. (2008). *Phys. Med. Biol.* **53**, 6065–6077.
- Kitchen, M. J., Paganin, D. M., Uesugi, K., Allison, B. J., Lewis, R. A., Hooper, S. B. & Pavlov, K. M. (2011). *Phys. Med. Biol.* **56**, 515–534.
- Lehmann, L. A., Alvarez, R. E., Macovski, A., Brody, W. R., Pelc, N. J., Riederer, S. J. & Hall, A. L. (1981). *Med. Phys.* **8**, 659–667.
- NIST (2011). *X-ray Mass Attenuation Coefficients*, <http://www.nist.gov/pml/data/xraycoef/index.cfm>.
- Phillips (2008). *Exploring the spectrum – advances and potential of spectral CT*. http://clinical.netforum.healthcare.philips.com/us_en/Explore/White-Papers/CT/Exploring-the-spectrum-Advances-and-potential-of-spectral-CT.
- Sartoris, D. J. & Resnick, D. (1989). *Am. J. Roentgenol.* **152**, 241–246.
- Schwarz, F., Ruzsics, B., Schoepf, U. J., Bastarrika, G., Chiamida, S. A., Abro, J. A., Brothers, R. L., Vogt, S., Schmidt, B., Costello, P. & Zwerner, P. L. (2008). *Eur. J. Radiol.* **68**, 423–433.
- Snigirev, A., Snigireva, I., Kohn, V., Kuznetsov, S. & Schelokov, I. (1995). *Rev. Sci. Instrum.* **66**, 5486–5492.
- Speller, R. D., Ensell, G. J. & Wallis, C. (1983). *Brit. J. Radiol.* **56**, 461–465.
- Suzuki, K., Abe, H., MacMahon, H. & Doi, K. (2006). *IEEE Trans. Med. Imaging*, **25**, 406–416.
- Thieme, S. F., Becker, C. R., Hacker, M., Nikolaou, K., Reiser, M. F. & Johnson, T. R. (2008). *Eur. J. Radiol.* **68**, 369–374.
- Torikoshi, M., Tsunoo, T., Endo, M., Noda, K., Kumada, M., Yamada, S., Soga, F. & Hyodo, K. (2001). *J. Biomed. Opt.* **6**, 371–377.
- Torikoshi, M., Tsunoo, T., Sasaki, M., Endo, M., Noda, Y., Ohno, Y., Kohno, T., Hyodo, K., Uesugi, K. & Yagi, N. (2003). *J. Biomed. Opt.* **48**, 673–685.
- Uesugi, K., Hoshino, M. & Yagi, N. (2011). *J. Synchrotron Rad.* **18**, 217–223.
- Wilkins, S. W., Gureyev, T. E., Gao, D., Pogany, A. & Stevenson, A. W. (1996). *Nature (London)*, **384**, 335–338.
- Xu, T., Ducote, J. L., Wong, J. T. & Molloy, S. (2011). *Phys. Med. Biol.* **56**, 1191–1205.

5 Measuring alveolar dimensions

In this chapter we turn our attention to the application of autocorrelation-based analysis of X-ray speckle to measure the distribution of alveolar size in the lungs. In the previous chapter a method to separate and remove bone from chest X-ray images was outlined. The motivation for developing this method was to produce high temporal resolution, bone free images of the speckle pattern produced by alveoli in the lungs that would be suitable for autocorrelation-based analysis. Overlying bones (specifically the ribs, and to a lesser extent the spine) are problematic when attempting to study alveolar speckle because they tend to dominate the autocorrelation function due to their size and intensity.

However, the method of single exposure, dual energy bone subtraction described in the previous chapter is currently limited to absorption-based X-ray imaging. The key equations are based on the Beer-Lambert law, which describes X-ray attenuation in matter. To be applicable in phase contrast imaging, these equations would need to be expanded to also incorporate the contribution of phase contrast. The relevant theory is described in section 1.4.1 but its application to dual energy imaging is not trivial (to begin with the system of equations will no longer be linear). Additionally, without significant hardware upgrades — the X-ray/optical systems used in section 4.1 are too inefficient — the relatively poor signal-to-noise ratio of that dual energy imaging system is an issue.

Until these challenges can be overcome, to move forward with the stated objective of measuring alveoli, a method for achieving equivalent bone suppression in phase contrast X-ray images of the lungs is needed. In the paper accompanying this chapter (section 5.5) an alternative approach to bone suppression is outlined based on image filtering in the frequency domain, which is shown to achieve equivalent results to dual energy bone subtraction, and is used to demonstrate the measurement of the distribution of alveolar diameter in the lungs.

In the paper, a technique for bone subtraction by segmentation and reprojection of phase contrast CT is used to demonstrate the equivalency of the image frequency filtering technique. Due to the relatively concise description of the methodology provided in the paper, a more detailed description of the CT-based bone subtraction technique, the frequency filtering technique, and their equivalency is provided in the following sections.

5.1 Computed tomography bone subtraction and reprojec-tion

5.1.1 Phase contrast enhanced computed tomography

The method for performing propagation-based phase contrast CT is described in section 3 of the accompanying paper.

CT reconstruction can be performed using any available reconstruction technique — filtered back projection was used here. In phase contrast CT a phase retrieval step is typically included to effectively “undo” the phase contrast edge enhancement and obtain low noise, quantitative CT images. Here, because we would like to preserve the phase contrast for the subsequent autocorrelation-based analysis, we skip the phase retrieval step: CT reconstruction is performed exactly as for a conventional scan.

5.1.2 Bone segmentation and reprojec-tion

Separating the bones and lungs on CT can be achieved by either segmenting the lungs and removing the remainder (the method used in the paper) or just segmenting and removing the bones themselves. Differing from the paper slightly, here the latter method was used because the resulting reprojected slices can be compared back directly to the original unprocessed projections.

Segmentation of the lungs (airspace) was performed using a region growing segmentation algorithm (commonly referred to as a magic wand tool, e.g. Avizo 3D software magic wand). This method requires the user to select a seed location somewhere in the airspace (the trachea is an obvious choice) and an intensity threshold (midway between the mean tissue and mean air intensity was found to work well). Morphological closing using a cubic $3 \times 3 \times 3$ voxel element will grow the segmentation boundary by around 3 voxels and help ensure that the lungs are completely encapsulated in the segmentation. Voxels outside the lungs are replaced by the mean soft tissue attenuation coefficient.

Segmentation of the bones is even more straightforward. Simple intensity-based thresholding can be used with the threshold set between the the mean tissue and mean bone intensities; a setting slightly below the mean bone intensity was found to work well. Again morphological closing with a $3 \times 3 \times 3$ voxel element helps to ensure sure that the bone edges are completely captured in the segmentation. The voxels of segmented bone were replaced with the mean soft tissue intensity. This technique produces output equivalent to the the dual energy bone subtraction technique outlined in the previous chapter. The sequence of steps is illustrated in Figure 5.1.

The common final step in both approaches is to reproject the now bone free volu-



Figure 5.1: Sequence of phase contrast CT images illustrating the process of bone segmentation and removal. Beginning with the raw CT reconstruction (left), bones are thresholded by intensity (centre; shown in red) and replaced by the mean tissue intensity (right).

metric CT data. This process consists of ray casting to simulate X-ray image formation. In the case of synchrotron imaging where the X-ray beam is essentially parallel, this task is straightforward: a single ray projected through the CT volume corresponds to the position of each pixel on the detector.

The CT volume is integrated along the length of each ray to determine the intensity, p , at detector location t, r , according to

$$\log(p(t, r)) = - \int \mu(x, y, z) dr$$

where $\mu(x, y, z)$ is the CT tissue attenuation coefficient at location x, y, z (see Figure 5.2). By rotating the CT volume, or equivalently the X-ray source and detector positions, about the z axis a projected image through the CT volume can be obtained at any angle.

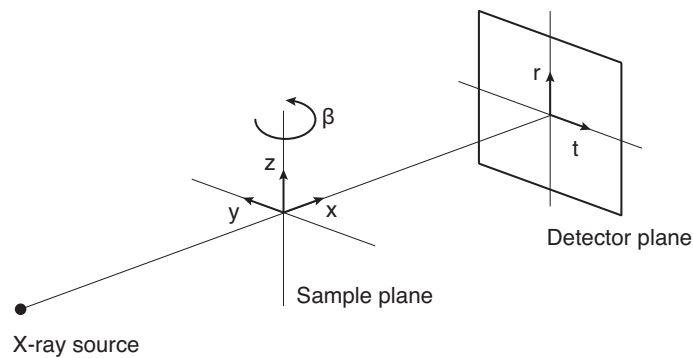


Figure 5.2: Illustration of the planes and coordinate systems for CT reprojection.

To test the reprojection process in isolation (without bone subtraction) we can look at how closely the reprojected images match the original CT projections. These two images are compared in Figure 5.3 and show good agreement.

Finally, in Figure 5.4 we see a comparison between the original projection image and its equivalent, bone free, reprojected image.

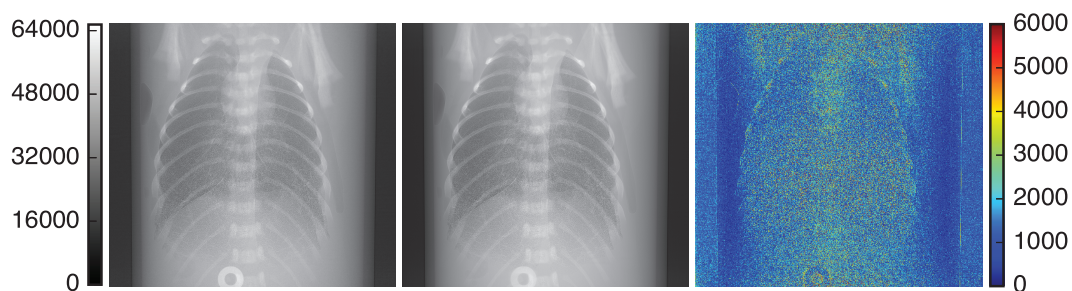


Figure 5.3: A single projection image (left) and corresponding reprojected image (centre) of a rabbit pup chest. The absolute difference between these 16-bit images has also been calculated (right). The root mean square difference is 1813.

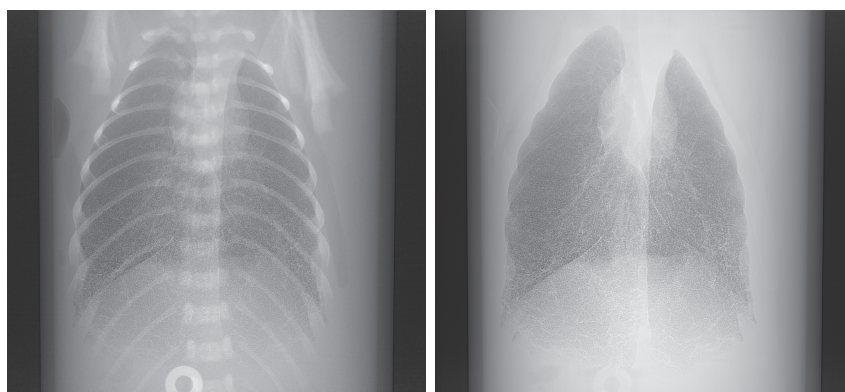


Figure 5.4: A single projection image (left) and corresponding bone free reprojected image (right) of a rabbit pup chest.

5.2 Spatial frequency filtering

In the accompanying paper, spatial frequency filtering is used to suppress larger structures, such as bones, while maintaining a strong lung speckle signal. A second order Butterworth filter is used to perform image spatial frequency filtering before autocorrelation-based analysis. The choice of a Butterworth filter was somewhat arbitrary: a Gaussian or other filter shape may work equally well. The filter is applied

in the frequency domain using fast Fourier transforms. The Butterworth filter kernel is can be expressed as

$$H = \left(1 - \frac{1}{1 + \left(\frac{u^2+v^2}{f_L^2} \right)^2} \right) \frac{1}{1 + \left(\frac{u^2+v^2}{f_H^2} \right)^2}$$

where u and v are image coordinates in the frequency domain, and f_L and f_H are the lower and upper cut-off frequencies, respectively. The lower cut-off frequency is chosen to suppress structures larger than the lung speckle and the upper cut-off frequency to suppress image noise. In the paper, only a lower cut-off frequency is specified (i.e. it is a high pass filter) at 1/32 cycles per pixel.

The filter is applied using the Fourier transform pair

$$I_{filtered} = \text{IFFT}(\text{FFT}(I) \cdot H)$$

where I is the original image and FFT and IFFT are the fast fourier and inverse fast fourier transforms, respectively.

A comparison between frequency filtered projection and bone free reprojected images is provided in Figure 5.5. It can be seen that the bones haven't been completely suppressed, but it will be seen in the following section that they have little influence on the globally averaged autocorrelation function. However, it does highlight the potential value of a more effective bone suppression technique to improve the performance of regional analysis (regional analysis is covered in the next chapter).

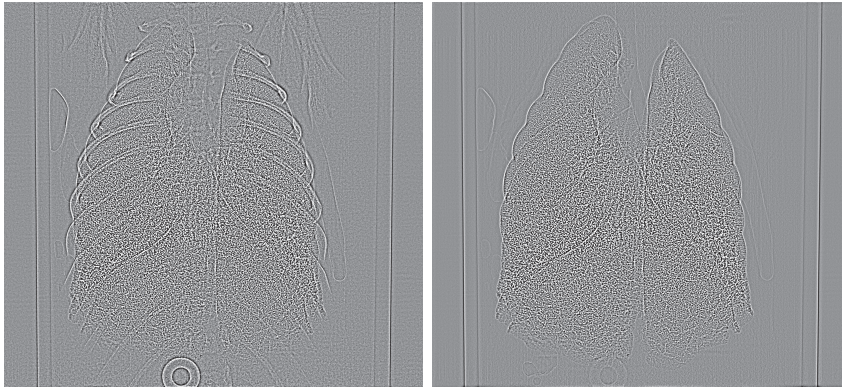


Figure 5.5: Frequency filtered projection (left) and bone free reprojected (right) lung images (cut-off frequencies: $f_L = 1/32$ cycles per pixel and $f_H = 1/5$ cycles per pixel).

5.3 Comparison of autocorrelation functions using bone subtraction and frequency filtering

Figure 7 in the paper is a comparison of alveolar size distributions showing the equivalency of frequency filtering with or without prior bone subtraction. To support the decision to use frequency filtering, additional analysis is presented here, showing the autocorrelation functions of the lung speckle to also be equivalent. This is achieved by comparing the autocorrelation of the lung speckle in the two frequency filtered images in Figure 5.5 — that is with and without bone subtraction. The technique for obtaining the global autocorrelation function is as described in the paper and is based on the same imaging data. The resulting autocorrelation functions are presented in Figure 5.6.

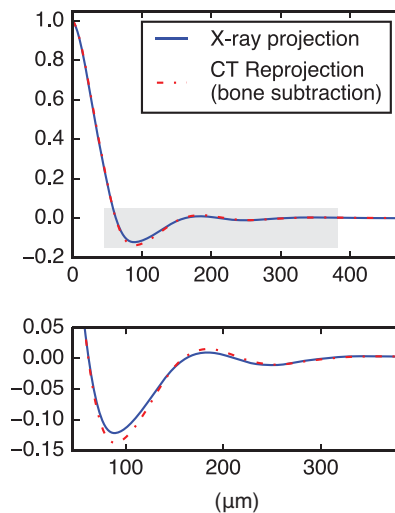


Figure 5.6: The upper image contains the spatial autocorrelation functions for a single X-ray projection (solid blue) and a bone-free reprojected image (dot-dashed red) of the same rabbit pup chest. Identical frequency filtering was first applied to both X-ray images. The lower plot is a magnified view of the shaded region around the first few correlation peaks.

In Figure 5.6 we can see there is close agreement between the autocorrelation function obtained by both methods (root mean square difference of 0.06). This result, together with the comparison between measured alveolar distributions in Figure 7 in the paper, suggests that frequency filtering alone provides sufficient bone suppression for the purpose of autocorrelation-based analysis of X-ray lung speckle.

5.4 Concluding comments on bone suppression

In this extended introduction to the paper we have seen how spatial frequency filtering, as a preprocessing measure, can be applied to phase contrast chest X-ray images. This technique is used in the paper that follows and throughout the work on measuring dynamic lung function in chapter 6. As such, it has proven to be a simple but effective alternative to more onerous bone subtraction techniques such as dual energy imaging.

5.5 Article - Single-shot X-ray measurement of alveolar size distributions

The following paper was published in 2014 in *Proceedings SPIE 9038, Medical Imaging 2014: Biomedical Applications in Molecular, Structural and Functional Imaging 2014*. This work was co-authored by M.J. Kitchen and A. Fouras. The paper is reproduced in this thesis directly from the published version.

Monash University

Declaration for Thesis Section 5.5

Declaration by candidate

In the case of Section 5.5, the nature and extent of my contribution to the work was the following:

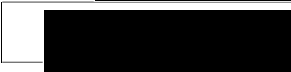
Nature of contribution	Extent of contribution (%)
Initiated the paper, conducted experiments, performed analysis and wrote manuscript.	85

The following co-authors contributed to the work. If co-authors are students at Monash University, the extent of their contribution in percentage terms must be stated:

Name	Nature of contribution	Extent of contribution (%) for student co-authors only
A. Fouras	Performed experiments, supported analysis and revised manuscript.	NA
M. J. Kitchen	Performed experiments, supported analysis and revised manuscript.	NA

The undersigned hereby certify that the above declaration correctly reflects the nature and extent of the candidate's and co-authors' contributions to this work*.

Candidate's Signature  Date 11/12/2016

Main Supervisor's Signature  Date 11/12/2016

*Note: Where the responsible author is not the candidate's main supervisor, the main supervisor should consult with the responsible author to agree on the respective contributions of the authors.

Single-shot X-ray measurement of alveolar size distributions

Richard P. Carnibella^{*a}, Marcus J. Kitchen^b, Andreas Fouras^a

^aDepartment of Mechanical Engineering, Monash University, Melbourne, 3800, Australia; ^bSchool of Physics, Monash University, Melbourne, 3800, Australia

ABSTRACT

Regional changes in lung microstructure are an important component of several common lung disorders and even in healthy lungs alveolar mechanics are poorly understood. Existing techniques capable of studying the lung microstructure have various limitations including poor temporal resolution. We present a technique, which can measure the distribution of alveolar diameters from a single, phase contrast chest X-ray. We present the results of analysis of synchrotron images of a rabbit pup's lungs, which we compare with high-resolution computed tomography images. We demonstrate that measurements can be made with an exposure time of 40 ms, highlighting the unique potential for performing dynamic *in vivo* measurements. Applications include disease detection, assessment of therapeutics and physiological studies.

Keywords: phase contrast, X-ray imaging, dynamic imaging, functional imaging, lung imaging, alveolar size

1. INTRODUCTION

Regional changes in lung microstructure are the predominant characteristic of several common lung disorders, such as emphysema and chronic obstructive pulmonary disease (COPD), and are increasingly of interest to those studying the pathophysiology of asthma¹. Additionally, the mechanics of alveoli in the breathing lung has been a long standing topic of contention amongst physiologists^{2,3}.

However, it has only been in recent years that imaging techniques have allowed researchers and clinicians to explore this domain.

Magnetic resonance imaging (MRI) with hyperpolarized noble gases is a functional lung imaging technique that has attained considerable popularity of late. The apparent diffusion coefficient (ADC) of these gases can be used directly as a relative measure of microstructural abnormalities⁴. Efforts have been made, using alveolar models, to obtain quantitative measurements from ADCs⁵. However, a significant factor limiting more widespread adoption of these techniques is the cost and difficulty in producing and obtaining the hyperpolarized gases. Another factor is machine dependence and poor repeatability of results. Additionally, measurements of alveolar morphology during lung inflation have required the need to use breath-holding techniques³, which presents a practical difficulty as well as a deviation from normal physiological respiration.

High resolution computed tomography (CT) offers an alternative means of studying lung microstructure. Acquisition of time series data can be achieved by breath-hold maneuvers, by machines capable of sub-second scan times⁶, and by gating techniques⁷. Individual alveoli can be clearly visualized in post mortem CT scans of small animal lungs using synchrotron sources. However, this level of resolution is difficult to achieve in a live animal due to both respiratory and cardiac motion. Radiation dose is also a potential issue for living subjects.

Propagation based phase contrast X-ray imaging is a technique utilizing a spatially coherent source, such as a synchrotron or micro-focus lab source, to achieve superior contrast in weakly absorbing media like the lungs⁸. Phase contrast images of the lungs have a strongly speckled appearance due to the superposition of many alveoli⁹. Dynamic X-ray velocimetry techniques^{10,11} can measure lung motion by exploiting the strong speckle contrast and are capable of quantifying regional tidal volumes. However, they are unable to retrieve quantitative morphological information.

*richard.carnibella@monash.edu; ldi.monash.edu

Medical Imaging 2014: Biomedical Applications in Molecular, Structural, and Functional Imaging,
edited by Robert C. Molthen, John B. Weaver, Proc. of SPIE Vol. 9038, 90380V
© 2014 SPIE · CCC code: 1605-7422/14/\$18 · doi: 10.1117/12.2043415

Proc. of SPIE Vol. 9038 90380V-1

Downloaded From: <http://proceedings.spiedigitallibrary.org/> on 07/30/2015 Terms of Use: <http://spiedigitallibrary.org/ss/TermsOfUse.aspx>

In previous work we have shown that the speckle produced by an idealized (non-penetrating, spherical) porous medium contains information about the underlying porous structure and that the distribution of pore sizes can be accurately determined¹². We hypothesize that the speckle produced by the lungs can be analysed in the same manner and that the distribution of alveolar sizes similarly measured.

Here we present a technique for measuring alveolar dimensions from a single X-ray image together with experimental results from analysis of a rabbit pup's lungs. The technique uses a simple imaging procedure, is capable of high temporal resolutions, and requires minimal radiation dose.

2. DESCRIPTION OF TECHNIQUE

The main concepts and details related to the technique are described in detail in a previous publication¹². Briefly, the idea is to simulate X-ray images of a distribution of randomly packed non-penetrating spheres and to use an inverse method (solver) to match the spatial autocorrelation function (SAF) of this image with that measured experimentally. Some minor alterations to the procedure used in our previous work were necessary, which we will outline presently.

An additional parameter, porosity, has been added to our packed sphere model. To achieve this, the volume is first packed with the desired number of small spheres, which are then allowed to grow to achieve the desired porosity and size distribution. The sphere growing was performed using LIGGGHTS¹³ discrete element method software.

The solver has also been modified to only attempt to fit a specified subsection of the SAF: the region around the second trough [See Figs. 5(a,b)]. Our rationale is as follows. The secondary peaks and troughs in the SAF inform us of periodic structure(s) within the lung and we contend that this must almost exclusively be due to the tightly packed alveoli. The primary peak and trough are affected by other structures, such as terminal bronchioles and alveolar ducts, which are not as strongly periodic and that our current (spherical) model cannot account for. Additionally, because the signal to noise ratio of the SAF increases along the horizontal axis, solutions using the entire tail tend to be unstable, so we also truncate the tail.

3. EXPERIMENTAL METHODS

A scavenged rabbit pup (at 29 days gestational age) served as our sample. The pup, which had previously been mechanically ventilated, was inflation fixed with nitrogen at a pressure of 27 cmH₂O and then set in agar in a cylindrical plastic tube.

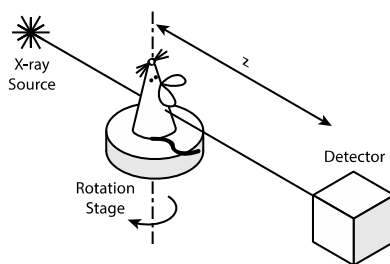


Figure 1. Schematic of the experimental imaging setup. A synchrotron or microfocus lab source is typically used to produce phase contrast. Propagation based phase contrast is achieved by allowing a propagation distance, z , between the sample and detector.

Imaging was performed on beamline BL20B2 at the Spring-8 synchrotron, Japan¹⁴. We used a propagation based phase contrast X-ray imaging technique, in which the X-ray detector was placed a distance of 0.975 m behind the sample. We used a monochromatic beam with an energy of 24 keV. 1800 images of the sample were taken between rotation angles of 0 and 180 degrees with 40 ms exposure times. Images were captured using BM5¹⁵ coupled to a pco.edge sCMOS

camera. The resultant 2042×2062 pixel images had an effective pixel size of 15.3 μm. Flat and dark field corrections were applied to all images.

At this point the images were handled in two different ways. One process began by performing a phase contrast CT reconstruction of the chest. The entire airway tree and distal airspaces were then segmented using Avizo® 3D analysis software. Any voxels outside the lungs were filled with a tissue equivalent grey level. Finally, the volume was forward projected to produce an X-ray image of only the lungs [Fig. 2(a)].

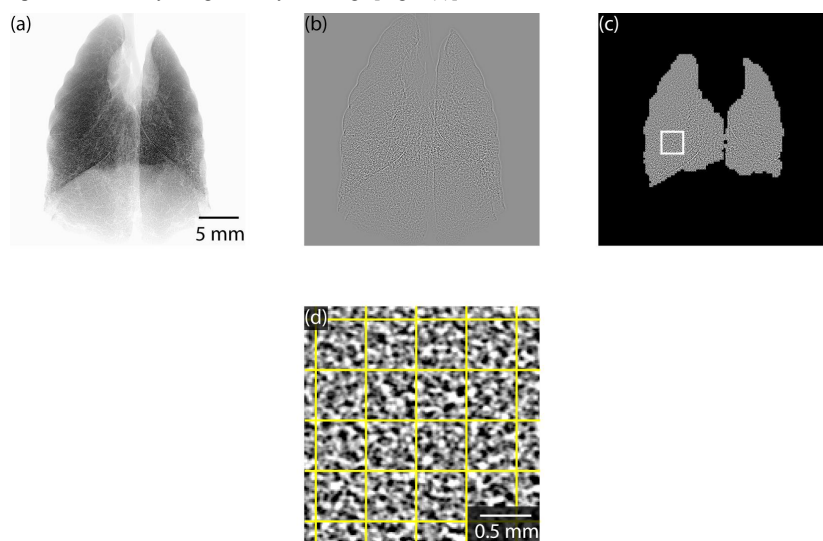


Figure 2. A re-projected image of a rabbit pup's lungs (a), which was previously segmented from CT data. The lung speckle is enhanced by a high pass filter (b) and after applying a grid, the densest areas of the lungs are selected by a mask (c). The speckled appearance and grid, corresponding to the area highlighted in (c) can be more clearly visualized in the magnified view (d).

An unmodified X-ray image [Fig. 3(a)], from the set of 1800 CT projections, at an angle corresponding with the re-projected image in Fig. 2(a) was also used for analysis.

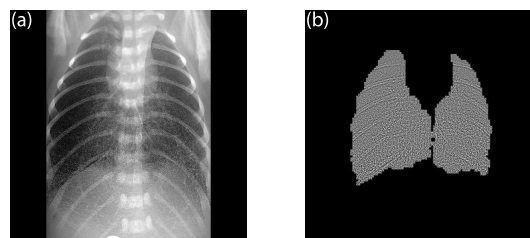


Figure 3. A single shot x-ray image of a rabbit pup's chest (a) and the lung speckle retrieved after masking and application of a high pass filter (b).

In both cases, the images were overlaid with a grid of windows (32×32 pixels with 50 per cent overlap) [Fig. 2(d)]. Windows were selected for analysis if their mean intensity was below a value, which was adjusted manually to obtain good coverage of the thicker (in projection) areas of the lungs [Figs. 2(c) and 3(b)]. A second order Butterworth high-pass filter (cutoff frequency: $1/32 \text{ px}^{-1}$) was then applied to enhance the lung speckle [Figs. 2(b,c) and 3(b)]. The

ensemble average of the two-dimensional SAF functions of all the windows was calculated before radially averaging to obtain the final one-dimensional SAF.

The radially averaged SAF is passed as an input to the solver. Detailed explanations of the following parameters related to the solver can be found elsewhere¹². The solver was run with a population size of 20. The parameter limits were: for the geometric mean diameter, 120 to 240 μm ; for the geometric standard deviation, 1.01 to 1.5; for the Gaussian point spread function, 6 to 30 μm and for the porosity, 0.3 to 0.55. The mutation distribution was one fifth of each parameter range and the mutation frequency was 20 per cent. Convergence was defined as the mean slope of the cost function for the previous 10 iterations reaching zero. The solver was run a total of 10 times and the solution with the lowest cost ultimately selected as the final solution.

4. RESULTS AND DISCUSSION

We begin by re-presenting previously published results to demonstrate the accuracy of our method when applied to non-penetrating spherical grains or pores. Good agreement can be observed between the nominal sizes of the glass microspheres and the distributions measured using our technique (Fig. 4).

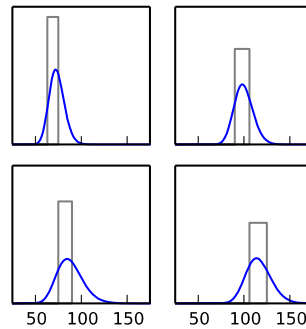


Figure 4. From a previous study, the probability density functions of glass microsphere diameters (in micrometres) measured using the same technique described here. The top-hat shaped distributions correspond with the nominal microsphere sizes and the other, lognormal distributions, with the results of our analysis.

The distribution of alveolar diameters was first measured from the re-projected lung image [Fig. 2(c)] and is presented in Fig. 5(a). The geometric mean diameter was 172 μm and the geometric standard deviation 1.26 (the arithmetic mean was 180 μm , and the arithmetic standard deviation 38.4 μm).

In terms of performance of the solver there is good agreement between the SAF of the lung speckle and that produced by the model in the region of the second trough [Figs. 5(b,c)]. Beyond this region, particularly at the head of the SAF, the two functions diverge considerably. As discussed previously, we attribute this behaviour to the presence of structures other than the alveoli.

Returning to the measured distribution, we were unable to find data in the literature for these parameters for a comparable animal but the diameters appear reasonable compared to those often cited for larger adult animals¹⁶. However, we can easily make a rough visual comparison between our measurements and the alveoli seen in a typical slice from our high-resolution CT reconstruction (Fig. 6). To the eye there is good agreement between illustrations of the sizes of representative alveoli at each quartile of the measured distribution and the alveoli observable in the CT image.

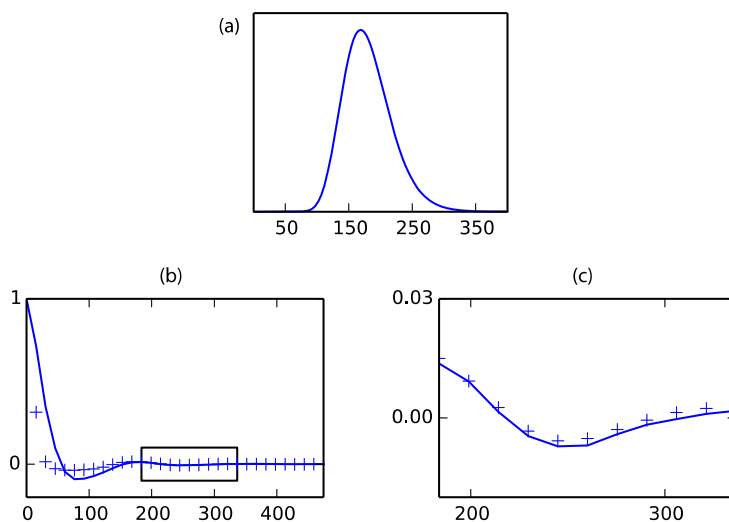


Figure 5. The distribution of small airway diameters (a) measured from a re-projected lung image. In (b), the spatial autocorrelation function of the re-projected lung image is depicted by the solid line, in comparison to the autocorrelation function of the proposed solution (cross hairs). A magnified view (c) of the region highlighted in (b) shows agreement between the two functions in our region of interest (the second trough). Units on the horizontal axes are micrometres.

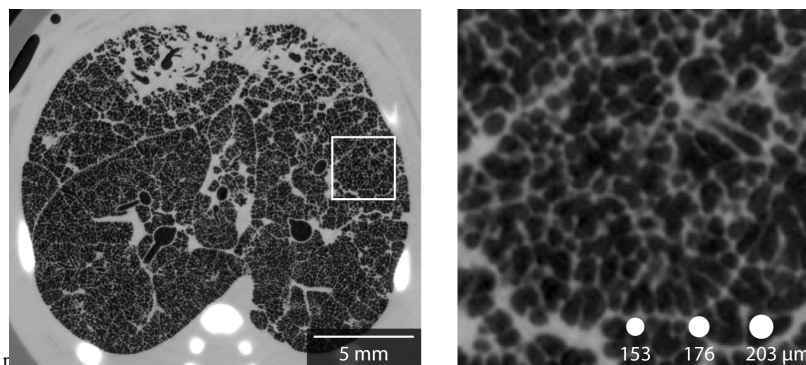


Figure 6. A computed tomography slice of a rabbit pup's lungs with a magnified view of the highlighted region on the right. In the magnified image are illustrations of alveoli corresponding with the 25th, 50th and 75th percentiles of alveolar diameters, corresponding with the distribution measured in Fig. 5(c).

Next, we present the distribution of alveolar diameters measured from the chest X-ray image [Fig. 3(a)] in Fig. 7. This distribution matches the distribution measured from the re-projected lung reasonably well and demonstrates that we can measure the distribution of alveolar diameters from a single, phase contrast, chest X-ray image with only a 40 ms exposure time. This potentially translates to dynamic imaging at 25 frames per second or faster.

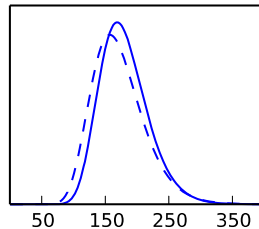


Figure 7. A comparison of the measured distribution of alveolar diameters (in micrometres) recovered from the re-projected (solid line) and single shot (dashed line) images.

There were a number of limitations in this study. Firstly, we acknowledge the need for further and more thorough validation of the technique. Comparison against objective, quantitative analysis of CT data is one obvious approach. A further limitation was the use of immature animal lungs, which was simply a matter of expediency. Further studies using adult lungs are required. The technique could also be improved by development of a more realistic (and likely more complex) lung model, which could allow the solver to make use of the entire SAF. This could potentially improve both the accuracy and robustness of the technique.

5. CONCLUSIONS

We have demonstrated a method for measuring the distribution of alveolar diameters from a single, phase contrast X-ray image. These measurements, performed on a chest X-ray of a rabbit pup, show good agreement with high-resolution computed tomography images of the same animal's lungs. The ability to perform the analysis on images with millisecond exposure times and with minimal radiation dose demonstrates the possibility of dynamic, *in vivo* measurements. Potential applications for the technique include disease detection, assessment of therapeutics and physiological studies.

REFERENCES

- [1] Wang, C., Altes, T. A., Mugler, J. P., Miller, G. W., Ruppert, K., Mata, J. F., Cates, G. D., Borish, L. and de Lange, E. E., "Assessment of the lung microstructure in patients with asthma using hyperpolarized ^3He diffusion MRI at two time scales: Comparison with healthy subjects and patients with COPD," *J. Magn. Reson. Imaging* 28(1), 80–88 (2008).
- [2] Carney, D. E., Bredenberg, C. E., Schiller, H. J., Picone, A. L., McCann, U. G., Gatto, L. A., Bailey, G., Fillinger, M. and Nieman, G. F., "The mechanism of lung volume change during mechanical ventilation," *Am. J. Resp. Crit. Care* 160(5), 1697–1702 (1999).
- [3] Hajari, A. J., Yablonskiy, D. A., Sukstanskii, A. L., Quirk, J. D., Conradi, M. S. and Woods, J. C., "Morphometric changes in the human pulmonary acinus during inflation," *J. Appl. Physiol.* 112(6), 937–943 (2012).
- [4] Saam, B. T., Yablonskiy, D. A., Kodibagkar, V. D., Leawoods, J. C., Gierada, D. S., Cooper, J. D., Lefrak, S. S. and Conradi, M. S., "MR imaging of diffusion of ^3He gas in healthy and diseased lungs," *Magn. Reson. Med.* 44(2), 174–179 (2000).
- [5] Yablonskiy, D. A., Sukstanskii, A. L., Leawoods, J. C., Gierada, D. S., Bretthorst, G. L., Lefrak, S. S., Cooper, J. D. and Conradi, M. S., "Quantitative *in vivo* assessment of lung microstructure at the alveolar level with hyperpolarized ^3He diffusion MRI," *PNAS* 99(5), 3111–3116 (2002).
- [6] Mokso, R., Marone, F., Haberthür, D., Schittny, J. C., Mikuljan, G., Isenegger, A. and Stampanoni, M., "Following dynamic processes by X-ray tomographic microscopy with sub-second temporal resolution," in *AIP Conference Proceedings* 1365, 38–41 (2011).

- [7] Dubsy, S., Hooper, S. B., Siu, K. K. W. and Fouras, A., "Synchrotron-based dynamic computed tomography of tissue motion for regional lung function measurement," *J. Royal Soc. Interface* 9(74), 2213–2224 (2012).
- [8] Fouras, A., Kitchen, M. J., Dubsy, S., Lewis, R. A., Hooper, S. B. and Hourigan, K., "The past, present, and future of x-ray technology for in vivo imaging of function and form," *J. Appl. Phys.* 105(10), 102009 (2009).
- [9] Kitchen, M. J., Paganin, D., Lewis, R. A., Yagi, N., Uesugi, K. and Mudie, S. T., "On the origin of speckle in X-ray phase contrast images of lung tissue," *Phys. Med. Biol.* 49, 4335–4348 (2004).
- [10] Dubsy, S., Jamison, R. A., Irvine, S. C., Siu, K. K. W., Hourigan, K. and Fouras, A., "Computed tomographic X-ray velocimetry," *Appl. Phys. Lett.* 96(2), 023702–023702–3 (2010).
- [11] Fouras, A., Allison, B. J., Kitchen, M. J., Dubsy, S., Nguyen, J., Hourigan, K., Siu, K. K. W., Lewis, R. A., Wallace, M. J., et al., "Altered lung motion is a sensitive indicator of regional lung disease," *Ann. Biomed. Eng.* 40(5), 1160–1169 (2012).
- [12] Carnibella, R. P., Kitchen, M. J. and Fouras, A., "Decoding the structure of granular and porous materials from speckled phase contrast X-ray images," *Opt. Express* 21(16), 19153–19162 (2013).
- [13] Kloss, C., Goniva, C., Hager, A., Amberger, S. and Pirker, S., "Models, algorithms and validation for opensource DEM and CFD–DEM," *Prog. Comput. Fluid Dy.* 12(2), 140–152 (2012).
- [14] Goto, S., Takeshita, K., Suzuki, Y., Ohashi, H., Asano, Y., Kimura, H., Matsushita, T., Yagi, N., Isshiki, M., et al., "Construction and commissioning of a 215-m-long beamline at SPring-8," *Nucl. Instrum. Meth. A* 467–468, 682–685 (2001).
- [15] Uesugi, K., Hoshino, M. and Yagi, N., "Comparison of lens- and fiber-coupled CCD detectors for X-ray computed tomography," *J. Synchrotron Radiat.* 18(2), 217–223 (2010).
- [16] Hyde, D. M., Tyler, N. K., Putney, L. F., Singh, P. and Gundersen, H. J. G., "Total number and mean size of alveoli in mammalian lung estimated using fractionator sampling and unbiased estimates of the Euler characteristic of alveolar openings," *Anat. Rec. Part A* 277A(1), 216–226 (2004).

6 Measuring dynamic alveolar function

6.1 Introduction

In the previous chapter a new single-shot X-ray technique for measuring the distribution of alveolar size in the lungs was presented. The two obvious extensions of this technique: measuring the change in alveolar size over the duration of a breath, and measuring the alveolar size in different regions of the lungs, are both addressed in this chapter.

In this chapter experimental results obtained from real-time, high resolution, in vivo imaging of breathing rabbit pup lungs are presented demonstrating the capability to observe and quantify the change in alveolar size over the respiratory cycle. These results are used to derive estimates of the total number of alveoli in the lungs, which in turn can be compared to previously published values as one means of indirect validation. Finally, capturing and visualising regional measurements of alveolar size is explored.

6.1.1 *A Direct Autocorrelation-Based Measurement Technique*

The previous chapter was concerned with the analysis of a static, single-shot, chest X-ray image. The next step is to consider a series of images taken over the duration of each breath. The short exposure times necessary to perform high frame rate imaging of this type of dynamic process are readily achievable using high sensitivity X-ray detectors with bright synchrotron X-rays sources. In addition to achieving significantly higher temporal resolution than is possible using computed tomography, the radiation dose is also significantly lower.

It would appear then that besides the challenges of high speed imaging, the extension of X-ray speckle-based alveolar sizing to a dynamic sequence of X-rays images would be straightforward. However, this isn't the case because the change in alveolar size during respiration is so small that the technique simply lacks the sensitivity to measure it (this will be evident shortly).

An alternative technique, a variation of the solver-based technique described in the previous chapter, based on the direct interpretation of the spatial autocorrelation function of particle generated speckle, presents a solution.

So far, the spatial autocorrelation function has been used as a simple, compact statistic for describing the speckle produced by grains or pores. As such, it is a convenient tool for comparing speckle patterns and, in this work, for generating a fit or cost function for an inverse method. Using this approach it is possible to solve for the morphological properties of granular and porous materials based on their

speckle patterns.

The presence of oscillations in the autocorrelation function of densely packed systems of particles (as can be seen in Figure 6.1) was discussed previously. However, the fact that these oscillations correspond, either directly or otherwise, to the ordering or structure of the underlying material has only been touched on in passing (section 3.1). The obvious question is whether any useful information about the system or material being studied can be obtained directly from the contours of these autocorrelation functions. This question was investigated using simulated projection images of packed particles.

One may recall that the packed particle model used previously is based on a lognormal distribution of sphere sizes. The three parameters that fully describe this model are the geometric mean (GM) and geometric standard deviation (GSD) of the distribution of sphere diameters and the its packing fraction or porosity. For reference, the basic properties of the lognormal distribution can be found in Appendix A.1.

To study the effect of each on the autocorrelation function a baseline distribution was nominated (geometric mean = 150 μm , GSD = 1.2 and porosity = 0.5) and the effect of varying the diameter for a range of geometric standard deviations and porosities was tested. Autocorrelation functions were generated by simulating phase contrast X-ray imaging of simple synthetic volumes of spherical particles using the same method outlined in section 3.1. Each cubic volume, $2 \times 2 \times 2 \text{ mm}^3$, was randomly packed with non penetrating spheres. The propagation-based phase contrast parameters were chosen to match those used later for small animal imaging (X-ray energy = 24 keV, propagation distance = 2 m and effective pixel size = 15.3 μm).

The positions of the first zero crossing and the first peak of the autocorrelation function (these locations are highlighted in Figure 6.1) were determined for a range of diameters, standard deviations and porosities. These results are presented in Figures 6.2 and 6.3.

In Figure 6.2 we see that for a constant GSD there is a linear relationship between the position of the geometric mean and both the position of the first zero crossing and the first peak. And in Figure 6.3 we see that the GSD has minimal, if any, effect on both the position of the first zero crossing and first peak. In both scenarios note the near one-to-one relationship between the the geometric mean diameter and the position of the first peak.

From these results we see that the position of the first peak provides a reasonable estimate of the geometric mean diameter. Furthermore, the gradient of the linear relationship between these two parameters is near unity, independent of either the geometric standard deviation or porosity. This relationship can be expressed as

$$\Delta\text{GM} = \Delta\text{Peak}_1 \quad (6.1)$$

A number of functions directly relating the zero and peak positions to the mean

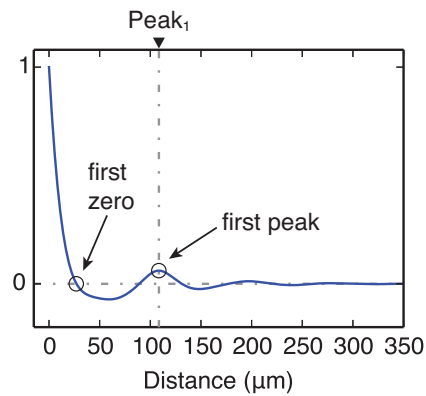


Figure 6.1: Spatial autocorrelation function of simulated X-ray image of spherical particles (particle diameters followed a lognormal distribution with geometric mean = $100\ \mu\text{m}$, GSD = 1.1 and porosity = 0.5). The positions of the first zero and the peak of the first oscillation have been highlighted.

diameter could also be derived from these results, but would be dependant on the porosity and GSD. The advantage of the simple relationship in equation 6.1 is that the change in diameter, of particular interest for dynamic measurements, can be easily obtained directly from the autocorrelation function. On the other hand, using multiple autocorrelation landmarks to make these measurements could be a means of reducing measurement error and increasing sensitivity.

The problem of dynamic lung imaging and dynamic measurement of the alveoli in the breathing lung is now revisited with a new tool for estimating alveolar size (though not the size distribution) directly from the spatial autocorrelation function of X-ray lung speckle.

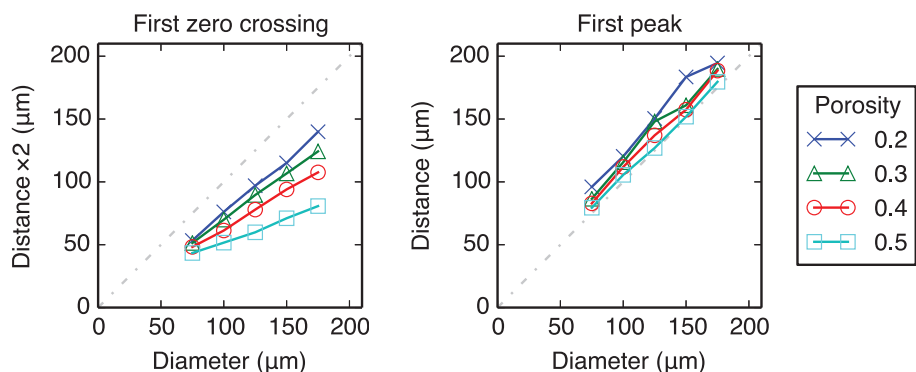


Figure 6.2: Position of first zero crossing (left) and first peak (right) vs geometric mean radius for a range of porosities. GSD = 1.25.

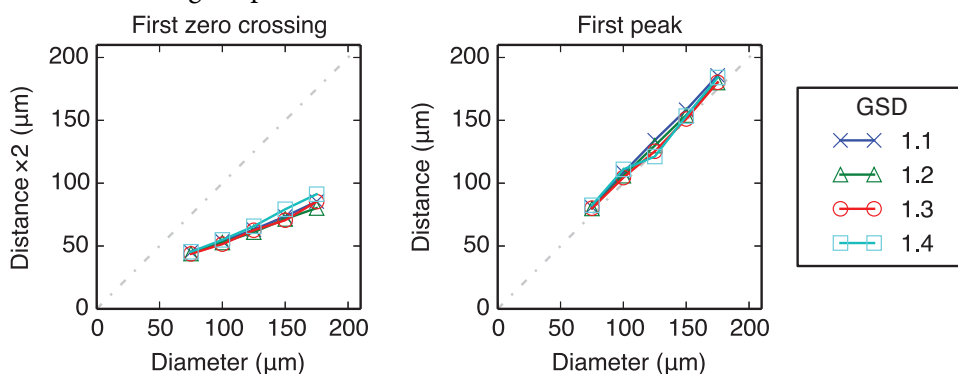


Figure 6.3: Position of first zero crossing (left) and first peak (right) vs geometric mean diameter for a range of GSDs. Porosity = 0.5.

6.2 Measuring the Dynamic Behaviour of Alveoli

Dynamic imaging and subsequent analysis was performed on rabbit pups, as in section 5.2. All experiments were approved by the Monash University Animal Ethics Committee and the SPring-8 Animal Care and Use Committee (Japan). These animals were controls for a separate experiment and no additional procedures were carried out for the purposes of the work outlined here.

Pups were delivered at 30 days of gestation (near-term) by caesarean section. An endotracheal tube was inserted via tracheostomy and the pups were ventilated for several minutes to clear their lungs of fluid.

Propagation-based phase contrast X-ray imaging was performed on beamline BL20B2 at the SPring-8 synchrotron (Goto et al., 2001). The propagation distance between the sample and detector was 2 m. A monochromatic X-ray source with an energy of 24 keV was used.

The pups were mechanically ventilated at a respiratory rate of 60 breaths per minute

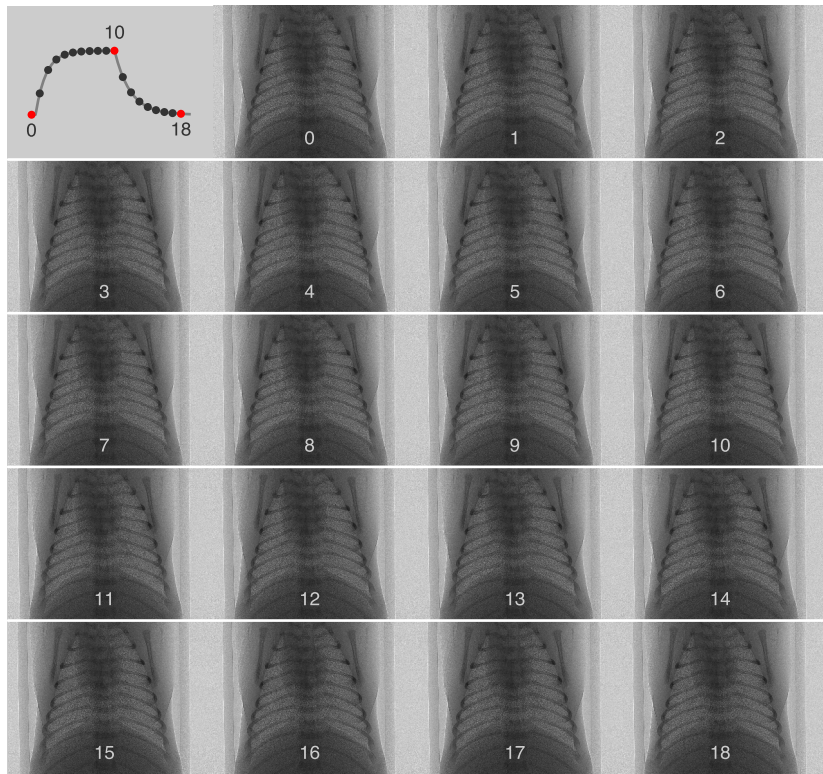


Figure 6.4: A sequence of chest X-ray images of a newborn rabbit pup: 19 projection images were captured over the course of a one second ventilation cycle. The respiratory motion can be observed in video format: <https://vimeo.com/172196119>

(equal duration inspiratory and expiratory phases of 0.5 s). Images were captured using a lens-coupled scintillator and pco.edge sCMOS camera, with image acquisition synchronised to the ventilator's timing. The image exposure time was 10 ms and the imaging rate was 19 frames per second. The combination of ventilation and imaging rates produced 19 imaging time points per breath. Images over multiple breaths were recorded with the animal in a front facing orientation. An Image sequence of a single breath can be seen in Figure 6.4. A trace of the tidal volume (the total volume of air inspired during a normal breath), measured by a pneumotach device, was recorded simultaneously.

Image processing was performed as described in section 5.2 except that spatial frequency filtering was performed with a second order Butterworth band-pass filter (cutoff frequencies: 1/32 and 1/5 cycles per pixel). The additional low pass component of the filter serving to attenuate high frequency image noise and subsequently improve analysis performance.

The position of the first peak of the autocorrelation function was calculated (by cubic interpolation) at each frame of the ventilation cycle. Assuming the peak posi-

tion is independent of the GSD and the porosity, which we saw to be the case to a good approximation, equation 6.1 was used to calculate the change in alveolar diameter by measuring the displacement of the first peak in each frame relative to frame zero (end-expiration). The alveolar size: geometric mean diameter and volume (volume was calculated assuming spherical alveoli), is plotted below the measured tidal volume trace in Figure 6.5.

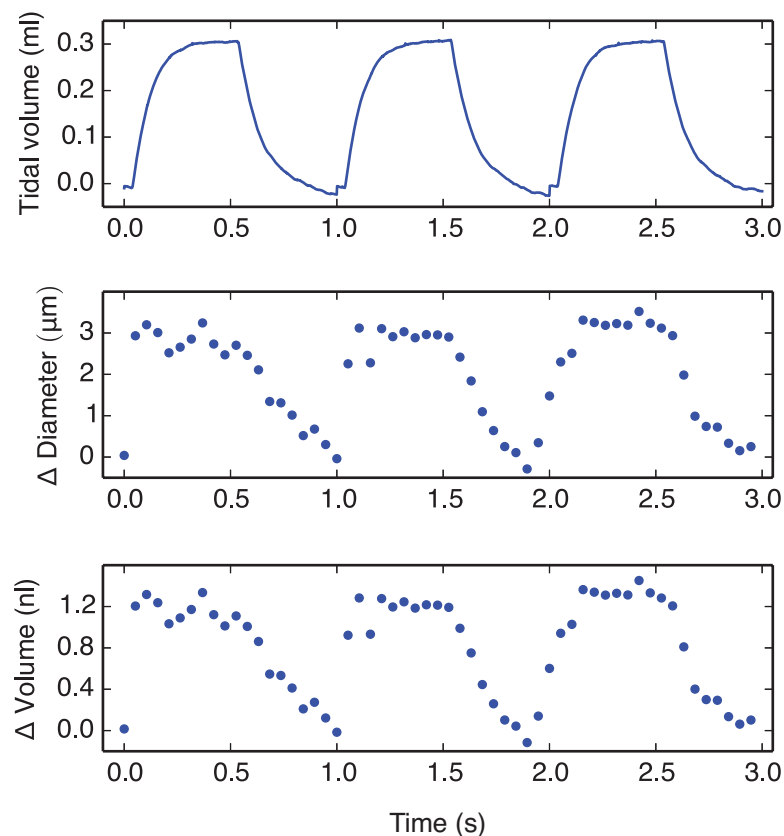


Figure 6.5: Below the tidal volume measured by a pneumotach device are the corresponding changes in geometric mean alveolar diameter and volume obtained by tracking the displacement of the first autocorrelation peak.

In Figure 6.5 we see that the change in alveolar diameter over a breath is about $3\ \mu\text{m}$ (2% increase) and the change in volume, the alveolar tidal volume, is around $1.3\ \text{nL}$ (6.1% increase). Note that the technique is making measurements with sub-pixel accuracy: $3\ \mu\text{m}$ is less than the $15.3\ \mu\text{m}$ effective pixel size of the imaging system.

The fact that it has proven necessary to measure with sup-pixel resolution goes to explaining why the sensitivity of the solver-based technique was an issue and the subsequent need for an alternative approach.

6.3 Estimating the total number of alveoli

So far the focus has been on measurements of alveolar diameter and volume. The problem of estimating the total number of alveoli in the lungs is now considered, making use of all the information now at hand. This information includes measurements of alveolar tidal volume, tidal volume measured by a pneumotach device and total lung capacity estimated from a high resolution CT scan.

The ability to estimate alveolar number in vivo is of value for investigating both physiological and pathological lung mechanics. Additionally, here, comparing these numbers to those documented in the literature serves to provide some validation of the technique.

6.3.1 Theory

Estimating the number of alveoli from the alveolar distribution

Assuming spherical alveoli, functional residual capacity (FRC) can be expressed as

$$\text{FRC} = N \int V(r) \cdot \text{PDF}(r) dr + V_{\text{DS}}$$

where N is the total number of alveoli and $V(r)$ is alveolar volume as a function of alveolar radius, $\text{PDF}(r)$ is the probability density function describing the number weighted distribution of alveolar radii and V_{DS} is the total dead space volume.

Simple rearrangement gives the number of alveoli:

$$N = \frac{\text{FRC} - V_{\text{DS}}}{\int V(r) \cdot \text{PDF}(r) dr} \quad (6.2)$$

Estimating the number of alveoli using the alveolar tidal volume

Having obtained the number of alveoli at end-expiration (N_0) using equation 6.2, the number of alveoli at end-inspiration (N_1) can be estimated using the alveolar tidal volume measured from imaging (Figure 6.5). The difference in the number of alveoli between end-expiration and end-inspiration represents the degree of alveolar recruitment. The relationship between all the relevant variables is given by

$$V_t = N_1 \int V(r) \cdot \text{PDF}_1(r) dr - N_0 \int V(r) \cdot \text{PDF}_0(r) dr + \Delta V_{\text{DS}}$$

where V_t is the global tidal volume, PDF_0 and PDF_1 are the number weighted distributions at end-expiration and end-inspiration, respectively, and ΔV_{DS} is the change in dead space volume.

Assuming that the standard deviation of the distribution doesn't change ($\sigma = \sigma_0 = \sigma_1$), the number of alveolar at end-expiration is given by

$$N_1 = \frac{V_t + N_0 \int V(r) \cdot \text{PDF}_0(r) \, dr}{\int V(r) \cdot \text{PDF}_1(r) \, dr} \quad (6.3)$$

6.3.2 Method

In addition to the dynamic imaging described in section 6.2, a high resolution chest CT of a rabbit pup was performed to estimate the functional residual lung capacity. Imaging at end-expiration was performed by gating to the ventilator. 450 images were taken over a 180° range of projection angles by rotating the sample stage. Otherwise all imaging parameters were the same as in section 6.2. CT reconstruction was performed by filtered back projection. The lung parenchyma and airways were segmented using a flood fill tool in Avizo 3D software (Figure 6.6). FRC was estimated by determining the volume of air within the segmented airspaces, where the volume of air for voxel ijk is

$$V_{ijk} = \frac{\text{CT}_{ijk}}{\text{CT}_{\text{air}}} V_{\text{voxel}}$$

where CT_{ijk} is the CT number (in Hounsfield units) of voxel ijk , CT_{air} is the CT number of air and V_{voxel} is the total volume of each voxel.

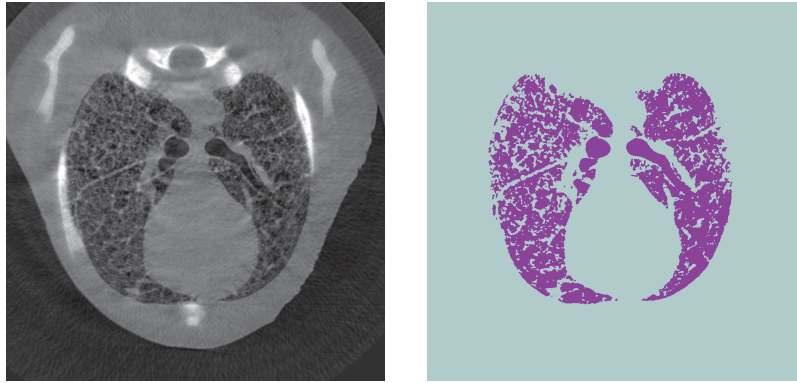


Figure 6.6: For illustrative purposes, segmented lung parenchyma (right) alongside the corresponding CT slice (left).

A single frame image, coinciding with the end of expiration, was also analysed employing the static X-ray speckle analysis technique used in section 5.5 to estimate the end-expiratory distribution of alveolar sizes.

6.3.3 Results/Discussion

The distribution of alveolar diameters obtained is shown in Figure 6.7. Note that until this point distributions have been volume weighted distributions, which is sensible given we are interested in the volume of air that is displaced during ventilation. The number weighted distribution is also shown, which is needed to obtain an estimate of the total number of alveoli as per equation 6.2.

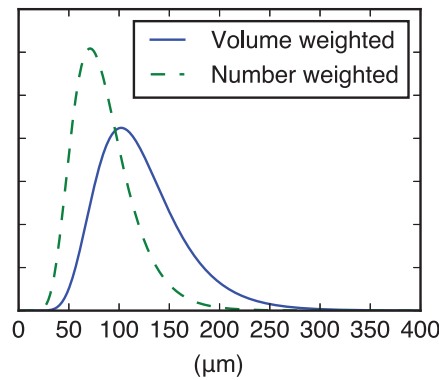


Figure 6.7: Volume and number weighted distributions (probability density) of alveolar diameters at end expiration obtained by lung X-ray speckle analysis. The solver's fitted, normalised autocorrelation function had a standard error of regression of 0.019.

All the relevant parameters required for calculating the total number of alveoli using both the methods outlined in the previous section, via equations 6.2 and 6.3 are given in Table 6.1. The dead space volume required for equation 6.2 was estimated as 26 percent of the tidal volume (Fowler, 1948).

Table 6.1: Parameters related to calculation of number of alveoli based on tidal volume. (*for number-based distribution.)

Functional residual capacity	1.38 ml
Tidal volume	0.3 ml
Dead space volume	0.078 ml
Alveolar diameter* (geometric mean, end expiration)	80.8 μm
Tidal change in alveolar diameter*	2.29 μm
Alveolar diameter GSD	1.41 μm

Finally, estimates of the number of alveoli in the lungs based on the alveolar distribution and the degree of alveolar recruitment are given in Table 6.2. These are compared to stereological measurements of histological sections made by Kovar et

al. (2002) and estimates of recruitment obtained by microscopy (Carney et al., 1999) and hyperpolarised MRI (Hajari et al., 2012).

Table 6.2: Estimates of number of alveoli

Based on end-expiratory alveolar distribution	2.8×10^6
Kovar et al. (2002)	2.8×10^6

Table 6.3: Estimates of tidal alveolar recruitment

Based on alveolar tidal volume	7.6%
Hajari et al. (2012, human)	14%
Carney et al. (1999, canine)	162%

Kovar et al. (2002) studied postnatal development of alveoli in rabbits and their estimate for the number of alveoli at term matches that obtained from the alveolar distribution measured by autocorrelation-based analysis.

Based on the ventilation strategy (tidal volume of 0.3 ml) and the change in alveolar diameter/volume obtained directly from the autocorrelation function during respiration, the number of alveoli recruited was estimated to be 211,000, which corresponds to an increase in the number of alveoli of 7.6 percent. There are only a few studies in the literature that have attempted to quantify alveolar recruitment, none of which have been performed in term rabbit pups. The figures from studies provided for comparison in Table 6.3 are at best rough estimates based on interpolating the data provided in these studies. Both studies were of adult lungs in species other than rabbits. The huge variation in the results from these studies highlights the difficulty in measuring alveolar recruitment. Carney et al. (1999) used surgical microscopy to image and measure subpleural alveoli. Both the surgical technique and the restriction of only studying subpleural alveoli were significant limitations in this study. On the other hand Hajari et al. (2012) rely on a complex lung model in order to obtain physiological or anatomical, quantitative measurements from MRI diffusion data.

The results in this section serve as both validation of the alveolar measurements obtained via static and dynamic techniques and support the growing consensus of the significance of alveolar recruitment. Furthermore, the ability to quantify the degree of alveolar recruitment was demonstrated. Going forward, future studies can use this technique to explore the degree of alveolar recruitment across normal physiology (e.g. developmental physiology of the lungs) and disease.

6.4 Regional analysis

All the measurements obtained so far have been global measurements, in which averaging has been performed over the entire lung fields. Averaging reduces noise in the autocorrelation function, which is particularly helpful when trying to achieve accurate sub-pixel measurements. However, averaging over the entire lung also negates one of the key strengths of an imaging-based technique: spatial information.

This final section demonstrates how regional measurements can be obtained by employing a less aggressive averaging regime and sacrificing a small amount of temporal resolution.

6.4.1 Theory

This analysis is based on the same rabbit pup imaging dataset as the previous section. Only the analysis itself differs.

Recalling the grid of windows that divides the lung into regions for autocorrelation analysis (section 5.5, Figure 2d), limited spatial averaging can be achieved by applying Gaussian weighted averaging of each radially averaged spatial autocorrelation function and its neighbours. This is equivalent to Gaussian smoothing in the context of image processing. It should be emphasised that here it is the autocorrelation functions that are being averaged, not the local estimate of alveolar size or other similarly derived quantities. The degree of averaging or smoothing is determined by the standard deviation (σ) of the Gaussian kernel.

Additionally, by averaging over multiple breaths additional noise reduction can be achieved without further sacrificing spatial resolution. This process is particularly practical when the subject is mechanically ventilated, and the imaging is gated to the ventilation cycle, because there is minimal breath to breath variability. Gated imaging in the case of a free breathing subject is still possible but is more involved and not as effective.

6.4.2 Method

In this analysis the spatial autocorrelation function sampling windows were 32×32 px², with 16 pixel spacing between windows (i.e. 50 percent overlap between adjacent windows).

Gaussian weighted averaging of these autocorrelation functions was performed by convolution with a Gaussian kernel ($\sigma = 5$ windows).

Autocorrelation functions were also averaged at the same phase of the ventilation/respiratory cycle over a total of three breathes.

Regional diameter was obtained by adding the relative change in diameter, as deter-

mined by measuring the change in the first peak position, to the global end-expiratory GM diameter as follows:

$$GM(i, j, t) = GM_{\text{global}} + \left(\text{Peak}_1(i, j, 0) - \overline{\text{Peak}_1(i, j, 0)} \right) + \Delta\text{Peak}_1$$

for window i, j at time point t .

6.4.3 Results/Discussion

Measurements of regional alveolar diameter are presented in Figure 6.8 in the form of a sequence of images of the lung fields that have been coloured by alveolar (GM) diameter.

Interestingly, Figure 6.8 shows an obvious trend of increasing alveolar size in the lower regions of the lungs. This is somewhat counterintuitive as one might have expected to find the opposite due to increased fluid pressure in the lower regions of the lungs. That this finding could be attributable to the effect of lung thickness or the influence of larger conducting airways was considered but discounted. If lung thickness was influencing measurements, a pattern around the edges of the lungs, rather than the upper regions, would be expected. Similarly, the distribution of large airways (central; airway diameter decreases towards the lung peripheries) isn't consistent with the observed pattern of alveolar diameter.

Because the change in alveolar size during respiration is small, it is easier to visualise the regional changes in alveolar size by only observing the change in alveolar diameter over time. An added level of complexity arises here because, since the lung isn't stationary, a window at a fixed location at the start of the inspiration will not lie over the same area of the lung at the end of inspiration. To compensate for lung motion and ensure we are comparing the same region between time points, bulk two-dimensional lung motion was tracked using the cross-correlation of windows between time points to estimate their displacement. All windows were shifted according to this map of tissue displacement, relative to the first time point (start of the breath). The difference in the peak position between time point zero and time point n , corresponding to the tidal change in alveolar diameter, was calculated at each window. The result is a sequence of images presented in Figure 6.9.

In Figure 6.9 the distribution of alveolar expansion appears to be quite heterogeneous throughout the lungs. An area of contraction, or decreasing alveolar size, is also evident in the left lower lobe. The significance of this finding is unclear.

The primary aim of this section has been to demonstrate the capability to measure dynamic alveolar function at a regional level. Some unexplained findings that have arisen from the results obtained suggest that further investigation from a biological perspective, although outside the scope of this work, is warranted.

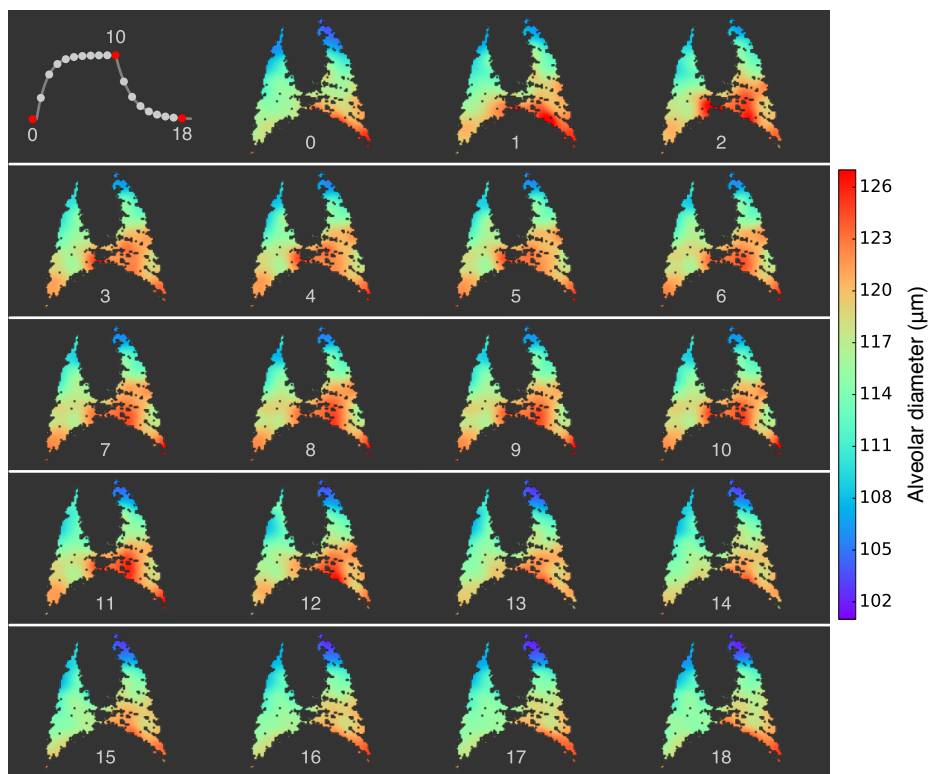


Figure 6.8: Sequence of lung images of a newborn rabbit pup over a complete ventilation cycle, coloured by geometric mean alveolar diameter.

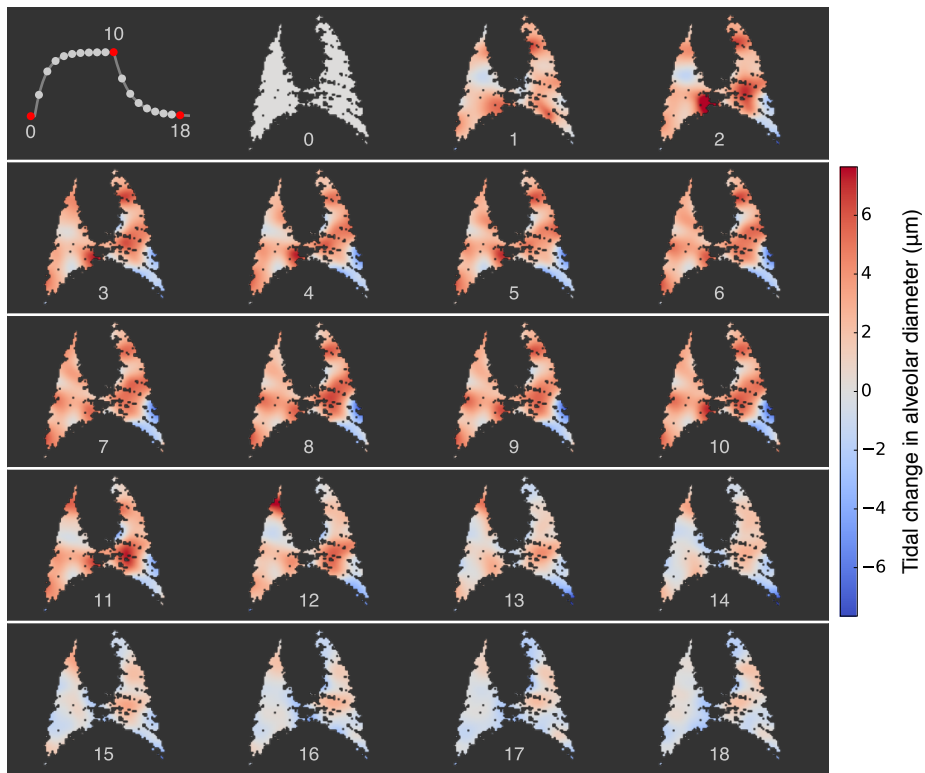


Figure 6.9: Sequence of lung images of a newborn rabbit pup over a complete ventilation cycle, coloured by change in geometric mean alveolar diameter (relative to the start of inspiration).

7 Conclusions

This thesis develops a suite of novel in vivo imaging techniques for studying the structure and dynamic behaviour of alveoli. It began with the development of the necessary theoretical background, then progressed to validation studies of a simple lung phantom before demonstrating the capability to perform in vivo lung imaging and analysis in small animal models. In this final chapter the most important outcomes of this research are presented and their significance highlighted before a brief discussion of the future directions for this work.

7.1 X-ray speckle

This thesis began with an examination of the nature of the speckle produced by granular and porous materials such as the lungs. It builds upon the research of Kitchen et al. (2004) and Cerbino et al. (2008), and advances the state of knowledge on this topic. Specifically, using phase contrast theory, it demonstrates how the speckled pattern produced by relatively large structures (tens to hundreds of micrometres), imaged with a coherent X-ray source, is directly related to the size of those structures. This relationship, which proved to be linear for loosely packed granular and porous materials, allows us to measure the size of grains and pores from a single X-ray projection image of a sample.

While the relationship between particles and the speckle pattern they produce is more complicated in the case of densely packed particle systems due to short range ordering, an inverse method for this problem was developed and used to accurately measure the distribution of the sphere sizes in a lung phantom consisting of a volume of packed glass microspheres.

An advantage of this technique, capable of measuring particles from a single projection image, compared to existing techniques such as computed tomography, is high temporal resolution. This allows us to study the behaviour of dynamic systems in real-time. Additionally, for biological specimens the reduction in radiation dose compared to computed tomography is significant. This technique, based on propagation-based phase contrast X-ray imaging, also has the advantage of having a relatively simple imaging protocol — in particular in comparison to techniques such as hyperpolarised MRI and nuclear medicine.

7.2 Functional alveolar imaging

At the very outset, the possibility of decoding the speckle produced by alveoli in phase contrast images of the lungs was presented as a novel and powerful means of measuring alveolar morphology. Building upon the methods developed and tested on microspheres, the same speckle analysis technique was applied to the analysis of X-ray lung speckle. Again, the key advantage of this method is its high temporal resolution, which makes it possible to study the dynamic mechanics of the alveoli during the respiratory cycle. The feasibility of measuring the dynamic behaviour of regional alveoli during tidal breathing was demonstrated. The applications of this technique range from basic physiological investigations of alveolar mechanics, to assessment of alveolar pathology related to diseases such as emphysema and bronchopulmonary dysplasia, and interventions such as mechanical ventilation. Of existing techniques, only diffusion weighted MRI has a similar capability but suffers from significant practical limitations including cost, accuracy and repeatability.

7.3 Bone suppression

When attempting to analyse the lung fields in a simple chest X-ray projection image, bones, particularly the ribs, can partially obscure a significant portion of the lungs. Dual energy X-ray imaging and material separation is a technique that can be used to remove or suppress the appearance of bones in such images. However, the synchrotron-based dual energy technique developed here is unique in that it allows true simultaneous dual energy imaging using a synchrotron light source. In this respect it is also superior to commercial dual energy scanners that sequentially acquire images at each energy. Beyond obtaining bone suppressed images for speckle-based alveolar measurement, it has applications for other dynamic synchrotron-based lung imaging techniques such as regional volume measurement (Kitchen et al., 2008).

7.4 Addendum

Between the end of their candidature and the completion of this thesis, the author contributed to another paper¹ (Appendix B.1) using a similar technique to measure lung structure, also in rabbit pup lungs. While that work is not included in its own chapter we will briefly look at it here.

The paper describes a technique of analysing near-field lung speckle based on spec-

¹Kitchen, M. J., Buckley, G. A., Leong, A. F. T., **Carnibella, R. P.**, Fouras, A., Wallace, M. J., Hooper, S. B., (2015). "X-ray specks: low dose in vivo imaging of lung structure and function". In: *Physics in Medicine and Biology* 60.18, pp. 7259–7276.

tral analysis of the speckle texture in Fourier space. It was shown that a peak in the power spectrum corresponds to, and can therefore be used to determine, the dominant length scale of the airways. In many respects this technique is very similar to that used in chapter 6, in which the secondary peak positions in the autocorrelation function were used to estimate the mean alveolar diameter. In fact, the power spectrum and autocorrelation are directly related by a single Fourier transform, as dictated by the Wiener-Khinchin theorem.

Using this technique, Kitchen et al. were able to study the developmental maturity of rabbit pup lungs at birth, discovering that there was significant variation between pups.

The major advantage of this technique is the simplicity of its implementation. However, the techniques previously presented in this thesis (i.e. the particle size distribution measurement) are not restricted to the near-field regime and are more powerful because they are capable of measuring the distribution of alveolar size.

7.5 Future work

In addition to the significant insights into measuring lung structure presented, due to the constraints inherent in a work of this type or simply because they were beyond the scope of this work, there are a number of unanswered questions, potential improvements and possible applications that merit future investigation.

In the process of modelling and simulating propagation-based phase contrast images of particles it was discovered, unexpectedly, that the Gaussian function that models the point spread function of the imaging system was dependent on the propagation distance. It was hypothesised that this may be the result of refraction within the volume of the sample, which is neglected when using a projected thickness approximation. Just prior to submission of this thesis it came to light that the effective source size of the synchrotron beamline may be larger than reported in the literature, which would increase the degree of penumbral blurring. This matter is currently being investigated on the beamline. Regardless of the cause, for the purpose of this work, it was possible to work around the issue using an empirically derived relationship between propagation distance and point spread function.

In terms of bone suppression, improving the performance of the dual energy technique presented could make it a practical tool for dynamic synchrotron imaging. More efficient scintillator-detector coupling and new technologies such as energy resolving detectors will drive developments in this area.

In chapter 6 we saw dynamic global and regional alveolar tidal volume measured in rabbit pup lungs. Measurement noise was an issue, although spatial and temporal averaging proved effective forms of noise reduction. Noise and associated errors arise from the fact that changes in size are being measured at sub-pixel resolution, and

for regional measurements from the requirement for ensemble averaging to obtain a low variance autocorrelation function. In the future, ongoing advances in X-ray detectors will produce detectors with increased sensitivity and higher spatial resolution. Advanced statistical and image processing techniques may also be able to improve the performance of autocorrelation-based analysis. This work will likely be driven by the applications of the technology.

The application of the technique in preclinical studies to study and provide insights into clinically relevant physiological processes and models of disease is the next step for this technology and the most important aspect of future work. Studies of early stage emphysema and mechanically induced lung injury are anticipated to follow.

7.6 Summary

The techniques developed in this thesis offer a new way of studying the dynamic behaviour of the alveoli in the breathing lung.

This work began by establishing the necessary theoretical groundwork; validation was performed using a simple lung phantom, methods of suppressing the effect of bone on image analysis were explored and, finally, the capability to measure alveolar size in vivo was demonstrated.

Future research will involve using the techniques developed here to gain new insights into clinically relevant physiological and pathological processes.

References

- Bajc, M., Neilly, B., Miniati, M., Mortensen, J., Jonson, B., (2010). "Methodology for ventilation/perfusion SPECT". In: *Seminars in Nuclear Medicine*. SPECT V/Q Imaging of the Lungs 40.6, pp. 415–425.
- Berger, M. J., Hubbell, J. H., Seltzer, S. M., Chang, J., Coursey, J. S., Sukumar, R., Zucker, D. S., Olsen, K., (2012). *XCOM: Photon cross sections Database*. XCOM: Photon Cross Section Database (version 1.5). URL: <http://www.nist.gov/pml/data/xcom.index.cfm> (visited on 03/06/2013).
- Berrington de González, A., Mahesh M. Kim K, et al, (2009). "Projected cancer risks from computed tomographic scans performed in the united states in 2007". In: *Archives of Internal Medicine* 169.22, pp. 2071–2077.
- Carney, D., Bredenberg, C., Schiller, H., Picone, A., McCann, U., Gatto, L., Bailey, G., Fillinger, M., Nieman, G., (1999). "The mechanism of lung volume change during mechanical ventilation". In: *American Journal of Respiratory and Critical Care Medicine* 160.5, pp. 1697–1702.
- Castillo, E., Castillo, R., Martinez, J., Shenoy, M., Guerrero, T., (2010). "Four-dimensional deformable image registration using trajectory modeling". In: *Physics in Medicine and Biology* 55.1, p. 305.
- Cerbino, R., Peverini, L., Potenza, M. A. C., Robert, A., Bosecke, P., Giglio, M., (2008). "X-ray-scattering information obtained from near-field speckle". In: *Nature Physics* 4.3, pp. 238–243.
- Cereda, M., Emami, K., Kadlecsek, S., Xin, Y., Mongkolwisetwara, P., Profka, H., Barulic, A., Pickup, S., Månsson, S., Wollmer, P., Ishii, M., Deutschman, C. S., Rizi, R. R., (2011). "Quantitative imaging of alveolar recruitment with hyperpolarized gas MRI during mechanical ventilation". In: *Journal of Applied Physiology* 110.2, pp. 499–511.
- Chapman, D., Thomlinson, W., Johnston, R. E., Washburn, D., Pisano, E., Gmür, N., Zhong, Z., Menk, R., Arfelli, F., Sayers, D., (1997). "Diffraction enhanced x-ray imaging". In: *Physics in Medicine and Biology* 42.11, p. 2015.
- Cheney, M., Isaacson, D., Newell, J. C., (1999). "Electrical impedance tomography". In: *SIAM review* 41.1, pp. 85–101.
- Chon, D., Simon, B. A., Beck, K. C., Shikata, H., Saba, O. I., Won, C., Hoffman, E. A., (2005). "Differences in regional wash-in and wash-out time constants for xenon-

- CT ventilation studies". In: *Respiratory Physiology & Neurobiology* 148.1, pp. 65–83.
- Crotti, S., Mascheroni, D., Caironi, P., Pelosi, P., Ronzoni, G., Mondino, M., Marini, J. J., Gattinoni, L., (2001). "Recruitment and derecruitment during acute respiratory failure: A clinical study". In: *American Journal of Respiratory and Critical Care Medicine* 164.1, pp. 131–140.
- Currey, J. D., (1988). "The effect of porosity and mineral content on the Young's modulus of elasticity of compact bone". In: *Journal of Biomechanics* 21.2, pp. 131–139.
- Danielson, R. E., Sutherland, P. L., (1986). "Porosity". In: *Methods of soil analysis. Part 1. Physical and mineralogical methods*. 2nd ed., pp. 443–461.
- Dubsky, S., Hooper, S. B., Siu, K. K. W., Fouras, A., (2011). "Dynamic four-dimensional X-ray PIV of the lung". In: *9th International Symposium on Particle Image Velocimetry-PIV*. Vol. 11, pp. 21–23.
- Dubsky, S., Hooper, S. B., Siu, K. K. W., Fouras, A., (2012). "Synchrotron-based dynamic computed tomography of tissue motion for regional lung function measurement". In: *Journal of the Royal Society Interface* 9.74, pp. 2213–2224.
- Ebert, M., Grossmann, T., Heil, W., Otten, E. W., Surkau, R., Thelen, M., Leduc, M., Bachert, P., Knopp, M. V., Schad, L. R., (1996). "Nuclear magnetic resonance imaging with hyperpolarised helium-3". In: *The Lancet* 347.9011, pp. 1297–1299.
- Fain, S., Schiebler, M. L., McCormack, D. G., Parraga, G., (2010). "Imaging of lung function using hyperpolarized helium-3 magnetic resonance imaging: Review of current and emerging translational methods and applications". In: *Journal of Magnetic Resonance Imaging* 32.6, pp. 1398–1408.
- Fan, M., Marks, L. B., Lind, P., Hollis, D., Woel, R. T., Bentel, G. G., Anscher, M. S., Shafman, T. D., Coleman, R. E., Jaszczak, R. J., (2001). "Relating radiation-induced regional lung injury to changes in pulmonary function tests". In: *International Journal of Radiation Oncology, Biology, Physics* 51.2, pp. 311–317.
- Ferri, F., Magatti, D., Pescini, D., Potenza, M. A. C., Giglio, M., (2004). "Heterodyne near-field scattering: A technique for complex fluids". In: *Physical Review E* 70.4, p. 041405.
- Fowler, W. S., (1948). "Lung function studies. II. The respiratory dead space". In: *American Journal of Physiology-Legacy Content* 154.3, pp. 405–416.
- Gattinoni, L., Caironi, P., Cressoni, M., Chiumello, D., Ranieri, V. M., Quintel, M., Russo, S., Patroniti, N., Cornejo, R., Bugedo, G., (2006). "Lung recruitment in pa-

- tients with the acute respiratory distress syndrome”. In: *New England Journal of Medicine* 354.17, pp. 1775–1786.
- Gierada, D. S., Woods, J. C., Bierhals, A. J., Bartel, S. T., Ritter, J. H., Choong, C. K., Das, N. A., Hong, C., Pilgram, T. K., Chang, Y. V., (2009). “Effects of diffusion time on short-range hyperpolarized ^3He diffusivity measurements in emphysema”. In: *Journal of Magnetic Resonance Imaging* 30.4, pp. 801–808.
- Giglio, M., Carpineti, M., Vailati, A., (2000). “Space intensity correlations in the near field of the scattered light: A direct measurement of the density correlation function $g(r)$ ”. In: *Physical Review Letters* 85.7, pp. 1416–1419.
- Goodman, J. W., (2006). *Speckle phenomena in optics*. 1st ed. Greenwood Village: Roberts and Company Publishers.
- Goto, S., Takeshita, K., Suzuki, Y., Ohashi, H., Asano, Y., Kimura, H., Matsushita, T., Yagi, N., Isshiki, M., Yamazaki, H., Yoneda, Y., Umetani, K., Ishikawa, T., (2001). “Construction and commissioning of a 215-m-long beamline at SPring-8”. In: *Nuclear Instruments and Methods in Physics Research Section A: Accelerators, Spectrometers, Detectors and Associated Equipment* 467-468, pp. 682–685.
- Guerrero, T., Sanders, K., Castillo, E., Zhang, Y., Bidaut, L., Pan, T., Komaki, R., (2006). “Dynamic ventilation imaging from four-dimensional computed tomography”. In: *Physics in Medicine and Biology* 51, p. 777.
- Hajari, A. J., Yablonskiy, D. A., Sukstanskii, A. L., Quirk, J. D., Conradi, M. S., Woods, J. C., (2012). “Morphometric changes in the human pulmonary acinus during inflation”. In: *Journal of Applied Physiology* 112.6, pp. 937–943.
- Harris, R. S., Schuster, D. P., (2007). “Visualizing lung function with positron emission tomography”. In: *Journal of Applied Physiology* 102.1, pp. 448–458.
- Holmes, J. H., O’Halloran, R. L., Brodsky, E. K., Jung, Y., Block, W. F., Fain, S. B., (2008). “3D hyperpolarized He-3 MRI of ventilation using a multi-echo projection acquisition”. In: *Magnetic Resonance in Medicine* 59.5, pp. 1062–1071.
- Jaeger, H. M., Nagel, S. R., Behringer, R. P., (1996). “Granular solids, liquids, and gases”. In: *Reviews of Modern Physics* 68.4, p. 1259.
- Jobe, A. H., Bancalari, E., (2001). “Bronchopulmonary dysplasia”. In: *American Journal of Respiratory and Critical Care Medicine* 163.7, pp. 1723–1729.
- Jobse, B. N., Rhem, R. G., McCurry, C. A., Wang, I. Q., Labiris, N. R., (2012). “Imaging lung function in mice using SPECT/CT and per-voxel analysis”. In: *PloS One* 7.8, e42187.

- Kitchen, M. J., Lewis, R. A., Morgan, M. J., Wallace, M. J., Siew, M. L., Siu, K. K. W., Habib, A., Fouras, A., Yagi, N., Uesugi, K., Hooper, S. B., (2008). "Dynamic measures of regional lung air volume using phase contrast x-ray imaging". In: *Physics in Medicine and Biology* 53, pp. 6065–6077.
- Kitchen, M. J., Lewis, R. A., Yagi, N., Uesugi, K., Paganin, D. M., Hooper, S. B., Adams, G., Jureczek, S., Singh, J., Christensen, C. R., (2005). "Phase contrast X-ray imaging of mice and rabbit lungs: A comparative study". In: *British Journal of Radiology*.
- Kitchen, M. J., Paganin, D. M., Lewis, R. A., Yagi, N., Uesugi, K., Mudie, S. T., (2004). "On the origin of speckle in X-ray phase contrast images of lung tissue". In: *Physics in Medicine and Biology* 49, pp. 4335–4348.
- Kovar, J., Sly, P. D., Willet, K. E., (2002). "Postnatal alveolar development of the rabbit". In: *Journal of Applied Physiology* 93.2, pp. 629–635.
- Kumar, R., Bhattacharjee, B., (2003). "Porosity, pore size distribution and in situ strength of concrete". In: *Cement and Concrete Research* 33.1, pp. 155–164.
- Lande, B., Mitzner, W., (2006). "Analysis of lung parenchyma as a parametric porous medium". In: *Journal of Applied Physiology* 101.3, pp. 926–933.
- Lewis, R. A., Yagi, N., Kitchen, M. J., Morgan, M. J., Paganin, D. M., Siu, K. K. W., Pavlov, K., Williams, I., Uesugi, K., Wallace, M. J., (2005). "Dynamic imaging of the lungs using x-ray phase contrast". In: *Physics in Medicine and Biology* 50, pp. 5031–5040.
- Lipson, A., Lipson, S. G., Lipson, H., (2010). *Optical physics*. 4th ed. Cambridge: Cambridge University Press.
- McKenzie, D. K., Abramson, M., Crockett, A. J., Glasgow, N., Jenkins, S., McDonald, C., Wood-Baker, R., Frith, P. A., (2010). *The COPD-X plan: Australian and New Zealand guidelines for the management of chronic obstructive pulmonary disease*. Milton: Lung Foundation Australia.
- Meinel, F. G., Yaroshenko, A., Hellbach, K., Bech, M., Müller, M., Velroyen, A., Bamberg, F., Eickelberg, O., Nikolaou, K., Reiser, M. F., Pfeiffer, F., Yildirim, A. Ö., (2014). "Improved diagnosis of pulmonary emphysema using in vivo dark-field radiography". In: *Investigative Radiology* 49.10, pp. 653–658.
- Mertens, M., Tabuchi, A., Meissner, S., Krueger, A., Schirrmann, K., Kertzsch, U., Pries, A. R., Slutsky, A. S., Koch, E., Kuebler, W. M., (2009). "Alveolar dynamics in acute lung injury: Heterogeneous distension rather than cyclic opening and collapse*." in: *Critical Care Medicine* 37.9, pp. 2604–2611.

- Mills, G. H., Wild, J. M., Eberle, B., Beek, E. J. R. V., (2003). "Functional magnetic resonance imaging of the lung". In: *British Journal of Anaesthesia* 91.1, pp. 16–30.
- Namati, E., Thiesse, J., Ryk, J., McLennan, G., (2008). "Alveolar Dynamics during Respiration". In: *American Journal of Respiratory Cell and Molecular Biology* 38.5, pp. 572–578.
- Nieto-Vesperinas, M., (2006). *Scattering and diffraction in physical optics*. 2nd ed. Singapore: World Scientific.
- Norberg, P., Persson, H. L., Schmekel, B., Carlsson, G. A., Wahlin, K., Sandborg, M., Gustafsson, A., (2014). "Does quantitative lung SPECT detect lung abnormalities earlier than lung function tests? Results of a pilot study". In: *EJNMMI Research* 4.1, pp. 1–12.
- Ochs, M., Nyengaard, J. R., Jung, A., Knudsen, L., Voigt, M., Wahlers, T., Richter, J., Gundersen, H. J. G., (2004). "The number of alveoli in the human lung". In: *American Journal of Respiratory and Critical Care Medicine* 169.1, pp. 120–124.
- Pan, T., Lee, T. Y., Rietzel, E., Chen, G. T., (2004). "4D-CT imaging of a volume influenced by respiratory motion on multi-slice CT". In: *Medical Physics* 31, p. 333.
- Parent, R. A., (2015). *Comparative biology of the normal lung*. Academic Press. 835 pp.
- Percus, J. K., Yevick, G. J., (1958). "Analysis of classical statistical mechanics by means of collective coordinates". In: *Physical Review* 110.1, p. 1.
- Pfeiffer, F., Kottler, C., Bunk, O., David, C., (2007). "Hard X-ray phase tomography with low-brilliance sources". In: *Physical Review Letters* 98.10, p. 108105.
- Pogany, A., Gao, D., Wilkins, S. W., (1997). "Contrast and resolution in imaging with a microfocus x-ray source". In: *Review of Scientific Instruments* 68, pp. 2774–2782.
- Reinhardt, J. M., Ding, K., Cao, K., Christensen, G. E., Hoffman, E. A., Bodas, S. V., (2008). "Registration-based estimates of local lung tissue expansion compared to xenon CT measures of specific ventilation". In: *Medical Image Analysis* 12.6, pp. 752–763.
- Rittayamai, N., Brochard, L., (2015). "Recent advances in mechanical ventilation in patients with acute respiratory distress syndrome". In: *European Respiratory Review* 24.135, pp. 132–140.
- Salerno, M., Altes, T. A., Brookeman, J. R., Lange, E. E., Mugler III, J. P., (2001). "Dynamic spiral MRI of pulmonary gas flow using hyperpolarized ^3He : Preliminary studies in healthy and diseased lungs". In: *Magnetic Resonance in Medicine* 46.4, pp. 667–677.

- Salerno, M., Lange, E. E., Altes, T. A., Truwit, J. D., Brookeman, J. R., Mugler III, J. P., (2002). “Emphysema: Hyperpolarized helium 3 diffusion MR imaging of the lungs compared with spirometric indexes—initial experience”. In: *Radiology* 222.1, p. 252.
- Samee, S., Altes, T., Powers, P., Lange, E. E., Knight-Scott, J., Rakes, G., Mugler III, J. P., Ciambotti, J. M., Alford, B. A., Brookeman, J. R., (2003). “Imaging the lungs in asthmatic patients by using hyperpolarized helium-3 magnetic resonance: assessment of response to methacholine and exercise challenge”. In: *Journal of Allergy and Clinical Immunology* 111.6, pp. 1205–1211.
- Schleede, S., Meinel, F. G., Bech, M., (2012). “Emphysema diagnosis using X-ray dark-field imaging at a laser-driven compact synchrotron light source”. In: *Proceedings of the National Academy of Sciences* 109.44, pp. 17880–17885.
- Simon, B. A., (2000). “Non-invasive imaging of regional lung function using x-ray computed tomography”. In: *Journal of Clinical Monitoring and Computing* 16.5, pp. 433–442.
- Snigirev, A., Snigireva, I., Kohn, V., Kuznetsov, S., Schelokov, I., (1995). “On the possibilities of x-ray phase contrast microimaging by coherent high-energy synchrotron radiation”. In: *Review of Scientific Instruments* 66.12, pp. 5486–5492.
- Song, C., Wang, P., Makse, H. A., (2008). “A phase diagram for jammed matter”. In: *Nature* 453.7195, pp. 629–632.
- Soriano, J. B., Zielinski, J., Price, D., (2009). “Screening for and early detection of chronic obstructive pulmonary disease”. In: *The Lancet* 374.9691, pp. 721–732.
- The ImpACT Group, (2009). *Comparative specifications: 128 to 320 slice CT scanner technical specifications*. CEP08028. London: Centre for Evidence-based Purchasing.
- Torquato, S., (2005). *Random heterogeneous materials: Microstructure and macroscopic properties*. Springer Science & Business Media.
- Viallon, M., Berthezène, Y., Callot, V., Bourgeois, M., Humblot, H., Briguet, A., Crémillieux, Y., (2000). “Dynamic imaging of hyperpolarized ^3He distribution in rat lungs using interleaved-spiral scans”. In: *NMR in Biomedicine* 13.4, pp. 207–213.
- Victorino, J. A., Borges, J. B., Okamoto, V. N., Matos, G. F., Tucci, M. R., Caraméz, M. P., Tanaka, H., Sipmann, F. S., Santos, D. C., Barbas, C. S., (2004). “Imbalances in regional lung ventilation: A validation study on electrical impedance tomography”. In: *American Journal of Respiratory and Critical Care Medicine* 169.7, pp. 791–800.
- Weibel, E. R., (1963). *Morphometry of the human lung*. New York: Academic Press.

- Wild, J. M., Paley, M. N., Kasuboski, L., Swift, A., FICHELE, S., Woodhouse, N., Griffiths, P. D., Beek, E. J., (2003). "Dynamic radial projection MRI of inhaled hyperpolarized ^3He gas". In: *Magnetic Resonance in Medicine* 49.6, pp. 991–997.
- Wilkins, S. W., Gureyev, T. E., Gao, D., Pogany, A., Stevenson, A. W., (1996). "Phase-contrast imaging using polychromatic hard X-rays". In: *Nature* 384.6607, pp. 335–338.
- Woods, J. C., Choong, C. K., Yablonskiy, D. A., Bentley, J., Wong, J., Pierce, J. A., Cooper, J. D., Macklem, P. T., Conradi, M. S., Hogg, J. C., (2006). "Hyperpolarized ^3He diffusion MRI and histology in pulmonary emphysema". In: *Magnetic Resonance in Medicine* 56.6, pp. 1293–1300.
- Yablonskiy, D. A., Sukstanskii, A. L., Leawoods, J. C., Gierada, D. S., Bretthorst, G. L., Lefrak, S. S., Cooper, J. D., Conradi, M. S., (2002). "Quantitative in vivo assessment of lung microstructure at the alveolar level with hyperpolarized ^3He diffusion MRI". In: *Proceedings of the National Academy of Sciences* 99.5, pp. 3111–3116.

A Appendix

A.1 The lognormal distribution

The lognormal distribution describes a probability distribution, the logarithm of which is a normal distribution, hence the name. Compared to the normal distribution it is skewed to the right. Another significant difference is that it starts at zero and therefore cannot be negative.

The lognormal probability density function is defined as

$$\text{PDF} = \frac{1}{x\sigma\sqrt{2\pi}} e^{-\frac{(\ln x - \mu)^2}{2\sigma^2}}$$

where μ is referred to as the location parameter, σ the scale parameter and x is the variable — in the context of this thesis that variable is the particle or alveolar diameter.

The location and scale parameters are related to the geometric mean, median and geometric standard deviation of the distribution:

$$\text{GM} = \text{median} = e^{\mu}$$

$$\text{GSD} = e^{\sigma}.$$

The arithmetic mean and standard deviation can be obtained via

$$M = e^{\mu + 0.5\sigma^2}$$

$$\text{SD} = M\sqrt{e^{\sigma^2} - 1}.$$

In the context of a distribution of particles, the distribution can be either volume or number weighted. A volume weighted distribution describes the fraction of the total volume that is composed of each particle diameter. This contrasts with a number weighted distribution that more intuitively describes the number of particles of each diameter. For a lognormal distribution, the relationship between the two weightings is

$$\mu_N = \mu_V - 3\sigma^2$$

where μ_N is the number weighted location parameter and μ_V the volume weighted location parameter.

B Appendix

B.1 Article - X-ray specks: low dose *in vivo* imaging of lung structure and function

IOP Publishing | Institute of Physics and Engineering in Medicine Physics in Medicine & Biology
Phys. Med. Biol. 60 (2015) 7259–7276 doi:10.1088/0031-9155/60/18/7259

X-ray specks: low dose *in vivo* imaging of lung structure and function

Marcus J Kitchen¹, Genevieve A Buckley¹,
Andrew F T Leong¹, Richard P Carnibella², Andreas Fouras²,
Megan J Wallace³ and Stuart B Hooper³

¹ School of Physics and Astronomy, Monash University, Clayton, Victoria, Australia

² Department of Mechanical and Aerospace Engineering, Monash University, Clayton, Victoria, Australia

³ The Ritchie Centre, Hudson Institute of Medical Research and the Department of Obstetrics and Gynaecology, Monash University, Clayton, Victoria, Australia

E-mail: Marcus.Kitchen@monash.edu

Received 9 July 2015

Accepted for publication 4 August 2015

Published 7 September 2015



CrossMark

Abstract

Respiratory health is directly linked to the structural and mechanical properties of the airways of the lungs. For studying respiratory development and pathology, the ability to quantitatively measure airway dimensions and changes in their size during respiration is highly desirable. Real-time imaging of the terminal airways with sufficient contrast and resolution during respiration is currently not possible. Herein we reveal a simple method for measuring lung airway dimensions in small animals during respiration from a single propagation-based phase contrast x-ray image, thereby requiring minimal radiation. This modality renders the lungs visible as a speckled intensity pattern. In the near-field regime, the size of the speckles is directly correlated with that of the dominant length scale of the airways. We demonstrate that Fourier space quantification of the speckle texture can be used to statistically measure regional airway dimensions at the alveolar scale, with measurement precision finer than the spatial resolution of the imaging system. Using this technique we discovered striking differences in developmental maturity in the lungs of rabbit kittens at birth.

Keywords: phase contrast, speckle, x-ray imaging, lung, airway dimensions

(Some figures may appear in colour only in the online journal)

1. Background

Pulmonary diseases are one of the greatest causes of human morbidity and mortality. Chronic obstructive pulmonary disease (COPD), the fifth leading cause of death in humans, occurs in 10% of the population and its incidence is rapidly increasing (Pauwels and Rabe 2004). COPD includes emphysema, chronic bronchitis and some cases of asthma. For newborn infants, respiratory failure is the greatest cause of morbidity and mortality, particularly for those born very preterm. Many of the surviving infants (~30%) develop bronchopulmonary dysplasia (BPD). BPD has major implications for the respiratory health of individuals throughout their lives (Jobe *et al* 2008). Forms of both COPD and BPD result in abnormal regional changes in airway structure. Our ability to reduce the burden of these diseases is impaired by our inability to image the lung with high resolution *in vivo*, particularly the small airways that harbour much of the pathology associated with these diseases. It is currently not possible to detect many forms of lung disease with imaging before they are clinically evident. High-resolution computed tomography (CT) is the gold standard technology commonly used for imaging COPD as it can resolve airway structures down to the 7th generation (Milne and King 2014). However, with a spatial resolution of around 0.5 mm, it is unable to resolve the smallest terminal airways (alveoli), which range in average size from 80–210 μm (Irvin and Bates 2003). This is true of all other clinical imaging modalities. Micro-CT is capable of resolving these structures (see e.g. Beltran *et al* (2011), Sera *et al* (2013)), however the radiation dose is prohibitively high and it is currently impossible to perform in real-time for *in vivo* human diagnostics (Milne and King 2014). Any technique capable of non-invasively measuring regional changes in minor airway structures *in vivo* could provide huge benefits for pre-clinical studies and diagnostic imaging (Milne and King 2014).

Propagation-based phase contrast x-ray imaging (PBI) is a very simple technique for obtaining high contrast images of weakly absorbing materials including soft tissues. It relies on Fresnel diffraction and requires a partially coherent x-ray source but no additional optics to render phase changes visible upon free-space propagation to a spatially resolving detector (Wilkins *et al* 1996). The airways of the lungs can be made highly visible with PBI due to the large differences in refractive index between soft tissue and air at diagnostic energies. In a 2D projection image, the many overlapping airways of the lungs create a speckled pattern of bright and dark spots resulting from interference effects (Yagi *et al* 1999, Suzuki *et al* 2002). Figure 1 shows the experimental configuration and a typical speckled image of the lungs. From a geometrical optics perspective, the lung tissue acts as an aberrated compound refractive lens causing local variations in focal volume that results in strong intensity variations (Kitchen *et al* 2004).

Speckle is commonly seen when coherent light is transmitted through or reflected from a random phase screen. In the laser community it has long been known that speckle encodes information about the scattering medium that created the speckle, and numerous methods have been developed to decode this information (Goodman 2000). When random media are imaged at sufficiently close distances to the object, speckles have approximately the same size as the scatterers that created them. This effect of ‘near-field speckle’ is independent of the number of scatterers in projection, the wavelength of radiation and the object-to-detector distance (ODD). However, in the far-field the speckle size grows with distance and the relation to the scatterer size is lost (Giglio *et al* 2000, Cerbino 2007). Various authors have given heuristic (Giglio *et al* 2000) and theoretical (Cerbino 2007) arguments as to why near-field speckle produces this simple relationship with the scatterer size.

Using x-rays, Cerbino *et al* (2008) showed that near-field speckle can provide statistical information about structural properties of colloidal samples. They obtained an order of

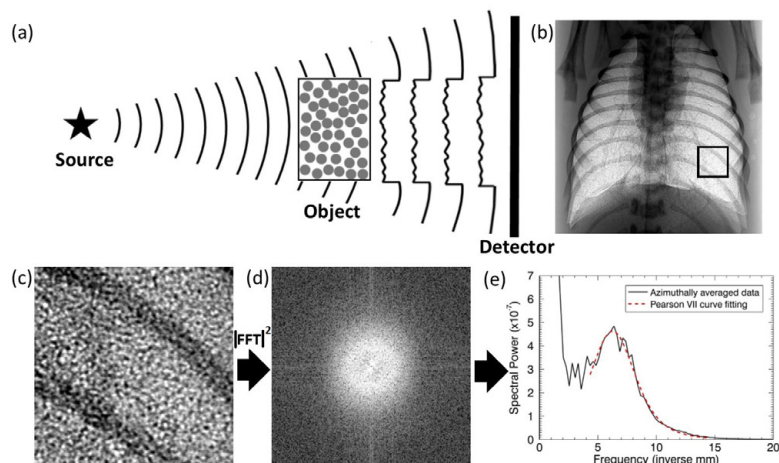


Figure 1. (a) Illumination of a random phase object by partially coherent radiation creates a chaotic speckled intensity pattern upon propagation through space to the detector as a result of interference effects. The many airways in lung tissue can serve as a random phase screen for x-rays, resulting in a speckled pattern such as that shown in (b). This phase contrast image of the lungs of a newborn rabbit kitten was acquired at beamline 20B2 of the SPring-8 synchrotron. Beam energy, 24 keV. Object-to-detector propagation distance, 1 m. Image size, $22.9 \times 23.7 \text{ mm}^2$. A 256×256 pixel region-of-interest indicated by the black square is shown magnified in (c), which reveals the speckle detail. (d) The 2D power spectrum of (c) (log scale). (e) Azimuthal average of (d) showing the raw data fit with a Pearson type VII function for measuring the position of the peak in the power spectrum caused by the speckle. The peak centroid at $6.2 \pm 0.4 \text{ mm}^{-1}$ reveals the dominant length scale of this region of lung speckle is $159 \pm 10 \mu\text{m}$.

magnitude improvement in the accessible scattering vectors over state-of-the-art ultrasmall-angle x-ray scattering (USAXS) instruments, such as the Bonse–Hart camera. Moreover, since the beam can be large enough to illuminate the entire sample, they showed a gain of roughly four orders of magnitude in area and total beam power and another two orders of magnitude because of lower temporal coherence requirements.

We recently reported a technique for using near-field PBI for measuring the size and population of alveoli in small animal lungs in real-time (Leong *et al* 2014). That method utilised the Fourier space signature of speckle patterns created by aerated lung tissue (such as that shown in figure 1(c)) and was able to accurately measure the change in size of alveoli on the micron scale throughout respiration cycles. Each measurement of alveolar size was calculated from statistical analysis of individual images. To acquire the same information from a sufficiently high resolution CT scan would require extremely high x-ray exposure and a very fast scanner to avoid motion blur. The disadvantages of our previous technique are that (i) the total volume of air in the region-of-interest has to be measured and (ii) an image of the non-aerated lungs must be recorded for normalisation purposes. As described below, our new method overcomes these limitations.

In Leong *et al* (2013) we used the transport-of-intensity equation (TIE) (Teague 1983) to find an analytic solution for the azimuthally averaged power spectrum of the near-field intensity of multiple randomly distributed spherical particles, a good approximation for lung tissue, given by:

$$\left| \mathbf{F} \left\{ \frac{I(x, y, z = L)}{I(x, y, z = 0)} - 1 \right\} \right|^2 = N(4\pi R\delta L)^2 \left[\left[\frac{\sin(k_{\perp}R)}{k_{\perp}R} - \cos(k_{\perp}R) \right] \right]^2 \quad (1)$$

Here \mathbf{F} denotes the Fourier transform, I is the intensity, z is the direction of the incident illumination, L is the ODD, δ is the energy dependent refractive index decrement of the scattering medium, N is the number of particles contained within the field-of-view, R is their radius and $k_{\perp} = (k_x^2 + k_y^2)^{1/2}$ is the transverse wavenumber in the (x, y) plane. We see that N , δ and L simply amplify the Fourier space signature as their values increase. The oscillatory term in square brackets is dominated by the cosine term as the sinc function rapidly decays with k_{\perp} , hence the amplitude of the peaks are almost constant for all spatial frequencies. This equation reveals that the size of the scattering objects govern the position and shape of the peaks, independent of sample depth, propagation distance or wavelength (within the near-field). In other words, when the propagation distance is sufficiently small, speckle size equals particle size, which agrees with previous studies (Giglio *et al* 2000, Cerbino 2007). We note that for a distribution of particles, equation (1) shows that more weighting will be given to larger particles and those with greater numbers as the amplitude scales with both R and N . In this model of spherical particles, the volume of the spheres (i.e. the lung volume, V_L) will be $V_L = N4\pi R^3/3$. Hence we see that the amplitude of the power spectrum (PS) in equation (1) is related to V_L (strictly V_L/R). In this paper the power spectrum peak (PS_{Peak}) amplitude is used as a simple measure to reveal approximate changes in lung air volume. Compare this with previous studies where quantitative measures of lung air volume were required, which necessitated immersing the specimen in water (see Kitchen *et al* (2008), Leong *et al* (2013), Leong *et al* (2014)).

In Leong *et al* (2014) we compared two methods of measuring particle/airway dimensions from power spectra. Both used the fact that the lung speckles produce a characteristic peak in the power spectrum (figure 1), as governed by equation (1) and first shown by Hooper *et al* (2007). The first method measured the centroid of the peak (PS_{Peak}) and calculated its reciprocal to determine the corresponding length scale in real space. The second measured the area under this peak (PS_{Area}) and solved for the alveolar size using the lung air volume measured from the images. Both methods required an image of the unaerated lungs to be recorded to normalise the data. To accurately measure absolute lung air volume for method two required the animal to be immersed in water and to initially image the lungs in a non-aerated state (Kitchen *et al* 2008, Leong *et al* 2014). There we imaged the lungs of newborn rabbit kittens and lung phantoms made from packed glass microspheres of known size, having similar dimensions to alveoli, to test these options. It was found that the PS_{Area} gave consistently more reliable results. This was attributed to the fact that dense packing of the particles (or airways) produces short-range-ordering (SRO) that readily alters the PS_{Peak} but only minimally affected the PS_{Area} . The derivation in Leong *et al* (2014) for relating the PS_{Peak} to the particle/alveolar size (equation (1)) assumed purely spatially random packing, which is not possible for a close-packed system.

In this paper we demonstrate that SRO is a major component to the signal produced from packed particles, further validating our previous studies. However, we also show that the aerated lungs of small animals exhibit only minimal SRO, even to quite high levels of aeration when the packing fraction becomes comparatively large. We then show that the discrepancy

between the PS_{Area} and the PS_{Peak} for lungs images shown by Leong *et al* (2014) largely arises because the PS_{Peak} does not indicate the size of the alveoli *per se*, but instead reveals the dominant feature size (length scale) in the image. For a fully aerated adult lung the alveoli occupy around 90% of the total airspace volume. However, when lung volumes are low, particularly in newborns when the lungs are aerating for the first time, the dominant length scale often does not result from the alveoli (that may be fluid filled or collapsed), but to the larger airways in the lungs. Since we used newborn rabbit kittens for our lung model, the PS_{Peak} can be readily influenced by the level of aeration. Herein we show that this new understanding of what the PS_{Peak} represents enables us to use this measurement to accurately quantify changes in the global and regional dominant airway size from a single projection image. Importantly, this approach does not require us to measure the lung air volume or record an image of the lungs in a non-aerated state to measure the airway dimensions.

2. Materials, methods and results

2.1. X-ray sources

Some experiments were conducted at the SPring-8 synchrotron beamline 20B2 in Hutch 3 (Goto *et al* 2001). We also validated the technique using a laboratory based liquid metal jet x-ray source (Excillum, Sweden). For propagation-based imaging (PBI), spatial coherence is more important than temporal coherence (Wilkins *et al* 1996). The monochromatic synchrotron source has the advantage of being highly spatially coherent with the sample positioned ~ 210 m from the $150 \times 10 \mu\text{m}^2$ source. By comparison, the laboratory source is polychromatic, with a characteristic peak at 25 keV. We employed a $\sim 20 \times 20 \mu\text{m}^2$ spot size and a source-to-object distance (SOD) of around 43 cm to produce a beam of moderate spatial coherence that is capable of producing appreciable propagation-based phase contrast (Larsson *et al* 2013). Figure 1 shows the experimental configuration and image processing procedure.

2.2. Near-field speckle analysis

As figure 1 shows, all images were analysed by fitting a highly flexible Pearson VII function (see e.g. Kitchen *et al* (2010b)) to the peak in the azimuthally averaged PS_{Peak} of square arrays cropped from a given data set. Azimuthally averaging greatly amplifies the signal-to-noise ratio of the peak, especially at high spatial frequencies as the number of points averaged over increases with spatial frequency. The characteristic length scale of the speckle was taken as the reciprocal of the peak position. The advantage of curve fitting enables measurement precision much finer than the system's spatial resolution. Images were first corrected for the presence of detector artifacts and beam inhomogeneity using images of the direct beam and dark current, and corrected for blur caused by the point-spread function (PSF) of the imaging system. The PSF was corrected by direct Fourier space division of the images with the measured PSF. This amplifies high frequency noise, but is necessary to accurately determine the PS_{Peak} position.

2.3. Test samples

2.3.1. Synchrotron-based near-field speckle imaging of lung phantoms. To experimentally confirm the validity of a near-field regime, where speckle size is approximately equal to object size and independent of the number of particles and propagation distance, we imaged dry packed soda-lime glass microspheres of known size ranges (63–75 μm and 106–125 μm).

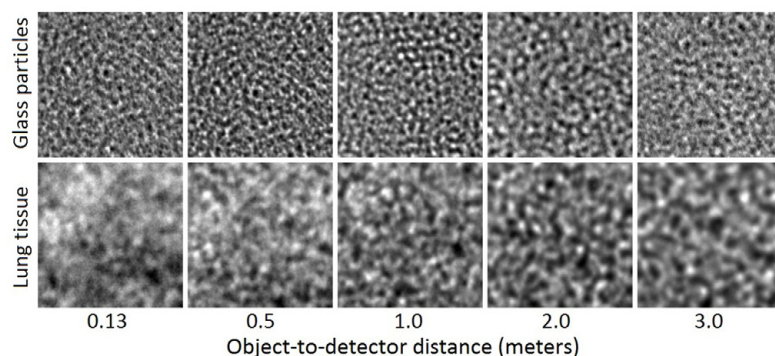


Figure 2. Phase-contrast x-ray images of speckle from glass microspheres with nominal size range 106–125 μm in a 10 mm thick PMMA container and from newborn rabbit lungs. Images are 1.5 \times 1.5 mm².

The microspheres (*Whitehouse Scientific, Ltd.*) were poured into Polymethyl methacrylate (PMMA) containers of set thicknesses of 1, 2, 5, 10 and 20 mm. ODDs were 0.035, 0.13, 0.5, 1.0, 1.5, 2.0 and 3.0 m. Monochromatic 30 keV x-rays were used and images were recorded with a Hamamatsu CCD detector (C4880-41 S) coupled to a powdered 10 μm thick gadolinium oxysulfide ($\text{Gd}_2\text{O}_3\text{:Tb}^{3+}$; P43) phosphor and a tandem lens system yielding an effective pixel size of 5.9 μm . PBI images of such samples are known to produce speckle patterns that are similar to those of the lung of small animals, hence they make for an ideal lung phantom where the dimensions of the refracting bodies are known (Kitchen *et al* 2004). Typical speckle patterns from x-ray images of glass microspheres and rabbit lungs are shown in figure 2.

Figure 3(a) quantifies the speckle size of the microspheres through power spectral analysis for the 106–125 μm particles. A region wherein speckle size remains constant with propagation distance is observed for each sample thickness. The breakdown in this near-field regime was found to occur at shorter ODDs for thicker samples, and for smaller microspheres (63–75 μm ; data not shown).

Within the near-field regime the dominant size of the microspheres measured from the PS_{Peak} position is slightly lower than the manufacturer's nominal size range and is below the mean size expected from the commercial measurement (figure 3(a)). As described by Carnibella *et al* (2012, 2013), this discrepancy results from close packing of the dry packed microspheres. As free particles of similar size become more closely packed they arrange themselves more periodically, like a rhombohedral crystal structure. The characteristic length scale of the speckle pattern is strongly influenced by the distance between planes formed by the particles. In a rhombohedral crystal structure this includes the length scale of $R\sqrt{3}$, which is smaller than the particle diameter ($2R$) (Cumberland and Crawford 1987), leading to the underestimated particle size observed in figure 3(a).

2.3.2. Tomographic evidence for short-range ordering of packed glass microspheres. High resolution CT scans were collected of glass microspheres of various sizes poured into a 10 mm cuvette to observe how the particles packed together. Particle sizes were in the nominal ranges of 63–125 μm , 75–106 μm , 75–125 μm , 150–180 μm , 150–212 μm and 250–300 μm . The 1800 projection images were recorded over 180° of rotation with an exposure time of 200 ms

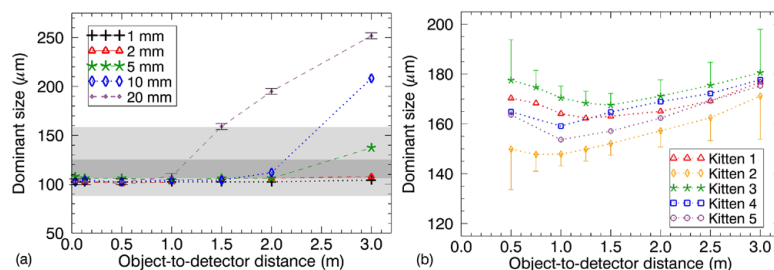


Figure 3. (a) The dominant size of glass microspheres calculated from the peak spatial frequency of the image power spectrum, shown as a function of ODD. Shading indicates the nominal microsphere size specified by the manufacturer (106–125 μm ; dark grey) and the full-width half-maximum of the distribution measured via sieving with a commercial measurement system (*Mastersizer 2000*; light grey). Error bars are consistent for all distances but shown only for one plot for clarity. (b) The dominant size of terminal airspaces in neonatal rabbit lungs calculated from the speckle power spectrum, as a function of ODD. All kittens imaged here were 30 dGA. Only upper and lower error bars have been shown for clarity.

per frame and a propagation distance of 1 m at 30 keV. We employed a scientific-CMOS (sCMOS) (Hamamatsu ORCA Flash4.0; C11440-52U) x-ray camera with a straight fiber optic element coupled to a 10 μm thick gadolinium oxysulfide phosphor with a pixel size of 6.39 μm . We used the single image phase retrieval algorithm of Paganin *et al* (2002) to provide a 3D reconstruction of the attenuation coefficient of the sample with much higher signal-to-noise ratio than is possible with attenuation contrast CT (Beltran *et al* 2011).

Figure 4(a) shows the normalised autocorrelation (AC) of 2D slices of the microspheres taken from the CT datasets. As expected, each curve shows a Gaussian-like function near the origin whose half-width is approximately proportional to the size of the average particles. The curves then oscillate about zero at increasing distance from the origin. The peaks reveal the presence of short-range ordering of the close packed particles at those length scales.

2.3.3. Laboratory-based experiments. Two of the microsphere samples (63–75 μm and 106–125 μm in 10 mm thick cuvettes) were imaged using the laboratory based x-ray source. The SOD was 0.5 m and the ODD was 6.0 m, yielding a geometric magnification factor of 13. We employed a fluoroscopy flat panel detector (*Varian Paxscan 2020 +*) with a native pixel size of 194 μm . With geometric magnification, the effective pixel size was 14.9 μm . Both samples showed clear speckle patterns. The measured size of the 63–75 μm microspheres was $57 \pm 2 \mu\text{m}$ whilst that for the 150–180 μm sized microspheres was $141 \pm 3 \mu\text{m}$. Again we found the particle size was underestimated as a result of SRO.

2.4. Animal studies

Animal experiments were approved by the Animal Ethics Committees at SPring-8, Japan, and Monash University, Australia. All animals were imaged in hutch 3 of beamline 20B2 at the SPring-8 synchrotron. New Zealand white rabbit kittens were delivered by caesarean section at 28 ($n = 11$), 29 ($n = 6$) and 30 ($n = 23$) days gestational age (dGA; term = 31–32 d). Neonates were humanely killed via anaesthetic overdose of sodium pentobarbitone ($>100 \text{ mg kg}^{-1}$),

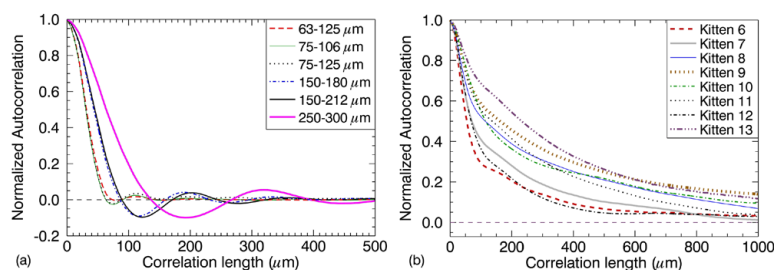


Figure 4. Autocorrelations of CT slices of (a) glass microspheres and (b) rabbit kitten lungs. Peaks at large length scales in (a) result from short-range ordering of particles. This effect is not seen in (b).

then placed on a custom designed small animal ventilator (Kitchen *et al* 2010a) with an endotracheal tube inserted into the mid-cervical trachea. A monochromatic beam energy of 24 keV was selected as it was previously found to provide optimal phase and absorption contrast-to-noise ratio at this facility for small animal lung imaging studies (Kitchen *et al* 2008). At this energy, the surface entry dose to the sample in the hutch was approximately 225 mGy s^{-1} , as measured using an ion chamber.

2.4.1. Near-field lung speckle analysis. To confirm that the near-field regime, wherein speckle size is approximately equal to object size, exists for imaging small animal lungs at diagnostic x-ray energies, images of the thoraces of five newborn rabbit kittens were recorded at various ODD between 0.13 m and 3.0 m, as seen in figure 2. The lungs of the deceased kittens were well aerated prior to imaging and an airway pressure of 20 cm H_2O , delivered by the ventilator, was maintained within the lungs upon closing the endotracheal tube before setting each kitten in a 2% agarose solution to prevent object movement. A sCMOS detector (pco.edge; PCO AG, Kehlheim, Germany) was coupled to a $25 \mu\text{m}$ thick gadolinium oxysulfide ($\text{Gd}_2\text{O}_2\text{S:Tb}^+$) powdered phosphor and a tandem lens system that provided an effective pixel size of $15.1 \mu\text{m}$. With a field-of-view (FOV) of $38.6 \times 32.6 \text{ mm}^2$, the entire thorax was visible in a single exposure.

Figure 3(b) shows the measured dominant airspace size as a function of ODD for five kittens. We see slight differences in airway size between each animal, resulting primarily from differences in tissue compliance and airway pressure. The average size of the airways is similar to previously reported measures of alveolar dimensions for newborn rabbit kittens (Hooper *et al* 2007). Like the glass particle experiment, we observe a steady increase in the calculated airway dimension above a critical distance for each animal between 1.0 m and 1.5 m at this energy and resolution. However, at short ODD lungs also show a decrease in the measured airway as a function of ODD. At ODDs below 0.75 m the speckle contrast-to-noise ratio is very weak and consequently the PS_{Peak} is dominated by other low frequency structures, such as the ribcage, making the measured airway size meaningless. Each sequence goes through a minimum in the measured airway size at distances between 0.75 m and 1.5 m. Here the PS_{Peak} position is more reliably measured, before the size again increases linearly with ODD. Similar to the glass microspheres, the distance at which the measured size begins to increase with ODD tended to become larger with increasing average airway/particle size. A propagation distance of 1.0 m was chosen as the optimal ODD for lung imaging at this

x-ray energy for this species as it is generally large enough to achieve a measureable signal and still remain within the near-field. Section 2.4.2 shows that at this distance speckle size is well correlated with the dominant size of the airspaces. We note that the larger length scale for the lungs, compared to the glass microspheres seen in figure 3, is consistent with the larger size of the speckles apparent in figure 2. Despite the stronger absorption and refraction effects of glass compared to lung tissue, both give measurements close to their expected size within their regions of validity.

2.4.2. Tomographic evidence for the absence of short-range ordering within the lungs. The close packing of airways in the lungs is crucial to the lungs achieving the large surface-area-to-volume ratio required for respiration. SRO similar to that seen with packed glass microspheres (figure 4(a)) therefore seems likely for lung tissue. To test this hypothesis we acquired high resolution CT images of the lungs of newborn rabbits. The 1800 projections recorded over 180° were acquired at a propagation distance of 1.0 m at 24 keV with a 50 ms exposure per frame at beamline 20B2. The same detector was used as for the glass particle CT with a 1 m ODD. With a FOV of $\sim 13.1 \times 13.1$ mm², we could observe most of the lungs of the kittens in a single exposure. The total scan time was ~ 4 min. The surface entry radiation dose was ~ 20.3 Gy. Each kitten was imaged at multiple airway pressures. For the CT reconstruction, a phase retrieval algorithm focusing on the lung tissue was employed using the method described by Beltran *et al* (2011).

Figures 5 and 6 show reconstructed slices of the lungs of two kittens of different gestational ages at two different airway pressures. The size of the airways measured using the PS_{Peak} position from the phase contrast projections is shown in these figures. It can be seen that the measured values closely match the actual airway dimensions. We also see that the airway dimensions vary with airway pressure; a point we shall return to in section 2.4.3. We also see a clear difference in lung behaviour between the near term (30 dGA; figure 5) and preterm (28 dGA; figure 6) kittens. Minor airways (alveoli) of the 30 dGA kitten expand at high pressure, whereas those of the 28 dGA kitten collapse or reflow with lung liquid at low pressure, leaving only the larger airways aerated.

Uncertainties in airway dimensions measured using the PS_{Peak} position were estimated by assessing the variability of sizes measured from the PS_{Peak} of animals imaged at different projection angles at a fixed pressure, and by deliberately altering the initial estimates of the parameters in the curve fitting procedure. This gave a maximum systematic uncertainty of 20 μm when the volume was low and the peaks difficult to fit. With a pixel size of 15.1 μm and a 25 μm thick phosphor, the spatial resolution is around 45 μm . We note that the uncertainty is less than the spatial resolution as a result of the curve fitting interpolation. When the peaks are sufficiently strong and a reasonable estimate is used for the initial curve fitting parameters, the variability is as low as 5 μm , enabling high precision measurements of changes in airway dimensions within an animal, as seen in section 2.4.3.

Figure 4(b) shows the autocorrelations (ACs) of the lungs of several kittens from CT data. Interestingly, the ACs do not show clear peaks of the type seen in figure 4(a) for the packed glass microspheres. Instead the AC function for each kitten asymptotes toward zero at distances much larger than the alveolar diameter. We have also performed these measurements on 3D stacks of the CT slices and the 3D results are of identical form to the 2D results presented here. These results demonstrate a lack of SRO within the lung structure despite there being so many alveoli of similar size packed together. This suggests we can safely ignore any negligible contribution from SRO to the power spectra of phase contrast images of the lungs of small animals.

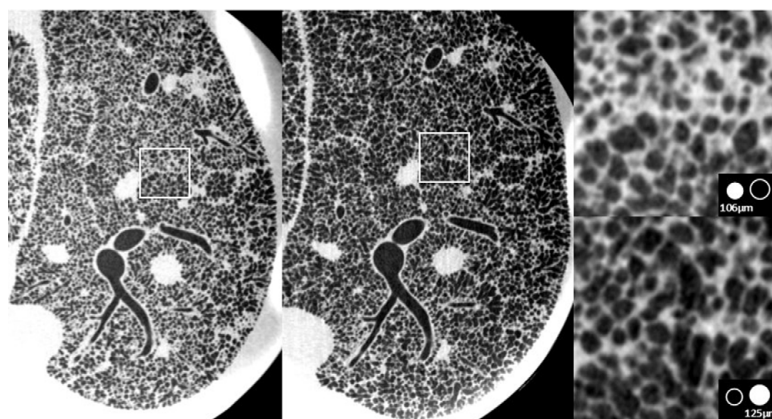


Figure 5. CT reconstruction from a near term 30 dGA rabbit kitten showing the lungs at atmospheric pressure (0 cmH₂O; left) and when inflated to a pressure of 20 cmH₂O (middle). Airways are dark grey and other tissues are lighter grey. Segments highlighted by white boxes are magnified in the right panel (dimensions of 1.9×1.9 mm²). The upper and lower insets correspond to the left and middle panels, respectively. Mean airway dimensions measured from phase contrast projection images were 106 ± 10 μ m at 0 cmH₂O and 125 ± 10 μ m at 20 cmH₂O. Solid white circles indicate these sizes for comparison to alveolar dimensions in the magnified segment. Outlined white circles indicate the airspace size at the other pressure.

Since SRO is not evident in lung tissue (figure 4(b)), the position of any PS_{Peak} of phase contrast images of small animal lungs should faithfully represent the airway size under near-field conditions. However, Leong *et al* (2014) saw clear differences between alveolar dimensions measured from the PS_{Peak} position and the PS_{Area} method combined with the known lung air volume, V_L . As we demonstrate below, this difference is now believed to result from the fact that the PS_{Peak} position does not represent the average alveolar size, but instead simply represents the dominant length scale present in the image, which may or may not be the mean alveolar diameter. Furthermore, Leong *et al* (2014) showed that the PS_{Peak} tended to underestimate the airway dimensions, as revealed by comparisons with granulometry applied to CT data of the lungs. However, we note in that analysis the peak position was not directly measured, rather it was measured after several pre-processing stages that tend to shift the power spectra towards higher spatial frequencies, particularly dividing the image by its absorption contrast image before subtracting the power spectrum of a non-aerated image of the same animal. There the absorption contrast image was approximated by performing phase retrieval on the images under the assumption the object was comprised of a single homogenous material.

Figure 7 shows the dominant airway dimension measured from the PS_{Peak} of single phase contrast projections taken from CT datasets of the chest imaged at three airway pressures for kittens of different gestational ages. We successfully imaged three kittens aged between 29 and 30 dGA and four aged 28 dGA. The data is compared against the dominant range of alveolar dimensions measured by applying 3D granulometry software to the CT datasets assuming spherical alveoli (see Leong *et al* 2014). For all of the data measured at moderate to large volumes we see good agreement between the measurements. This provides further evidence that SRO is not affecting the power spectra, even at large lung air volumes. Conversely, at low volumes we see that the airway

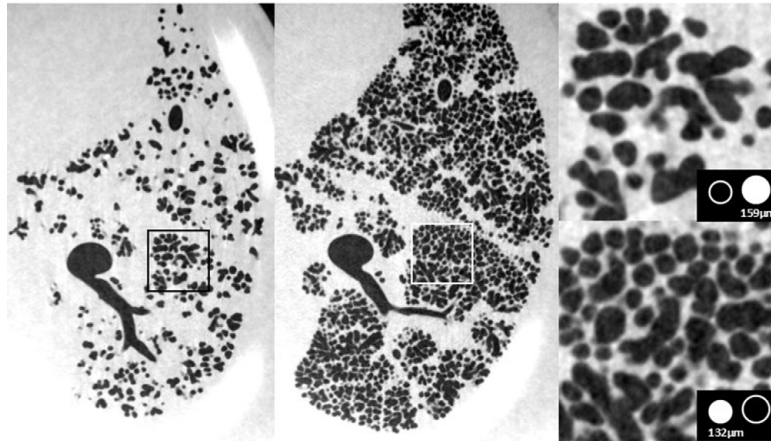


Figure 6. CT reconstruction from a preterm 28 dGA rabbit kitten showing the lungs near atmospheric pressure (1 cmH₂O; left) and when inflated to a pressure of 18 cmH₂O (middle). Segments highlighted by boxes are magnified in the right panel (dimensions of $1.9 \times 1.9 \text{ mm}^2$). Mean airway dimensions measured from phase contrast projection images were $159 \pm 10 \mu\text{m}$ at 1 cmH₂O and $132 \pm 10 \mu\text{m}$ at 18 cmH₂O. Solid white circles indicate these sizes for comparison to alveolar dimensions in the magnified segment. Outlined white circles indicate the airspace size at the other pressure.

dimensions measured from power spectra overestimates the alveolar dimensions measured from granulometry. This results from the fact that many of the alveoli have collapsed at low pressure, hence the dominant length scale in the power spectral is biased toward the size of the major airways. Figure 6 shows a clear example of how the minor airways collapse at low pressure.

2.4.3. *In situ* airway dimension analysis. The data shown in figure 7 is broken into colour-coded segments based upon the gestational age of the kittens. Doing so revealed an unexpected effect. At large air volumes the dominant airway dimensions are all very similar between the kittens of different ages. However, at small volumes the separation between the groups greatly increased. In the youngest animals (28 dGA) the dominant airway dimension are very large, whilst at the oldest age (30 dGA) the opposite is true. CT data (see figures 5 and 6) confirms that in the young animals (28 dGA) the lungs are prone to collapse at low pressure, but with the older animals the majority of the terminal airways remain open but are reduced in size. Upon expiration, the minor airways in the premature animals either collapse (de-recruit) or refill with lung liquid still trapped in the lung's interstitial tissue. Indeed, as these pups are likely to be surfactant deficient (Bland *et al* 1980, Raj and Bland 1986, Siew *et al* 2013), Laplace's law predicts that wall tension within smaller airways will increase as the radius decreases, promoting small airway collapse and redistribution of gas into larger airways (Prange 2002). Thus we have a useful finding whereby the power spectral analysis is capable of readily distinguishing between the developmental maturity of the lungs of newborn animals.

Further evidence for the sensitivity to differences in lung maturity are seen when looking at complete respiratory cycles of newborn (deceased) kittens *in situ*, as shown in figures 8 and 9. Images were recorded at 5 Hz with an exposure time of 40 ms. These rabbits were humanely

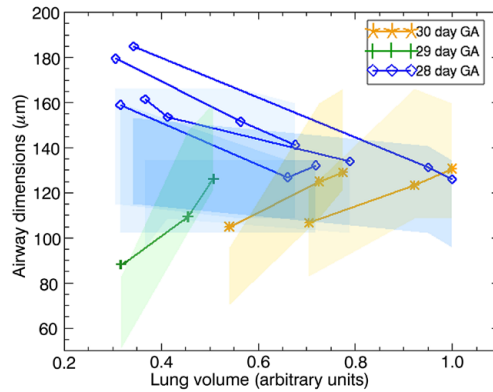


Figure 7. Dominant airway dimensions measured from the peak of the power spectra for various lung air volumes for rabbit kittens of differing gestational age: 28 dGA ($n = 4$; blue), 29 dGA ($n = 1$; green) and 30 dGA ($n = 2$; yellow). All volumes have been normalised to the maximum lung volume measured for all kittens. The more mature 29 and 30 dGA kittens show the expected trend that airway size increases with lung volume. By contrast, 28 dGA kittens show a clear reduction in the dominant airway size with increasing volume. The shaded background shows the dominant airway sizes measured from granulometry from the 3D tomograms of each animal, which shows close agreement with the size measured from the power spectra.

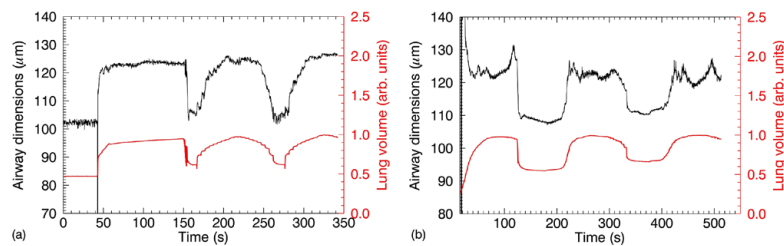


Figure 8. Graphs of the dominant airway size (left y-axis, black curve) from temporal image sequences of lungs ventilated *in situ*. Overlaid is the approximate lung air volume, normalised to the maximum value (right y-axis, red curve). The airway size increases with lung volume in rabbits at (a) 29 dGA and (b) 30 dGA.

killed prior to taking their first breath and the lungs were still filled with fetal lung liquid prior to the onset of imaging and ventilation. These were the same animals used for the tomographic analysis in section 2.4.2 under the same experimental conditions. Air pressure was increased in 2 cmH₂O increments, held for 5 s at each point, and decreased in the same manner after reaching full inflation.

Red curves in figures 8 and 9 show a semi-quantitative measure of lung air volume given by the amplitude of the PS_{Peak} (see section 1). Black curves reveal the dominant airway dimensions measured from the PS_{Peak} position. We see that the airway size typically varies by up to

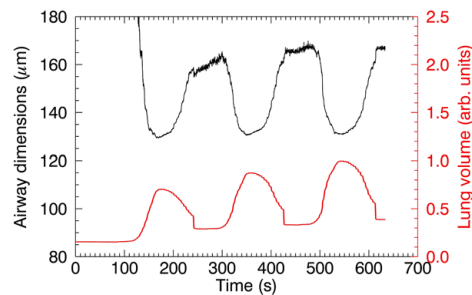


Figure 9. Graph of the dominant airway size (left y-axis, black curve) from a temporal image sequence of lungs ventilated *in situ* in a 28 dGA rabbit. Overlaid is the approximate lung air volume, normalised to the maximum value (right y-axis, red curve). Contrary to the older animals, the dominant airspace size increases as lung volume decreases.

30 μm during the ventilation cycle for the given air pressures employed. Most importantly we see that for the 29 dGA and 30 dGA kittens the airway dimensions follow the trend of the ventilation cycle, but those of the 28 dGA kitten are 180° out-of-phase with the ventilation cycle. All other kittens in these age groups produced the same trends. Considering that the alveolar dimensions should increase with lung volume, this apparent reversal was unexpected. In our previous work (Leong *et al* 2014) we attributed this strange trend to effects associated with SRO. However, we now see that for immature lungs (28 dGA) the inflation slowly recruits increasingly smaller airways leading to a reduction in the dominant length scale measured from the power spectra. These small airways collapse upon expiration and reverse the trend. This result is consistent with the CT data shown above.

Finally, we note that figures 8 and 9 reveal that the measurement of airway dimensions is highly robust against noise, showing a fluctuation of around 3 μm (2–3%) when the volume is constant. This stability results from the robustness of the curve fitting procedure shown in figure 1.

2.4.4. *In vivo* airway dimension analysis. Next we demonstrate that airway dimensions can be measured *in vivo*. Here a 30 dGA kitten was initially ventilated with a sustained inflation to help recruit the lungs (te Pas *et al* 2009), followed by multiple ventilation cycles. Images were acquired at a frame rate of 20 Hz (figure 10) with a 40 ms exposure (surface entry dose ~ 9 mGy per exposure). We see that when the lung initially aerates, the dominant length scale reduces to a minimum as smaller airways are successively recruited before they begin to expand to accommodate an increase in lung air volume. During subsequent standard ventilation cycles the airway size follows the curve of the lung air volume, as expected for kittens in this age group.

2.4.5. Regional morphological lung analysis. All of the data shown thus far have been measured across the whole chest. As figure 1 suggests, regional distributions of airway dimensions can also be measured within a single image. Figure 11 shows the results of locally measuring the PS_{Peak} using 128×128 pixel windows raster scanned across the image shown in figure 1(b). The dominant airway size has a mean of 161 μm and a standard deviation of 9 μm across the chest. These length scales are consistent with that measured using the whole image, which was 159 ± 10 μm . Areas where the regional size measurement contains outliers occur

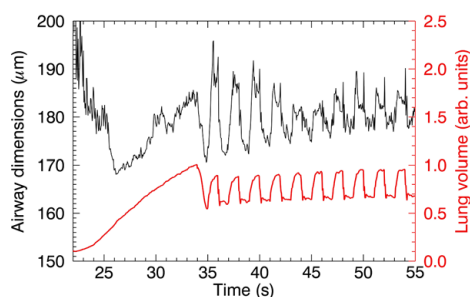


Figure 10. Graph of the dominant airspace size of lungs *in vivo* in a ventilated newborn rabbit at 30 dGA (left y-axis, black curve). Overlaid is the approximate lung air volume, normalised to the maximum value (right y-axis, red curve). An initial 20 s sustained inflation is followed by regular ventilation with a 2.5 s period.

mainly at the borders of the lung and along the frontal portion of the diaphragm where the speckle pattern is interrupted by strong phase contrast from large changes in phase gradient or lack of speckle signal outside the lungs. Elsewhere the size distribution is more homogenous, yet we still see variability in airway dimensions across the lungs.

3. Discussion

We have developed a robust, low dose *in vivo* technique for measuring the dominant lung airway size of small animals both globally and regionally across the lung. Measuring the airway dimensions locally with CT and granulometry here required a dose that was around 2,250 times larger than from the single phase contrast image combined with speckle texture analysis. Although we have not optimised either technique for minimal dose, the spatial and contrast resolution for CT must be sufficiently high to resolve individual alveoli for the granulometry to adequately measure alveolar dimensions. By comparison, speckled 2D phase contrast images readily provide statistical information that reveals changes in lung structure and function during respiration and with far greater precision.

Our technique is capable of measuring dynamic changes in respiratory function with real-time quantitative output. Potential applications include assessment of strategies to reduce ventilation-induced lung injury, respiratory monitoring of preterm infants, and the diagnosis and treatment of lung diseases. A key advantage is that it does not rely on any *a priori* information and requires only a single propagation-based phase contrast x-ray image.

Phase contrast imaging has already proven valuable for imaging respiratory diseases including pulmonary fibrosis (Fouras *et al* 2012), cystic fibrosis (Morgan *et al* 2014), emphysema (Meinel *et al* 2013), lung cancer (Liu *et al* 2008) and for studying lung development at birth (Hooper *et al* 2011). We have commenced trialling the methods presented herein to determine how accurately this method works for other animal models and for detecting respiratory disease. Diseases including BPD and COPD are of particular interest as the airway dimensions and lung structure are altered by these diseases. We aim to determine whether single image analysis of lung speckle patterns in these diseases can provide a low dose alternative method to computed tomography for early disease detection.

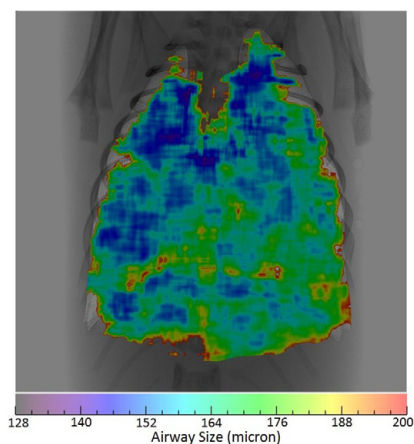


Figure 11. Map of the local dominant airway dimensions measured using power spectral analysis of figure 1(b). The accuracy of the map is low at the boundaries of the lung where the speckle pattern disappears within the ROI; invalid solutions have not been displayed.

Our technique was capable of measuring physiological differences in lung structure and function between preterm rabbits at 28 days gestational age and 29 or 30 days of gestation. This difference was especially clear at near atmospheric pressures where the degree of airspace re-flooding or collapse significantly altered the dominant airspace size. This results from the major physiological transition in lung development preterm infants undergo from the saccular to alveolar stages in late pregnancy (Kotecha 2000, Fraga and Guttentag 2012). This transition is associated with increased activation of epithelial sodium channels that may account for the more efficient lung liquid clearance in rabbits at 29 + d gestation (Olver *et al* 2004). Alternatively, or in addition, this may be caused by increased surfactant production in lung tissue that lowers alveolar surface tension and inhibits collapse, leading to a larger functional residual capacity of the lungs (Hills 1990, Hillman *et al* 2012).

A limitation of the current technique is a decrease in accuracy when there is a high degree of airspace collapse or re-flooding (as was the case for the 28 dGA rabbits). Fewer air-filled spaces within the lungs reduced the speckle contrast, also reducing the amplitude of the power spectrum peak, making curve fitting difficult.

Although it was necessary to correct for non-random packing in the glass microsphere samples, it was found that this was not needed for the rabbit lungs. The large number of length scales in the airway branching (West 1990) reduces the likelihood for ordered stacking of airspaces, introducing a degree of randomness. It is possible that there exists an intermediate stage where there is a small degree of ordered packing, which may require a small corrective factor. We next aim to investigate whether additional structural information can be directly extracted from the speckle texture, such as information about the distribution of airway sizes within the lungs (see Carnibella *et al* (2014)).

In other work we have investigated measuring particle and alveolar dimensions from phase contrast images using autocorrelation analysis of speckle patterns (Carnibella *et al* 2012, 2013, 2014). For packed particles we used an iterative solver to simulate the particle sizes

that was optimised when simulations were a close match to experimental data. That approach has the advantage of not being limited to the near-field condition. It also yields both the mean particle size and their size distribution. In those papers we note that the ACs of the phase contrast images had similar peaks to those seen in figure 4(a). Initially considered as evidence of SRO, we now appreciate that such peaks will exist in the absence of SRO. The AC of the phase contrast image of a single symmetric particle will have a peak that simply reveals that the Fresnel fringes are identical on either side of the particle. Hence the peak position approximately indicates the particle size. This is in contrast to the absorption contrast AC of a particle, whose size is related to the width of the zeroth order peak of the AC function. We note that the power spectrum is related to the AC via a Fourier transform according to the Wiener–Khinchin theorem, hence the information could potentially be extracted via either approach, but in our experience the power spectrum method has proven to be a simple, robust and accurate method that is faster to compute. AC techniques are well known for being highly robust to noise (Carnibella *et al* 2012), but curve fitting the power spectral peak also provides a noise robust solution.

Leong *et al* (2014) showed that airway dimensions can be measured from the PS_{Area} provided the absolute lung air volume is known since the PS_{Area} depends upon two unknown variables, namely the size and number of particles/alveoli (see equation(1)). Since our new technique provides an independent measure of their size it is theoretically possible to measure the lung air volume by combining the PS_{Area} and PS_{Peak} . However, since the lungs are surrounded by many overlapping structures including bones, skin and fur that affect the power spectrum, an image of the chest with the lungs absent (e.g. collapsed or fluid filled) is required to quantitatively measure the lung air volume. For newborns this image may be obtainable because the fetal lung may be liquid filled, but in many cases will not be as it is difficult to image the lungs before the onset of breathing. We are currently investigating methods to accurately recover volume without requiring *a priori* knowledge.

It is well known that propagation-based phase contrast can be achieved using a polychromatic micro-focus laboratory based x-ray source (Wilkins *et al* 1996). Furthermore, it has recently been shown that lung speckle patterns of the type shown here using synchrotron radiation have been observed in the laboratory (Garson *et al* 2013). With powerful new x-ray sources capable of producing highly spatially coherent beams, such as the liquid metal jet employed here (see also Larsson *et al* (2013)) and new low noise sCMOS or photon counting detectors being developed, we expect that our technique will be suitable for clinical implementation.

This study demonstrates the quantitative retrieval of the dominant airway size from a single phase contrast projection image of rabbit lungs *in vivo*. This non-invasive technique is robust, low dose and sensitive to micron changes at sub-pixel resolution, making it ideally suited for dynamic imaging of respiratory function. It also provides regional information that shows the distribution of airway dimensions across the lungs, which may prove useful for the detection of early lung disease using much less radiation than CT and with greater sensitivity than absorption contrast imaging.

Acknowledgments

The synchrotron radiation experiments were performed at BL20B2 of SPring-8 with the approval of the Japan Synchrotron Radiation Research Institute (JASRI) (Proposal No. 2013B0047 and 2014A0047). We wish to thank Dr Kentaro Uesugi and Prof. Naoto Yagi for their assistance with experiments at SPring-8. This research was partially supported by the

Victorian Government's Operational Infrastructure Support Program. We acknowledge travel funding provided by the International Synchrotron Access Program managed by the Australian Synchrotron and funded by the Australian Government. AFTL acknowledges the support of an Australian Postgraduate Award. MJK, SBH and MJW acknowledge funding from the Australian Research Council (ARC; Grants DP110101941 and DP130104913) and the National Health & Medical Research Council (NHMRC; APP1064973). MJK is an ARC Australian Research Fellow. AF is an NHMRC Career Development Fellow. SBH is an NHMRC Senior Principal Research Fellow.

References

- Beltran M A, Paganin D M, Siu K K W, Fouras A, Hooper S B, Reser D H and Kitchen M J 2011 Interface-specific x-ray phase retrieval tomography of complex biological organs *Phys. Med. Biol.* **56** 7353–69
- Bland R D, McMillan D D, Bressack M A and Dong L 1980 Clearance of liquid from lungs of newborn rabbits *J. Appl. Physiol.* **49** 171–7
- Carnibella R P, Kitchen M J and Fouras A 2012 Determining particle size distributions from a single projection image *Opt. Express* **20** 15962–8
- Carnibella R P, Kitchen M J and Fouras A 2013 Decoding the structure of granular and porous materials from speckled phase contrast x-ray images *Opt. Express* **21** 19153–62
- Carnibella R P, Kitchen M J and Fouras A 2014 Single-shot x-ray measurement of alveolar size distributions *Medical Imaging 2014: Biomedical Application in Molecular, Structural and Functional Imaging* ed R C Molthen and J B Weaver (San Diego, California, USA: SPIE Proceedings) vol 9038 90380V
- Cerbino R 2007 Correlations of light in the deep Fresnel region: an extended Van Cittert and Zernike theorem *Phys. Rev. A* **75** 053815
- Cerbino R, Peverini L, Potenza M A C, Robert A, Bösecke P and Giglio M 2008 X-ray-scattering information obtained from near-field speckle *Nat. Phys.* **4** 238–43
- Cumberland D J and Crawford R J 1987 *The Packing of Particles* vol 6 (Amsterdam: Elsevier)
- Fouras A, Allison B J, Kitchen M J, Dubsky S, Nguyen J, Hourigan K, Siu K K W, Lewis R A, Wallace M J and Hooper S B 2012 Altered lung motion is a sensitive indicator of regional lung disease *Ann. Biomed. Eng.* **40** 1160–9
- Fraga M V and Guttentag S H 2012 *Lung Development: Embryology, Growth, Maturation and Developmental Biology Avery's Diseases of the Newborn* ed C A Gleason and S U Devaskar (Philadelphia: Elsevier Saunders) pp 571–83
- Garson A B III, Isaguirre E W, Price S G and Anastasio M A 2013 Characterization of speckle in lung images acquired with a benchtop in-line x-ray phase-contrast system *Phys. Med. Biol.* **58** 4237–53
- Giglio M, Carpineti M and Vailati A 2000 Space intensity correlations in the near field of the scattered light: a direct measurement of the density correlation function $g(r)$ *Phys. Rev. Lett.* **85** 1416–9
- Goodman J W 2000 *Statistical Optics* (New York: Wiley)
- Goto S *et al* 2001 Construction and commissioning of a 215 m-long beamline at SPring-8 *Nucl. Instrum. Methods A* **467** 682–5
- Hillman N, Kallapur S G and Jobe A 2012 Physiology of transition from intrauterine to extrauterine life *Clin Perinatol.* **39** 769–83
- Hills B A 1990 The role of lung surfactant *Br. J. Anaesth.* **65** 13–29
- Hooper S B *et al* 2007 Imaging lung aeration and lung liquid clearance at birth *FASEB J.* **21** 3329–37
- Hooper S B, Kitchen M J, Fouras A, Wallace M J, Dubsky S, Siu K K W, Siew M L, Yagi N, Uesugi K and Lewis R A 2011 Combined lung imaging and respiratory physiology research at SPring-8 *Synchrotron Radiat. News* **24** 19–23
- Irvn C G and Bates J H T 2003 Measuring the lung function in the mouse: the challenge of size *Respir. Res.* **4** 4–12
- Jobe A H, Hillman N, Polglase G, Kramer B W, Kallapur S and Pillow J 2008 Injury and inflammation from resuscitation of the preterm infant *Neonatology* **94** 190–6
- Kitchen M J *et al* 2008 Dynamic measures of regional lung air volume using phase contrast x-ray imaging *Phys. Med. Biol.* **53** 6065–77

- Kitchen M J, Habib A, Fouras A, Dubsy S, Lewis R A, Wallace M J and Hooper S B 2010a A new design for high stability pressure-controlled ventilation for small animal lung imaging *J. Instrum.* **5** T02002
- Kitchen M J, Paganin D M, Uesugi K, Allison B J, Lewis R A, Hooper S B and Pavlov K M 2010b X-ray phase, absorption and scatter retrieval using two or more phase contrast images *Opt. Express* **18** 19994–20012
- Kitchen M J, Paganin D, Lewis R A, Yagi N, Uesugi K and Mudie S T 2004 On the origin of speckle in x-ray phase contrast images of lung tissue *Phys. Med. Biol.* **49** 4335–48
- Kotecha S 2000 Lung growth for beginners *Paediatr. Respir. Rev.* **1** 308–13
- Larsson D H, Lundström U, Westermark U K, Henriksson M A, Burvall A and Hertz H M 2013 First application of liquid-metal-jet sources for small-animal imaging: high-resolution CT and phase-contrast tumor demarcation *Med. Phys.* **40** 021909
- Leong A F T, Buckley G A, Paganin D M, Hooper S B, Wallace M J and Kitchen M J 2014 Real-time measurement of alveolar size and population using phase contrast x-ray imaging *Biomed. Opt. Express* **5** 4024–38
- Leong A F T, Paganin D M, Hooper S B, Siew M L and Kitchen M J 2013 Measurement of absolute regional lung air volumes from near-field x-ray speckles *Opt. Express* **21** 27905–23
- Liu P, Sun J, Guan Y, Yue W, Xu L X, Li Y, Zhang G, Hwu Y, Je J H and Margaritondo G 2008 Morphological study of early-stage lung cancer using synchrotron radiation *J. Synchrotron Radiat.* **15** 36–42
- Meinel F G *et al* 2013 Diagnosing and mapping pulmonary emphysema on x-ray projection images: incremental value of grating-based x-ray dark-field imaging *Plos One* **8** e59526
- Milne S and King G G 2014 Advanced imaging in COPD: insights into pulmonary pathophysiology *J. Thorac. Dis.* **6** 1570–85
- Morgan K S *et al* 2014 *In vivo* x-ray imaging reveals improved airway surface hydration after a therapy designed for cystic fibrosis *Am. J. Respir. Crit. Care* **190** 469–72
- Olver R E, Walters D V and Wilson S M 2004 Developmental regulation of lung liquid transport *Annu. Rev. Physiol.* **66** 77–101
- Paganin D, Mayo S C, Gureyev T E, Miller P R and Wilkins S W 2002 Simultaneous phase and amplitude extraction from a single defocused image of a homogeneous object *J. Microsc.* **206** 33–40
- Pauwels R A and Rabe K F 2004 Burden and clinical features of chronic obstructive pulmonary disease (COPD) *Lancet* **364** 613–20
- Prange H D 2002 Laplace's law and the alveolus: a misconception of anatomy and a misapplication of physics *Adv. Physiol. Educ.* **27** 34–40
- Raj J U and Bland R D 1986 Lung luminal liquid clearance in newborn lambs. Effect of pulmonary microvascular pressure elevation *Am. Rev. Respir. Dis.* **134** 305–10
- Sera T, Yokota H, Tanaka G, Uesugi K, Yagi N and Schroter R C 2013 Murine pulmonary acinar mechanics during quasi-static inflation using synchrotron refraction-enhanced computed tomography *J. Appl. Physiol.* **115** 219–28
- Siew M L *et al* 2013 The role of lung inflation and sodium transport in airway liquid clearance during lung aeration in newborn rabbits *Pediatr. Res.* **73** 443–9
- Suzuki Y, Yagi N and Uesugi K 2002 X-ray refraction-enhanced imaging and a simple method for phase retrieval for a simple object *J. Synchrotron Rad.* **9** 160–5
- Teague M R 1983 Deterministic phase retrieval: a Green's function solution *J. Opt. Soc. Am.* **73** 1434–41
- te Pas A B *et al* 2009 Establishing functional residual capacity at birth: the effect of sustained inflation and positive end-expiratory pressure in a preterm rabbit model *Pediatr. Res.* **65** 537–41
- West B J 1990 Fractal forms in physiology *Int. J. Mod. Phys. B* **4** 1629–69
- Wilkins S W, Gureyev T E, Gao D, Pogany A and Stevenson A W 1996 Phase-contrast imaging using polychromatic hard x-rays *Nature* **384** 335–8
- Yagi N, Suzuki Y, Umetani K, Kohmura Y and Yamasaki K 1999 Refraction-enhanced x-ray imaging of mouse lung using synchrotron radiation source *Med. Phys.* **26** 2190–3